



HAL
open science

A mesoscale investigation of the endothelial glycocalyx and its interaction with blood flow

Sofia Biagi

► **To cite this version:**

Sofia Biagi. A mesoscale investigation of the endothelial glycocalyx and its interaction with blood flow. Human health and pathology. Université Grenoble Alpes; Università degli studi La Sapienza (Rome), 2016. English. NNT: 2016GREAY083 . tel-01693743

HAL Id: tel-01693743

<https://theses.hal.science/tel-01693743v1>

Submitted on 26 Jan 2018

HAL is a multi-disciplinary open access archive for the deposit and dissemination of scientific research documents, whether they are published or not. The documents may come from teaching and research institutions in France or abroad, or from public or private research centers.

L'archive ouverte pluridisciplinaire **HAL**, est destinée au dépôt et à la diffusion de documents scientifiques de niveau recherche, publiés ou non, émanant des établissements d'enseignement et de recherche français ou étrangers, des laboratoires publics ou privés.

THESIS

for the degree of

DOCTOR OF PHILOSOPHY

under joint supervision between the
Communauté Université Grenoble Alpes
and the
Sapienza Università di Roma

Subject : **Physics**

By **Sofia BIAGI**

Thesis director : **Chaouqi MISBAH**

Thesis co-director : **Francesco SCIORTINO**

A mesoscale investigation of the endothelial glycocalyx and its interaction with blood flow

(Étude mésoscopique du glycocalyx endothélial
et de son interaction avec le sang)

Discussed on: December 2nd, 2016

Jury:

M. Abdul BARAKAT

Research Director, École Polytechnique Paris-Saclay (referee)

M. Stefano GUIDO

Professor, Università degli Studi di Napoli Federico II (referee)

M. Benoît POLACK

Professor, Centre Hospitalier Universitaire Grenoble Alpes (president)

M. Marco MACCARINI

Researcher, Laboratoire TIMC-IMAG (member)



COMMENT GARGANTUA NASQUIT EN FAÇON BIEN ESTRANGE
COME FU CHE GARGANTUA VENNE AL MONDO IN MODO MOLTO STRANO

*Par cest inconvenient
feurent au-dessus relaschéz les cotyledons de la matrice,
par lesquelz sursaulta l'enfant, et entra en la vène creuse,
et gravant par le diaphragme jusques au dessus des espales
(où la dicte vène se part en deux) print son chemin à gauche,
et sortit par l'aureille senestre.*

(Per tale inconveniente,
i cotilèdoni della matrice si allentarono in alto
e il bambino ne profitò per infilarsi d'un balzo nella vena cava;
di qui arrampicandosi per il diaframma fin sopra le spalle,
dove la detta vena si biforca, prese il cammino a manca
e se ne uscì per l'orecchia sinistra).

trad. di A. Frassinetti

Gargantua et Pantagruel, F. Rabelais

Contents

Introduction	1
Introduction (french version)	3
1 Background and project design	5
1.1 A historical overview	5
1.2 Endothelial glycocalyx: a bioorganic polymer brush . . .	8
1.2.1 The architecture of the EGL	9
1.2.2 The EGL in the macro- and micro-circulation . . .	10
1.3 The major fraction of blood volume: Red Blood Cells . .	14
1.3.1 RBC mechanical properties	14
1.3.2 RBC rheology	16
1.4 Previous models for the EGL and recent results	19
1.4.1 Theoretical approaches to the EGL	20
1.4.2 Recent experiments	22
1.5 Genesis of our project	23
Résumé (french version)	26
2 Coarse-graining with Dissipative Particle Dynamics	29
2.1 The choice of the numerical method	29
2.1.1 Coarse-graining techniques for liquids	30
2.2 The code	31
2.2.1 DPD methodology	31
2.2.2 Details on the algorithm	34
2.2.3 The system geometry and the boundary conditions	35
2.3 DPD and physical units	38
2.4 The coarse-graining of the RBC membrane	40
2.4.1 The stress-free triangulation	41
2.4.2 Membrane energy	44
2.4.3 Boundary conditions and cylindrical geometry . .	45
2.4.4 Coarse-graining level and physical units	47

Résumé (french version)	52
3 Equilibrium properties of the brush	55
3.1 A basic model for a polymer brush	55
3.2 Density profiles and scalings	58
3.2.1 The longest relaxation time	61
3.2.2 Chain stiffness	64
3.3 Polydisperse brush	65
3.3.1 Bimodal distribution	66
Résumé (french version)	70
4 Polymer brushes under flow	73
4.1 Single polymer dynamics	74
4.2 Solvent velocity field: the flow inversion	79
4.3 Collective polymer dynamics: brush surface waves	82
4.4 Polidispersity	86
4.5 Possible origins of the surface wave	87
4.5.1 An overview on surface waves	89
4.5.2 Polymer brush as an elastic solid: importance of the shear modulus	91
Résumé (french version)	96
5 Red Blood Cells through brush coated microchannels	99
5.1 RBC in bare channel	100
5.2 Polymer brush as a rigid compartment for a RBC	105
Résumé (french version)	111
6 Final discussion	113
6.1 Technical issues: one more success for DPD	113
6.2 Finite size effects on the surface wave phenomenon	114
6.3 Speculations	116
Résumé (french version)	120
Conclusion and perspectives	123
Conclusion et perspectives (french version)	127
A The conservative force parameter	131
B Expressions for the RBC membrane forces	133
C Membrane boundary conditions	137

Introduction

The present thesis aims to contribute to the understanding of the flow-induced dynamics of polymer brushes.

A polymer brush is a dense matrix of grafted macromolecules. Playing on its chemical composition or on the geometry of its architecture, it is possible to differentiate and finely tune the physico-chemical features of the grafting surface. Thanks to such high versatility, the design of polymer brushes has received much attention in the field of polymer science [1–8]. At the same time, the discovery that the inner surface of various mammalian organs is coated with tethered polymers has sparked the interest of biologists [9–12]. A prominent example is provided by the blood circulatory system: an heterogeneous filamentous network, mainly composed of grafted glucose macromolecules and proteins, decorates the inner surface of vessel walls; its name is *endothelial glycocalyx* [12–14]. A complete understanding of the endothelial glycocalyx behavior still represents a challenge for modern science, because the partially unknown dynamics of polymer brushes couples with the intrinsic complexity of the surrounding medium, namely the flowing blood.

Polymer brushes at equilibrium have been appropriately characterized: theoretical models (mean-field or scaling theories [15, 16]), experiments (especially neutron scattering [17, 18]) and numerical simulations (by mean of Monte Carlo and Molecular Dynamics methods [19, 20]) agree in predicting the monomer distribution and provide the estimation for the layer thickness and its correct scalings as function of the grafting density and polymerization degree. On the contrary, an organic description of the polymer brush dynamics in steady states, that is, when a shear flow drives the grafted polymers away from their equilibrium configurations, is still lacking and no consensus has been reached [21–24]. Envisioning how a polymeric coating, as the mentioned glycocalyx, can interfere with the flowing plasma and with the suspended blood particles is, therefore, far from being a simple task. The fundamental problem to be addressed

might be summarized as follows:

what is the *hydrodynamic response* of a polymer brush?

which generates a cascade of questions: what are the brush's characteristic timescales that are dynamically relevant? If we consider the top layer of a dense polymer brush as a two dimensional interface, would it be prone to develop instabilities? Finally, since a general concept concerning out-of-equilibrium dynamics states that boundary conditions can propagate and influence the system bulk, how does the dynamics of the brush interface affect the solvent bulk properties? Given the long-range nature of hydrodynamic interactions and the out-of-equilibrium dynamics, it cannot be excluded a priori that polymers dynamics could even influence the motion of a flowing object. These questions have no clear-cut answers and additional data are required in order to grasp the many facets of polymer brush systems.

The present thesis, by mean of numerical simulations, proposes a self-consistent coarse-grained model for a dense polymer brush under parabolic flow. Our mesoscale investigation highlights the relevance of polymer brush collective effects as driven by long-ranged hydrodynamics. For the first time in the same numerical framework a deformable object is also included, as prototype of a red blood cell, and preliminary results are provided for its interaction with a polymeric coating. Thus, such a case study adds a mesoscopic point of view to the state of the art deepening the investigation on glycocalyx behavior under parabolic flow and of its interaction with blood.

Introduction (french version)

Ce travail contribue à la compréhension de la dynamique des brosses de polymères.

Une brosse de polymères est une matrice dense de macromolécules greffées. En jouant sur sa composition chimique ou sur la géométrie de son architecture, il est possible de différencier et d'affiner les caractéristiques physico-chimiques de la surface de greffage. Grâce à une telle polyvalence, la conception de brosses de polymères a reçu beaucoup d'attention dans le domaine de la science des polymères [1–8]. En même temps, la découverte que la surface interne de divers organes de mammifères est revêtue de polymères greffés a suscité l'intérêt des biologistes [9–12]. Un exemple remarquable est fourni par le système circulatoire du sang: une structure hétérogène de filaments, composée principalement de macromolécules et de protéines de glucose greffées, décore la surface interne des parois des vaisseaux; son nom est *glycocalyx endothélial* [12–14]. Une compréhension complète du comportement du glycocalyx endothélial représente encore un défi pour la science moderne, parce que la dynamique partiellement inconnue des brosses de polymères se couple avec la complexité intrinsèque du milieu environnant, c'est-à-dire le sang qui coule.

À l'équilibre les brosses de polymères ont été caractérisées de façon bien appropriée: modèles théoriques (théories de champ moyen ou d'échelle [15, 16]), expériences (notamment le scattering de neutrons [17, 18]) et simulations numériques (via méthodes Monte Carlo et Molecular Dynamics [19, 20]) concordent tous pour prédire la distribution de monomères et estimer l'épaisseur de la couche avec ses lois d'échelle en fonction de la densité de greffage ou du degré de polymérisation. Au contraire, une description organique de la physique des brosses de polymères à l'état stationnaire, c'est-à-dire lorsqu'un écoulement de cisaillement entraîne les polymères greffés loin de leurs configurations d'équilibre, fait encore défaut et le consensus n'a pas été trouvé [21–24]. Envisager comment un revêtement de polymères, tel que le glycocalyx susmentionné, peut interférer avec le plasma s'écoulant et avec les particules de sang en suspension est loin d'être une tâche simple. Le problème fondamental à résoudre pourrait se résumer de la façon suivante:

quelle est la *réponse hydrodynamique* d'une brosse de polymères?

Voilà qui génère une cascade de questions: quelles sont les échelles de temps caractéristiques de la brosse qui sont dynamiquement pertinentes? Si l'on considère la couche limite d'une brosse dense comme une interface

bidimensionnelle, pourrait-elle développer des instabilités? Enfin, comme un concept général concernant la dynamique hors équilibre indique que les conditions aux limites peuvent se propager et influencer tout le volume du système, comment la dynamique de l'interface de la brosse affecte les propriétés du solvant? Compte tenu du long rayon des interactions hydrodynamiques et de la dynamique hors équilibre, il ne peut pas être exclu a priori que la dynamique des polymères pourrait même influencer la mécanique d'un objet en écoulement. Ces questions n'ont pas de réponses claires et des analyses supplémentaires sont nécessaires pour saisir les nombreuses facettes des systèmes de brosses de polymères.

Cette thèse, en utilisant des simulations numériques, propose un modèle coarse-grained et auto-cohérent pour une brosse dense de polymères sous écoulement parabolique. Notre étude mésoscopique met en évidence l'importance des effets collectifs entre molécules, entraînés par l'hydrodynamique. Pour la première fois dans le même cadre numérique, un objet déformable est également inclus, comme prototype d'un globule rouge, et des résultats préliminaires sont fournis pour son interaction avec une couche de polymères. Ainsi, une telle étude ajoute un point de vue mésoscopique à l'état de l'art en approfondissant le comportement du glycocalyx sous écoulement parabolique et avec le sang.

Chapter 1

Background and project design

The reference system, an heterogeneous filamentous matrix mainly composed of glucose macromolecules covering the inner walls of all blood vessels and called “endothelial glycocalyx”, is introduced. Its composition and basic functions are presented, together with the properties of red blood cells, which constitute the main fraction of blood volume. The strategy by which the present thesis addresses the problem of glycocalyx and of red blood cell modeling is presented and critically discussed.

1.1 A historical overview

In 1940, thanks to Danielli and his experiments on the permeability of frog capillaries, the hypothesis of a thin layer coating the inner surface of vessel walls appeared for the first time in the scientific literature [25]. Danielli noted that the same kind of macromolecule was able to pass through the pores of the capillary membrane in the absence of serum¹ while it could not perfuse towards tissues if serum was present. He ascribed such behavior to the presence of a film of blood proteins adsorbed on the capillary wall, which obstructed the capillary pores. Since that moment, the idea of a protein layer adhering to the *endothelium*² served as a guideline for follow-up works pertaining to blood circulation physi-

¹Serum is blood plasma not including clotting factors.

²The endothelium is the innermost cell layer of a blood vessel.

ology [26–28]. However, only in 1966 a measurement performed by Luft raised such intuition from the ground of mere hypothesis to the level of observable data [12]. Luft adopted the newborn improved-resolution technique of electron microscopy and revealed a 20 nm-thick layer covering mouse diaphragm capillary walls. His paper reports the very first image of an endothelial glycocalyx layer (Fig.1.1(a)). Such convincing evidence immediately provided the key for new appealing interpretations regarding blood circulation data and the subsequent thirty years marked great advancements in the field. For example, in Refs. [29,30], the thickness of the luminal³ surface layer was related to changes in blood cell deformation: it was observed that red blood cells (RBCs) assume a less elongated shape after a chemical treatment targeted against the components of the luminal surface layer. Moreover, in 1994, comparisons with blood flow in glass capillaries highlighted an increase in blood flow resistance⁴ in real vessels, attributed, again, to the presence of the endothelial film [31]. In this study, flow resistance is measured in different capillaries (ranging in between 10 μm and 30 μm in diameter) at different hematocrit⁵ values: as evident from Fig.1.1(b), experimental data display a higher resistance than expected according to the *in vitro* model, which assumes bare vessel walls. Therefore Pries et al. proposed to take into account a tube radius reduction due to the presence of the endocapillary layer. Such new *in vivo* model provides a better fit (see Fig.1.1(b)). Then, in 1996, a surprising progress was achieved by Vink and Duling, whose new experimental protocol led to the first *in vivo* estimation of the layer volume [32]. Instead of dehydrating the sample, as for the *ex vivo* measurements, and using fixatives, which might damage the network and dissolve some proteins, they used a dye-exclusion technique to finally measure the actual thickness of the layer. They unexpectedly found a much more pronounced thickness than measured before: around 0.5 μm thick. If such a non-negligible layer (around 10% of the smallest capillary diameter) covers the luminal surface of blood vessels, it surely has to play a relevant role in the homeostasis of the circulatory system and in the exchanges between blood and tissues. It was finally proved that the interface between blood and organs was not a simple one-dimensional separation line nor a trivial plasma layer but

³Referred to the *lumen*, namely the inner space of a tubular organ, as a blood vessel, for example.

⁴Flow resistance R is defined as the ratio of the pressure drop over the volume flowrate $R = \Delta P/Q$.

⁵The hematocrit is defined as the ratio of red blood cell volume over the whole blood volume.

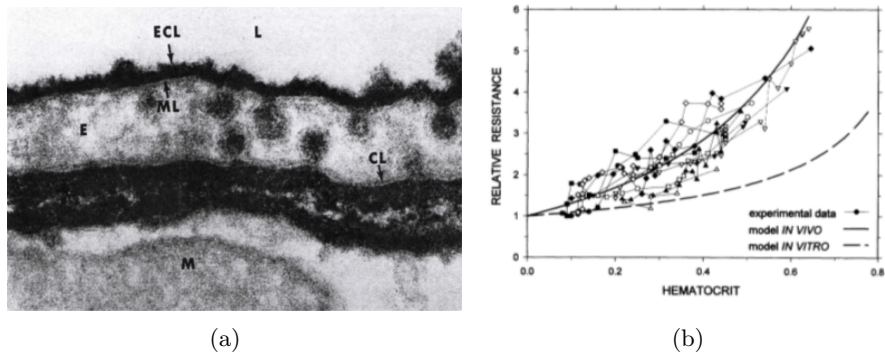


Figure 1.1: Two milestone results in the history of the endothelial glycocalyx investigation: panel (a) reports the first image of an endothelial glycocalyx layer, as it appeared in ref. [12] [ECL=endocapillary layer, L=lumen]; panel (b) shows the enhanced blood resistance in real microvessels with respect to the *in vitro* one, as measured by Pries et al. (Ref. [31]). In (b) experimental values, relative to different capillary radii in between 10 μm and 30 μm and normalized by the correspondent plasma value, are suitably fitted by the *in vivo* model, taking into consideration the presence of an endocapillary layer reducing the tube diameter.

rather a more composite and active structure than considered till that moment. For the scientific community it was clear that the discovered coating deserved deeper attention and a new, proper name: from the unspecified definition of “endocapillary layer” such structure was baptized as “endothelial glycocalyx layer” (EGL). The word “glycocalyx”, coined by Bennett to indicate the generic extracellular polysaccharide coating on cells [33], means “husk made up of glucose” or, as translated elsewhere with a taste of affection [34], “sweet shield”. For our purposes it is worth mentioning, in this historical overview, an additional paper, by Rostgaard and Qvortrup [35], dated back to 1997: the endothelial glycocalyx was established to be not a uniform coverage but rather an heterogeneous bush-like network made up of filaments, as documented by Fig.1.2(a) and by a more recent image at higher resolution in Fig.1.2(b). It was thus recognized as a dense polymer brush.

Twenty years have already elapsed, now, and research on that structure has intensified and it has not ended yet. The high resolution modern techniques have allowed for a characterization of the whole structure, thus information regarding its chemical composition and electrostatic properties are known [14, 37]. The belief that an alteration in the glycocalyx

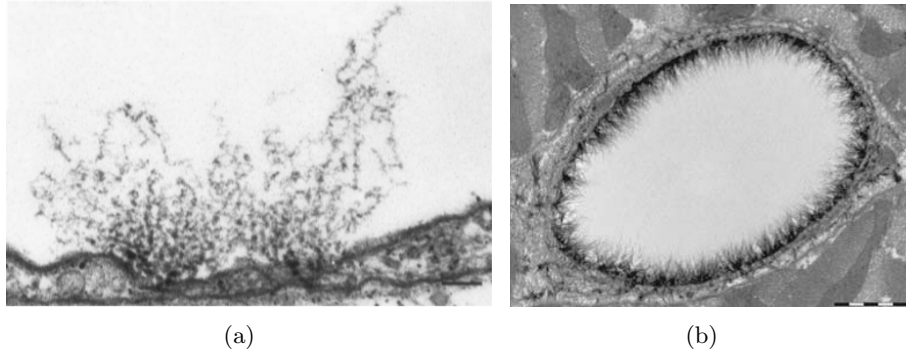


Figure 1.2: Electron microscopy images of endothelial glycocalyx. Bars correspond to $0.5\mu m$ and $1\mu m$ respectively. (a) In 1997 glycocalyx is recognized to be a bush-like polymer brush composed of wavy filaments [35]; (b) a more recent image (cross-section of a rat left ventricular myocardial capillary) obtained by using alcian blue staining, offers a higher resolution view of this hairy network [36].

could be associated to physiological dysfunctions and diseases is now a certainty [13, 38, 39]. However, physiologists as well as physicians explicitly ask for further studies before introducing a glycocalyx treatment in the medical practice [13, 40]. In particular, since the EGL is exposed to circulating blood, it is necessary to better clarify its flow-induced dynamics. In this thesis we propose to model the EGL as a dense polymer brush under parabolic flow.

Before presenting our working hypotheses and chosen set-up, we examine in the following Section the composition and basic functions of the EGL.

1.2 Endothelial glycocalyx: a bioorganic polymer brush

In his paper regarding the first observation of the endothelial glycocalyx, Luft defined the EGL as “flocculent material” [12]. Modern techniques have now allowed for a more precise characterization on the scale of nanometers [14, 41]. We report below the main features of the EGL structure.

1.2.1 The architecture of the EGL

Endothelial glycocalyx is a negatively-charged network of membrane-bound macromolecules [14]. Its name refers to the substrate (*endothelium*) on which filaments composing it are grafted. However, not all the macromolecules are attached directly to the substrate: indeed, they are collected in bush-like bundles (see Fig.1.2 and Fig.1.3(a) for an idealized sketch). It is a delicate medium and difficulties in the visualization are due to its degradation under treatments and preparation protocols. Now it has been established that its thickness ranges from 0.1 μm to 1 μm [37,42]. It is a comparable value with respect to the thickness of the vessel wall itself (endothelium is less than 0.1 μm -thick in capillaries [43]), while it is no more than 10% of the tube diameter even in the smallest capillaries. Such proportions reveal how it forms a significant compartment devoted to vessel wall shielding, without constituting a relevant obstacle to blood flow.

Its main components are: proteoglycans, glycosaminoglycans and glycoproteins, together with absorbed plasma proteins.

- *Proteoglycans*

Proteoglycans are the core proteins and are stiff macromolecules directly attached to the substrate. They constitute a sort of “backbone”, which other components are linked to.

- *Glycosaminoglycans*

Glycosaminoglycans (GAGs) are repeated disaccharide units with negative charge. They can have a high degree of polymerization giving to EGL a large potential extension. Heparan sulfate, chondroitin sulfate and hyaluronan are some of the most abundant GAGs in the EGL. All GAGs, except hyaluronan, are attached to a core protein. While GAGs have several sulfation sites and therefore can bind different kinds of plasma proteins conferring heterogeneity to the EGL, hyaluronan is nearly inert and has basically a space-filling and hydration role. However, since it is directly synthesized by the endothelial cell membrane, it is reasonable to assume that sudden environmental changes produce modifications in its metabolisms that can be directly responsible of glycocalyx dysfunctions. [44].

- *Glycoproteins*

Several families of glycoproteins are expressed by the EGL. Most of them act as mediators for cell adhesion signaling. For example,

selectins and immunoglobulins are involved in the leukocyte-cell interaction, while integrins play a role in the platelet-cell interaction. In healthy conditions these glycoproteins are hidden inside the EGL thickness. The shedding of glycocalyx, which causes the uncovering of the glycoprotein receptors, is the first response toward inflammation or coagulation processes.

- *Plasma proteins*

Several kinds of plasma-derived proteins can dock to GAGs. Embedded within the EGL or layered on top of it, they control the functionality of the local environment [45].

Glycocalyx incorporates molecules in a dynamic equilibrium, since it continuously binds and replaces both endothelium-derived and in-blood flowing substances [40]. Thus it is a self-assembling composite three-dimensional matrix.

From a morphological point of view the EGL has a precise geometry, as represented in Figs.1.3: anchor points of the bush-like bundles draw a 6-fold pattern on the endothelium. The average spacing between neighboring anchors is 100 nm, but the bush-like structure of filaments produce a thickening, with spacing around 20 nm in all directions. The monomer diameter, too, is around 20 nm, thus making of the EGL a very dense matrix.

1.2.2 The EGL in the macro- and micro-circulation

The endothelial glycocalyx decorates the lumen of every vessels of mammals, birds and amphibians [46]. The basic functions of the EGL play a substantial role in small vessels as well as in big ones. However, since the exchange with tissues is a prerogative of microcirculation, it is reasonable to assume microcapillaries to be the preferential stage on which EGL reveals the richest range of its behaviors.

We list below the most relevant functions of the EGL.

- EGL acts as mechanotransductor

It has been proved that endothelial cells are sensitive to the shear stress induced by blood flow [47–49]. Their morphology and chemical response are determined by the strength and direction of these hemodynamic forces. For example, their shape and nucleus orientation align with the flow direction [48, 49] and the production

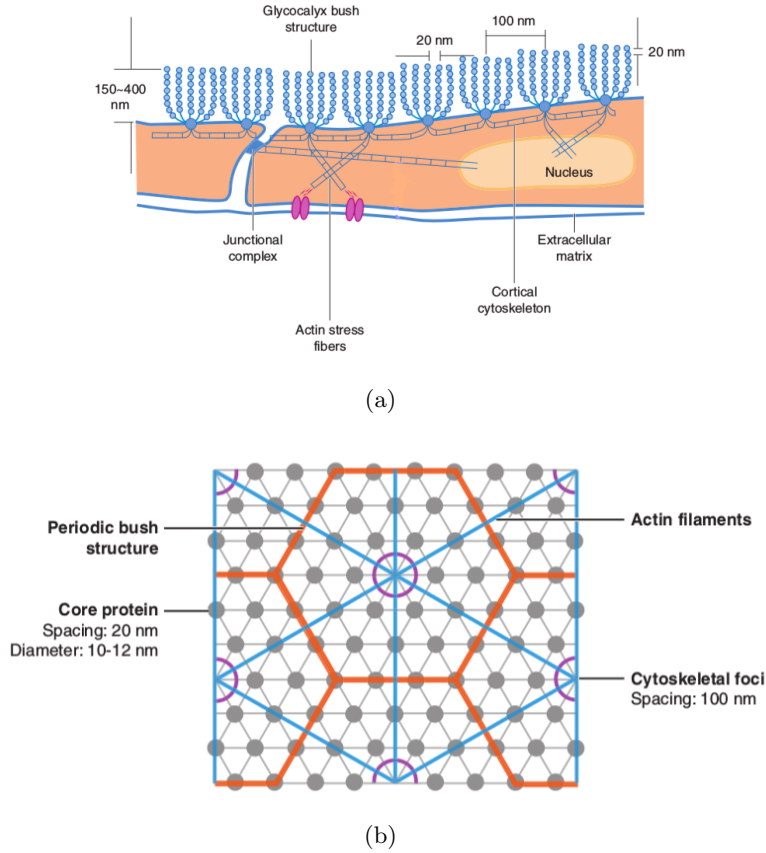


Figure 1.3: Schematic view of the endothelial glycocalyx morphology (images from [14]): (a) configuration of fibers and spacing among them; (b) idealized top view of the 6-fold distribution of anchors.

rate of nitric oxide [47, 50], as well as the synthesis of specific proteins [45, 51], is subordinate to the shear stress profile. The way mechanical stresses are translated into chemical signals is still partly unknown, but surely the EGL participates to such process: thanks to its stiffer fibers, it transmits the shear to the endothelial cells, acting as a mechanotransducer. Interestingly, it is not the intensity itself but rather the kind of shear stress that is responsible of the specific endothelial cell reaction [52, 53]. Indeed, a low shear stress or a strong time-dependent one are the most dangerous for the health: they fail to align cells and promote inflammatory processes. Those kinds of shear stresses can occur in case of fluid vortices and turbulence, likely to develop in big vessels where the

Reynolds number is really high (≈ 4000) [54, 55]. For example, at big artery bifurcations, vortices and recirculation zones can be created where the plasma is stagnant so that, eventually, those sites become prone to arteriosclerosis.

- EGL regulates adsorption

The EGL avoids adsorption of blood-flowing particles onto the vessel walls [14]. Deposition of massive particles, especially fatty tissues and low-density lipoproteins (LDL), results in irreversible bumps that penetrate the first layer of the vessel wall. It is the starting stage of an inflammatory process leading to sclerotic plaque formation (atherogenetic state) and stiffening or even death of the surrounding tissue [56]. Also platelets and White Blood Cells (WBCs) would attach to the endothelium if the adhesion receptors on the endothelial surface were not screened by a proper EGL thickness [57]. Such kinds of flow obstruction increase the risk of thrombosis and atherosclerosis, together with their pathological complications, namely heart attacks and strokes.

- EGL regulates permeability of capillary walls

In addition to protection, mechanotransduction and adhesion regulation, at the level of microcirculation the EGL has another key role. Indeed, the walls of big arteries and veins are constituted by several layers of different tissues, as schematized in Fig.1.4, while the capillary wall is basically a single layer of endothelial cells. Therefore, while the wall stratification at the level of macrocirculation keeps blood well separated from the surrounding tissues, at the microcirculatory level the exchange between blood and organs is allowed. Thus, the EGL acts as an interface effectively tuning permeability of capillary walls. In fact, capillary walls are included among the most permeable interfaces and it has been remarked that living cell membranes hardly possess such a low level of selectivity unless “permeability action is subordinate to that of the intercellular structure and substances” [28]. Therefore, it is clear that the selection between filtration and absorption, as well as the amount of proteins passing from blood to tissue and vice versa, should involve the EGL. Nowadays, the so-called *revised* Starling principle, illustrating the balance of oncotic and hydrostatic pressures between blood and tissues, takes into account the EGL presence [58, 59]. Hence, a damaged glycocalyx is linked to dysfunctions of the blood

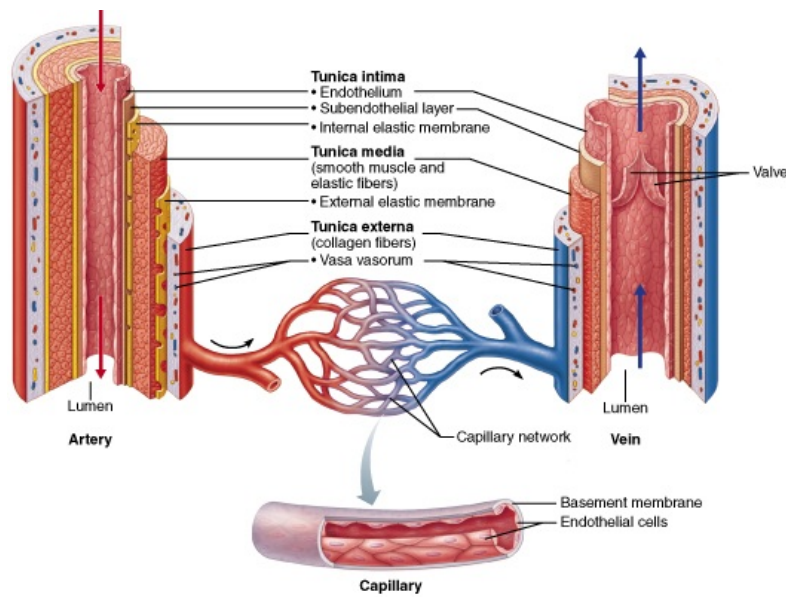


Figure 1.4: Sketch of the stratified walls of blood vessels. For big arteries and veins, several layers are enclosed one in the other: (from the innermost on) the endothelium, the tunica intima, the tunica media and the tunica externa. Capillary walls, on the other hand, are composed of just a single layer of endothelial cells embedded by a membrane. (Image from [61]).

homeostasis and it is associated with diseases like edemas [25, 36] or albuminuria [39, 60].

- EGL influences hematocrit and blood viscosity
 In microcapillaries blood viscosity and hematocrit are actually modulated by the EGL [31, 45]. Indeed, both the size of a WBC and of a RBC are comparable with the smallest capillary diameter, thus, the presence of a glycocalyx layer affects the way in which they arrange inside it. A WBC, occupying all the available room, has to crush the glycocalyx fibers down. Differently, a RBC is highly deformable and it easily flows under strong confinement. However, for a given speed, its degree of deformation, and hence its overall shape, depends on the EGL thickness: the larger the EGL width is, the more elongated shape is assumed by the RBC in order to avoid contact with the EGL fibers.

1.3 The major fraction of blood volume: Red Blood Cells

A Red Blood Cell (RBC), also called erythrocyte, is the main character of the circulatory system. With its hemoglobin content it is responsible of the transport of oxygen and carbon dioxide throughout the vascular system. The quantity of RBCs determines the hematocrit, that in healthy conditions is around 45% of the blood volume fraction. From a biological point of view, having no nucleus, a RBC can be considered among the simplest cells, however it displays a rich variety of behaviors under rheological investigations. To give a feeling of such complexity, we first outline its mechanical properties.

1.3.1 RBC mechanical properties

As sketched in Fig.1.5, the RBC membrane is made of a phospholipid bilayer: phospholipid pairs assemble in a closed surface with their hydrophilic heads toward the surrounding fluid and the hydrophobic tails screened inside the so-formed membrane. The width of such a membrane

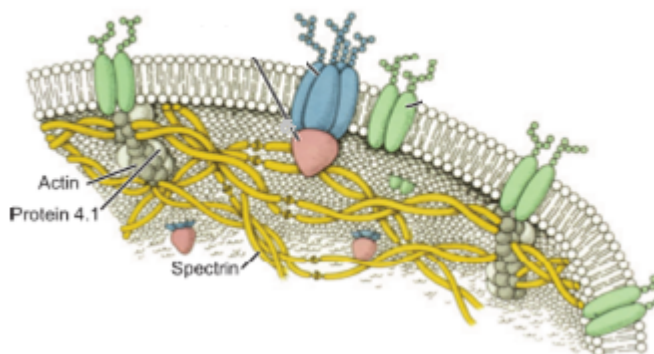


Figure 1.5: A picture of a section of the RBC membrane: the phospholipid bilayer is sustained by a network of spectrin protein filaments, called cytoskeleton. Junction points made of actin proteins connect the cytoskeleton to the phospholipidic portion of the membrane.

is of the order of few nanometers, while the cell has a typical diameter of $7.8 \mu\text{m}$ and a thickness of almost $3 \mu\text{m}$. The gap between these length-scales justifies the idealization of the membrane as a two dimensional surface, as assumed in basically all the RBC models aiming at reproduc-

ing blood rheology. The van der Waals interaction between phospholipids confers to the membrane an area expansion/compression modulus K of the order of 400 mN/m. Since it is much higher than the shear stresses associated to the RBC passage through vessels, the membrane is considered to be both locally and globally inextensible [62]. The crossing of such phospholipidic bilayer is allowed only to small molecules (i. e. water molecules). Thus, under isotonic physiological conditions, a balance is established between the molecules flowing inwards and outwards and no net change in the cell volume is registered. At physiological temperature, the bilayer is in a liquid state and shearing at constant area does not cost too much energy, since phospholipidic molecules are free to move and rearrange, however, the RBC membrane does display shear resistance. Such mechanical properties is conferred to the cell by its *cytoskeleton*. The cytoskeleton is a network of spectrin filaments that sustains the phospholipidic bilayer. Spectrin proteins are connected in a quasi-hexagonal lattice with typical distance of about 70 nm between the junctional complexes made of actin. With a shear modulus μ between 1 and 13 $\mu\text{N/m}$ the cytoskeleton resists to stretch and shear deformations [62]. Differently, the phospholipidic bilayer has no shear resistance, as already mentioned, but it resists bending. The cell bending modulus k_c has been measured to be in the range $k_c = 0.13 - 3 \times 10^{-19}\text{J}$. It helps the cell restoring the previous shape after each deformation [62]. Indeed, the most important feature of a RBC is its ability to deform. At rest, the RBC has a typical discoidal biconcave shape, but, during its lap through the circulatory system, the RBC flows in big arteries of some centimeters of diameter as well as in microcapillaries of diameter down to 4 μm . Recalling that the RBC size is around 8 μm , the latter corresponds to a highly strong confinement. As a result, the cell changes shape and arranges to fit the new condition. Then it recovers the discoidal shape as soon as the pressure drop pushes it towards venules and big vessels.

The reason for such mechanical property, given the non extensibility of the membrane, resides in the combined effects of the flexibility given by its membrane and of its membrane *excess area*. The possibility to range over several different shapes is actually due to the membrane excess area, as compared to a sphere of equal volume, or, in the other way round, to the *reduced volume* as compared to a sphere of equal surface. In literature it

is often defined the reduced volume ν , as a useful dimensionless quantity:

$$\nu = \frac{V_0^{tot}}{\frac{4}{3}\pi \left(\frac{A_0^{tot}}{4\pi}\right)^{3/2}} \quad (1.1)$$

and such that $\nu < 1$. With the values of mean surface area $A_0^{tot} = 135\mu\text{m}^2$ and of mean volume $V_0^{tot} = 94\mu\text{m}^3$, a healthy RBC yields a constant reduced volume $\nu = 0.64$. Confirmations of the key role of RBC deformability for blood flow come also from the consideration that the life-span of healthy RBCs ranges over 4 months, approximately, and during this period the deformability of each RBC is tested at any cycle by the spleen, that with its cascade of increasingly thin capillaries filters away the cells that are no more able to deform. Indeed, a reduction in RBC deformability reflects in enhanced blood flow resistance and inefficient oxygen exchange. It is involved in hemopathologies, like sickle cell anemia, spherocytosis and elliptocytosis [63].

It should be noted that the response of a RBC is not purely elastic, since the viscosity of the inner fluid ($\eta_{in} \approx 6\text{mPas}$) and of the whole membrane ($\eta_m \approx 0.5\mu\text{Ns/m}$) adds a dissipative character to the dynamics⁶.

A summary of the quantities characterizing the RBC is shown in Tab.1.1 together with their measured values. The RBC elastic moduli are usually estimated by means of micropipette aspiration or optical tweezers [65–67].

1.3.2 RBC rheology

Blood, being a suspension of microscopic particles in a mainly watery medium, is a complex fluid, as revealed by measurements of its apparent viscosity [68]. Peculiar blood trends are represented by the Fahraeus-Lindqvist effect and by the shear-thinning [69, 70]. Indeed, the blood apparent viscosity decreases on increasing blood confinement (for tube diameters smaller than $300\mu\text{m}$) and displays a minimum as the tube diameter becomes comparable to the RBC diameter⁷ (Fig.1.6(a)). This is due to the presence of a *cell-free* layer along the wall. Such layer (also

⁶With “whole membrane” we refer both to the phospholipidic bilayer, that is actually without shear resistance, and to the underlying cytoskeleton, that gives the major viscous contribution [64].

⁷We recall that this is strictly true in glassy tubes, while *in vivo* the apparent viscosity minimum is measured in vessels whose diameter is around $30\mu\text{m}$, because of the presence of the EGL [31].

RBC property	Value
the mean cell diameter D_0	$D_0 = 7.82\mu\text{m}$
the mean total surface area A_0^{tot}	$A_0^{tot} = 135\mu\text{m}^2$
the mean total cell volume V_0^{tot}	$V_0^{tot} = 94\mu\text{m}^3$
the shear modulus μ_0	$\mu_0 = 1 - 10\mu\text{N/m}$
the area compressibility modulus K	$K = 300 - 500\text{mN/m}$
the bending constant k_c	$k_c = 0.13 - 3 \times 10^{-19}\text{J}$
the membrane viscosity η_m	$\eta_m = 0.47 - 1\mu\text{N s/m}$
the internal viscosity η_{in}	$\eta_{in} = 5 - 7\text{mPa s}$

Table 1.1: Physical values for the quantities characterizing the mechanics of a RBC.

called *plasma-rich zone*) has a thickness of few micrometers and results from the balance between a lift force, that tends to align RBCs towards the channel centerline, and diffusion, that makes them spread. In smaller pores the viscosity increases slightly. Moreover, it decreases as function of the applied shear rate, indicating the RBC ability in conforming the shape to the flow streamlines (Fig.1.6(b)).

The dynamics of a flowing RBC is extremely various and sensitive to parameters like the viscosity contrast λ and the capillary numbers Ca_{bend} and Ca_{shear} . The former is defined as the ratio between the inner and the outer fluid viscosities

$$\lambda = \frac{\eta_{in}}{\eta_{out}} \quad (1.2)$$

and it discriminates between a fluid-like dynamical regime ($\lambda \ll 1$) and a rigid-body-like motion of the cell ($\lambda \gg 1$); the bending capillary number Ca_{bend} is defined as the ratio between the cell bending relaxation timescale and the flow timescale:

$$Ca_{bend} = \frac{\tau_{bend}}{\tau_{flow}} = \frac{\eta_{out}\dot{\gamma}D_0^3}{k_c}, \quad (1.3)$$

while the shear capillary number Ca_{shear} is defined as the ratio between the cell shear elasticity relaxation timescale and the flow timescale:

$$Ca_{shear} = \frac{\tau_{shear}}{\tau_{flow}} = \frac{\eta_{out}\dot{\gamma}D_0}{\mu_0}. \quad (1.4)$$

In two dimensional models the specification of λ and Ca_{bend} is sufficient to define the RBC dynamical regime: the cell membrane is indeed a closed

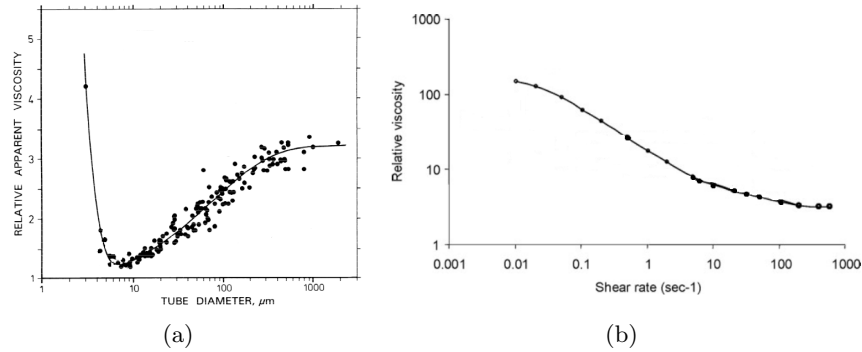


Figure 1.6: Panel (a) documents the Faraheus-Lindqvist effect: the blood apparent viscosity decreases on decreasing the tube diameter and reaches a minimum value in channels whose size is comparable to the RBC major axis size. Further decreasing the pore size leads to an increase of viscosity: thanks to RBC deformability, the flow experiences a higher resistance but it is not completely hindered. Image from Ref. [71]. Panel (b) displays the blood shear-thinning behavior: the ability of RBCs to change shape leads to a decrease of the blood viscosity as a function the shear rate. Image from Ref. [70].

curve with no extensibility. Shear elasticity cannot be envisioned and the cell dynamics equalizes that of a vesicle, namely of a phospholipidic membrane without cytoskeleton. At high enough Ca_{bend} , it exists a threshold value λ_c for the viscosity contrast below which the cell does not change shape nor orientation while the membrane rotates around the cell center of mass, like the tread of a tank, and shears the internal fluid: it is the so-called *tank-treading* motion [72]. On increasing the viscosity contrast above λ_c , the cell rather behaves like a rigid-body and the dynamics switches to a *tumbling* regime, in which the cell flips continuously [73]. The equivalence with vesicle dynamics works only in two dimensions. Examination, both by experiments and simulations, of different kind of flow and especially the consideration of the third space dimension demonstrate the existence of new other dynamical regimes which are peculiar to RBCs (for example: swinging [74, 75], kayaking [76, 77], and breathing dynamics with large deformations [78]), whose investigation is still ongoing. In addition, RBCs have been shown to interact with each other, giving raise to collective effects that, in some cases, are not negligible (see RBC diffusion [79] and aggregation both in large vessels [80] as well as in small ones [81]).

In the smallest capillaries the RBC ability to change shape in response

to a deforming force reaches the higher rate. In Fig.1.7 some of the commonly observed shapes for a RBC under strong confinement are reported: by similarity, they are called *parachute*, *croissant*, *bullet* and non-centered *slipper*. Indeed, it is worth noting that in microcapillaries of 10 μm of diameter the cell center of mass can move out of the pore centerline and the cell can assume asymmetric shapes.

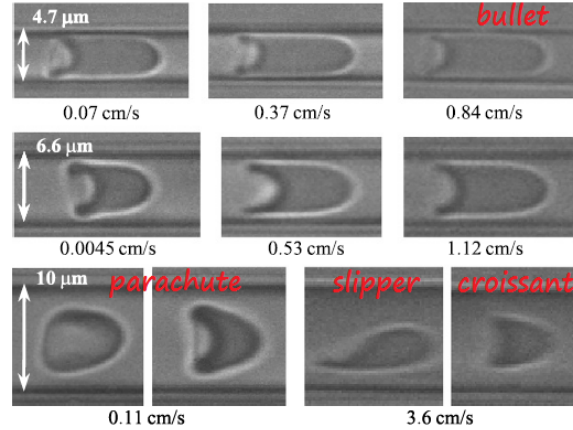


Figure 1.7: Typical deformed shapes, obtained by using a high-speed resolution camera, for a RBC flowing in microcapillaries: parachute, croissant, bullet and the non-centered slipper shapes are indicated. Figure from [62].

1.4 Previous models for the EGL and recent results

It is common knowledge in biophysics that a good model for blood is made up of a simple Newtonian liquid and one single kind of deformable particles [68]. In the previous sections we have presented an additional element, the endothelial glycocalyx, and we have discussed why it is essential to include it in order to properly describe blood microcirculation. An important amount of work has been devoted throughout the years in addressing such problem. Below, we review some models that have been suggested to account for the presence of the EGL, followed by the outline of recent results that lead to new, open questions.

1.4.1 Theoretical approaches to the EGL

The first model was proposed by Pries *et al.* [31]. As we have already mentioned, Pries *et al.* found an enhanced blood resistance in real vessels, which did not obey the *in vitro* model, namely the Faraheus-Lindqvist expression for the apparent viscosity:

$$\eta_{vitro} = 220e^{-1.3D} + 3.2 - 2.44e^{-0.06D^{0.645}} \quad (1.5)$$

where D is the tube diameter. Such expression is valid at the physiological hematocrit $H_D = 0.45$, otherwise a factor must be included to take into account the different RBC volume fraction. The new, *in vivo* model of Pries *et al.* is basically an heuristic correction that fits data much better:

$$\eta_{vivo} = \left[1 + (\eta_{vitro} - 1) \left(\frac{D}{D - W} \right)^{4\lambda} \right] \left(\frac{D}{D - W} \right)^{4(1-\lambda)} \quad (1.6)$$

where W is a fitting parameter with the dimension of a length. The constant value λ , $0 \leq \lambda \leq 1$, tunes the role of the presence of the EGL: for $\lambda = 0$ the difference with respect to the *in vitro* model is completely ascribed to a reduction of the effective diameter, while for $\lambda = 1$ the correction takes into account other possible factors (irregularity of the vessel geometry, presence of WBCs,...). They found the best agreement with data for $\lambda = 0.5$ and $W = 1.1\mu\text{m}$.

The flow inside the EGL has been investigated by treating the layer as a binary mixture (a solid phase and a fluid phase). In particular, Damiano *et al.* solved the problem of axisymmetric pressure-driven flow in a cylindrical channel with a binary mixture layer at the wall [82]. In the limit of an infinitesimally small solid volume fraction, the viscosity of the fluid in the wall layer equals the viscosity of the fluid in the lumen and the mixture is rather a uniform porous medium with a certain hydraulic resistivity K . Thus, the velocity field inside the layer obeys a Brinkman equation:

$$\begin{aligned} \eta \nabla^2 \vec{v} - K \vec{v} &= \nabla p \\ \nabla \cdot \vec{v} &= 0 \end{aligned} \quad (1.7)$$

where η is the viscosity of the incompressible fluid, \vec{v} the velocity field and p the pressure. It is useful to define the dimensionless quantity δ as the ratio of viscous drag forces over hydraulic resistance forces, $\delta^2 = \eta/(h^2K)$ where h is the layer thickness. If $\delta \ll 1$, hydraulic resistance

forces dominate and the Darcy’s law is recovered. For the EGL they calculated $\delta \approx 10^{-3} - 10^{-4}$, thus the flow throughout the EGL basically vanishes and the shear stress on the endothelium surface is eliminated. Such model points out the importance of the EGL fibers in transmitting the shear stress to the endothelial cells (mechanotransduction) and has inspired follow-up analyses on the mechanical properties of these grafted macromolecules (see the “elastohydrodynamic model” below).

The so-called “elastohydrodynamic model” considers the EGL macromolecules to have a preferential, vertical orientation and assigns to the fiber a finite bending rigidity EI [83, 84]. Thanks to such bending rigidity, they can resist the bending moment due to the shear stress at the outer EGL edge and transmit the mechanical stimuli to the grafting substrate, namely to the endothelial cells. An indirect estimation of EI is extracted by calculating the characteristic fiber recovery time (measured to be $< 1\text{s}$ [85]) after the passage of a WBC. Precisely, in Ref. [83], the authors use the small deflection theory and focus only on the final stage of the fiber elastic recoil, while in Ref. [84] large deformations are envisioned. In the latter study, the flow inside the EGL is assumed to follow a Brinkman-type equation and the estimation for the bending rigidity is $EI = 450\text{pN nm}^2$. Recent numerical simulations, aiming at reproducing the flow in the vicinity of the EGL, follow such outcome and supply the grafted polymers with a bending stiffness [86].

The elastic properties of the EGL fibers have attracted attention because of the non-trivial phenomenology associated to the mechanism of their recovery after the WBC passage: the layer is crushed to almost the 80% of its uncompressed thickness and can restore its undisturbed shape within half a second. Thus, the EGL fibers seem to be easily compressible and yet able to rapidly recover their previous configuration. On the other hand, other mechanisms than elasticity can play a role in the interaction between the EGL and the RBCs. For example, the exclusion of the RBC from the EGL could originate from a response to an electrostatic potential gradient, to a chemical potential gradients or to a combination of the two [87, 88]. The electrostatic potential, as elucidated in the so-called “mechano-electrochemical model” [88], results from the interaction between the highly charged EGL macromolecules and the free ions in solution, while the chemical potential is generated by a difference in the concentration of GAGs inside the EGL with respect to concentration in plasma (rather than a difference between the concentration of plasma proteins adsorbed to the EGL and the free plasma proteins flowing in the

capillary lumen, as previously suggested in the “oncotic model” [87]).

1.4.2 Recent experiments

Each one of the mentioned models grasps some key characteristic of the EGL. Nevertheless, the flow profile in the vicinity of the EGL, and of a polymer brush more generically, still raises some questions.

Experiments have highlighted the peculiarity of the *in vivo* velocity profile at the interface with glycocalyx [89,90]. Smith et al. [89], specifically, measured the velocity of microspheres in the so called plasma-rich zone, assuming a uniform shear flow. Damiano et al. [90] observed tracers along the whole microcapillary diameter and found that the shear flow in the plasma-rich zone is not uniform: the velocity has an exponential rather than a uniform radial distribution and the shear rate at the EGL interface is ≈ 4 times higher than expected according to the Poiseuille law with the same centerline velocity (see Fig.1.8(a)). It should be noted that in both works half of the sampled tracers was not taken into account, as only microspheres with monotonically increasing speed were considered. Moreover, those measurements do lack resolution in the vicinity of and inside the EGL.

Even choosing simpler experimental conditions, as for in *in vitro* experiments on artificial polymer brushes, the phenomenology is not easier to interpret. A recent publication by Lanotte et al. [42] revealed the new, following puzzle. The flow velocity through a hairy capillary (where the brush thickness is around 10% of the microchannel diameter) still has a parabolic shape and is slower than in a bare one of the same radius (shown in Fig.1.8(b)). However, to fit it with a Poiseuille formula it is necessary to reduce the channel radius of almost *twice* the brush thickness. This means an enhanced viscosity near the wall due to the polymer coating. The authors identify a possible explanation for the reduced velocity in the backflow effect, a phenomenon that has been reported in literature [86,91,92] which consists in the reversal of the flow direction in a thin layer near the brush surface. Another suggested hypothesis concerns polydispersity (i.e. the presence of macromolecules with different polymerization degree): longer chains are not detected by the apparatus which measures the brush thickness, but they can retard the flow.

In conclusion, the flow profile at the brush surface deserves further investigations.

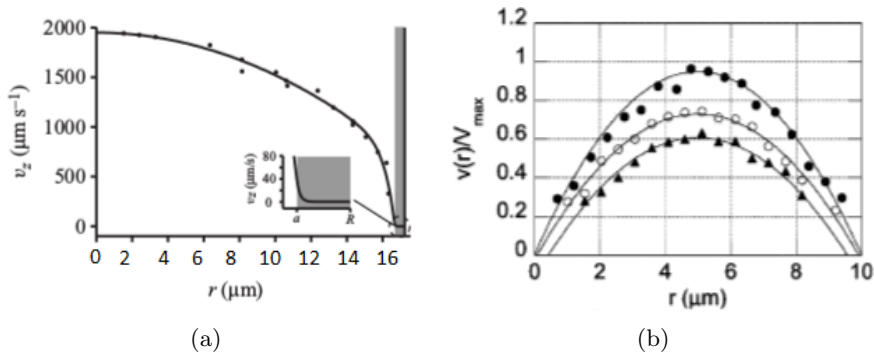


Figure 1.8: Velocity profiles inside capillaries. Velocities of fluorescent beads flowing (a) *in vivo*; (b) in glass microchannels for different brush thicknesses h : (black circle) $h = 0\text{nm}$; (white circles) $h = 200\text{nm}$; (black triangles) $h = 400\text{nm}$. It shows how the thicker is the polymer brush, the slower is the flow. Data in (b) are fitted by a Poiseuille parabola for which the channel radius has been reduced of twice the brush thickness.

1.5 Genesis of our project

The endothelial glycocalyx layer is a composite network, whose role in the blood circulatory system is not limited to chemical signaling nor to a mechanically passive compartment. Indeed, it is *hydrodynamically relevant*, having a repercussion on the in-blood flowing particles and on the streamlines of the surrounding plasma. The theoretical works that we have presented in the previous Section contribute to the description of such multi-faceted system, but the experiments that we have mentioned demonstrate how a complete understanding of the EGL, as well as of simpler artificial polymer brushes, requires additional efforts. In particular, a more detailed description of the hydrodynamics at the interface between the free brush surface and the bulk would be desirable.

Here, we propose the use of numerical simulations, as complementary study to *in vivo* analyses, more realistic but coupled with the unknowns of the complex biological environment, and to *in vitro* microfluidic experiments, highly controllable but unable to reach a resolution on the scale of polymers. Our simulations will probe the dynamics of a dense polymer brush under flow. Indeed, the present work is also a contribution to the wide branch of polymer brushes and propose a relatively simple model to examine their peculiar features under flow, still far from being completely revealed. For example, does the brush enhance or lower the

fluid viscosity? To which extent does it influence the bulk streamlines? How does a grafted polymer network interact with a RBC? In order to tackle such questions, we have designed the project of the present thesis. Enclosing in a same simulation both the hydrodynamics and the polymer dynamics requires a model suitable to grasp physics at the mesoscale. We thus resort to coarse-graining methods and opt for the Dissipative Particle Dynamics (DPD) technique.

We stress again that at the microcirculatory stage, since the RBC size is comparable to the capillary diameter, the EGL mechanical influence on cell dynamics is expected to be more relevant. Therefore our simulations will recreate a microcapillary environment. This choice, in addition, produces advantageous working hypotheses:

1. the flow is laminar and there is no need to take pulsatile flow into account,
2. elasticity of the vessel walls can be neglected,
3. interaction among RBCs can be disregarded, because in tiny tubes they flow one by one.

We also specify that our polymer chains will be freely flexible, that is, no chain flexural rigidity will be taken into account. This decision is not in contrast with the purpose of comparing our results with the EGL. Even if the bending resistance has been considered a distinctive characteristic of the glycocalyx fibers (for example, in Ref. [83,86]), we refer to the concept of a glycocalyx as constituted by “two regions: one thin underlying sieving layer and a much looser outer layer” [59]. Also recalling Fig.1.2(a), the wavy conformation of macromolecules can be recognized. Basically, a single definition on the nature of glycocalyx chain rigidity seems too strict. Here, since our focus is on the interaction of the polymeric matrix with the outer flow and cells and not on its role as mechanotransductor, we are justified in using a softer chain model.

The structure of the present thesis is the following: in Chapter 2 we discuss the numerical method we use and we introduce a coarse-grained model suitable for RBCs to be embedded in a DPD code; in Chapter 3 we present our polymer brush model and validate our code by reproducing well-known brush equilibrium features. Then, in Chapter 4, we show our results for the brush under parabolic flow in slit-pore geometry. We

thoroughly describe the wave forming at the brush surface. In Chapter 5 we report our preliminary results regarding the interaction between our polymer brush and a RBC. Chapter 6 contains a final discussion, before we outline our Conclusion and perspectives for future works.

Résumé (french version)

Le système circulatoire sanguin fournit de l'oxygène et des substances nutritives à toutes les cellules. Comprendre les mécanismes physiques qui régissent le comportement du sang à l'intérieur du dense et très structuré réseau d'artères, veines et capillaires est l'un des problèmes ouverts de la science. Ce sujet n'est absolument pas trivial, parce que différents facteurs contribuent à lui conférer de la complexité. La première source de difficulté, par exemple, réside dans la nature du sang, qui est un fluide complexe. Le sang est en fait une suspension de particules, principalement des globules rouges dans un milieu essentiellement aqueux. Les globules rouges, en plus, sont des particules déformables, ce qui constitue une autre source de difficultés. Et encore, le sang en passant à travers les divers vaisseaux sanguins est soumis à des conditions physiques très variées: dans les grandes artères l'écoulement est pulsatile et turbulent, tandis que dans les petits capillaires il est continu et les effets d'inertie du fluide peuvent être négligés; dans les grands vaisseaux l'hématocrite est élevé et il faut considérer les interactions entre les nombreux globules rouges, tandis que dans les capillaires les globules passent un à la fois; les parois des grands vaisseaux sanguins sont déformables, tandis que les capillaires ont une élasticité négligeable et constituent un confinement bien serré pour les globules rouges qui en conséquence subissent de grandes déformations. Afin de caractériser la rhéologie du sang, il faut donc étudier soit la dynamique du globule seul, soit les effets collectifs entre eux, mais il est important aussi d'inclure dans le modèle la géométrie des bifurcations et l'élasticité des parois. Et pourtant, tenir compte de tous ces effets ne suffit pas. Un autre élément influe sur la circulation sanguine: la morphologie de l'endothélium, c'est-à-dire de la couche la plus interne des parois des vaisseaux sanguins. Cette couche fine de cellules, à une analyse nanométrique, ne se révèle être ni lisse ni uniforme, mais plutôt couverte de polymères greffés. Cette structure polymérique prends le nom de *glycocalyx endothélial*. Le glycocalyx endothélial est un ensemble négativement chargé de macromolécules, principalement composé de glucose et exprimé par les cellules endothéliales. C'est une structure délicate et difficile à visualiser, parce qu'elle se dégrade facilement à la suite des traitements et des protocoles de préparation. Son épaisseur a été établie variant de $0.1\ \mu\text{m}$ à $1\ \mu\text{m}$. Il s'agit d'une valeur comparable à l'épaisseur de la paroi du vaisseau (l'endothélium est inférieur à $0.1\ \mu\text{m}$ d'épaisseur dans les capillaires), alors qu'il n'est pas plus du 10% du diamètre des capillaires les plus petits. Des telles proportions révèlent

que le glycocalyx constitue un compartiment important pour la protection des parois des vaisseaux, sans constituer un obstacle considérable à l'écoulement.

Les composants principaux du glycocalyx endothélial sont: les protéoglycanes, les glycosaminoglycanes et les glycoprotéines, ainsi que des protéines plasmiques absorbées. Les fonctions de base du glycocalyx jouent un rôle important dans les petits vaisseaux ainsi que dans les grands. Il agit comme mécanotransducteur, il régule l'adsorption et la perméabilité des parois capillaires et il influence l'hématocrite et la viscosité du sang. Pour toutes ces raisons il est important de comprendre l'interaction entre les polymères du glycocalyx et les cellules du sang.

Un travail imposant a été consacré tout au long des trente dernières années pour définir un modèle pour le glycocalyx. Chacun de ces modèles saisit une caractéristique clé de cette structure. Néanmoins, le profil d'écoulement à proximité du glycocalyx ou, plus généralement, d'une brosse de polymères, soulève encore quelques questions. Des mesures récentes du profil de vitesse dans le voisinage d'une brosse de polymères en sont un exemple. Notre travail propose un modèle pour obtenir une description détaillée de l'hydrodynamique à l'interface libre d'une brosse polymérique. En effet, le présent ouvrage est également une contribution à la vaste branche de brosses de polymères. On propose un modèle relativement simple pour examiner leurs caractéristiques sous écoulement, encore loin d'être complètement révélé. Par exemple, en quelle mesure et jusqu'à quelle distance peut-elle influencer la vitesse du solvant? La dynamique de la brosse augmente ou baisse la viscosité du fluide? Comment une structure de polymères greffés interagit avec un globule rouge? L'objectif de cette thèse est d'aborder ces questions. Inclure à la fois dans un même code l'hydrodynamique et les détails des polymères exige un modèle approprié qui saisit la physique à l'échelle mésoscopique. Ainsi nous avons recours à une méthode coarse-grained et nous avons opté pour la technique numérique de la Dissipative Particle Dynamique (DPD).

La structure de la présente thèse est la suivante: dans le Chapitre 2, on discute la méthode numérique qu'on utilise et on introduit un modèle coarse-grained approprié et dans lequel on peut incorporer un globule rouge; dans le Chapitre 3, on présente notre modèle de brosse de polymères et on valide le code en reproduisant des propriétés d'équilibre bien établies. Puis, au Chapitre 4, on montre les résultats pour la dy-

namique de la brosse sous flux parabolique dans la géométrie *slit-pore*. On décrit minutieusement la formation d'une onde à la surface de la brosse. Au Chapitre 5, on présente des résultats préliminaires concernant l'interaction entre la brosse et un objet déformable qui représente un globule rouge. Le Chapitre 6 contient une discussion finale, avant de tirer notre Conclusion et décrire nos perspectives des travaux futurs.

Chapter 2

Coarse-graining with Dissipative Particle Dynamics

A Dissipative Particle Dynamics code has been set up to reproduce the dynamics of a simple Newtonian fluid and of a dense polymer brush. Coarse-graining is applied both to solvent particles and monomers. Details of the implementation and the applied boundary conditions to obtain a parabolic flow with no-slip at the walls are analyzed. Moreover, a multi-scale model for Red Blood Cells suitable to be embedded in the DPD frame is presented.

2.1 The choice of the numerical method

A channel coated by a polymer brush and a simple liquid flowing through it represent a case study for polymer out-of-equilibrium dynamics. Moreover, as discussed in the previous Chapter, they constitute a minimal model that can help in clarifying some aspects of blood circulation. A suitable numerical code should include hydrodynamics interactions, which are expected to play a central role in the dynamics of the brush, and at the same time retain a detailed description of the brush filaments. With this premise, the involved scales we want to cover span from nanometers to tens of micrometers. Therefore, a standard full-atom Molecular Dynamics (MD) simulation would be too demanding in computational time and memory capacity; even with the most performing computers,

it would be impossible to reproduce the long-time and long-length scales concerning hydrodynamics. On the other hand, it would be premature to build a continuum model to solve Navier-Stokes equations without having first understood which properties of polymers have a relevant feedback effect on the flow. For those reasons, we opted for an intermediate point of view and operate a coarse-graining of MD following the Dissipative Particle Dynamics (DPD) technique. Indeed, DPD proposes a strategy to coarse-grain liquids reproducing mesoscale dynamics. While a coarse-graining on monomers is, in line with *blob* theory [93,94], a structural operation, on a liquid is not a straightforward concept. The DPD procedure, then, suggests a uniform coarse-graining, applied both to monomers and liquid molecules, and guarantees the correct hydrodynamics with explicit solvent [95,96]. The settled model is, thus, self-consistent.

In the last 15 years DPD has been larger and larger used to investigate free mesoscopic objects, especially polymers. At present, it has been established that equilibrium properties, like the scaling laws (i.e., mass dependent behaviors) describing the typical polymer size and monomer space distribution or the relaxation times that characterizes particle rearrangements are perfectly recovered [97] and DPD can be legitimately used for any kind of polymer systems, from melts [97], to block copolymers [98] and polymers in solution [99,100]. The possibility to simulate a wide range of systems continuously pushes towards technical additions and refinements: DPD including electrostatic interactions [101] or DPD with energy conservation [102] are also available. Together with the increasing interest on biophysics and medical applications, DPD has focused on the modeling of biological membranes and, recently, a coarse-graining for RBC has been proposed [103,104]. We will present such a model in the last Section of the present Chapter, since we will be using it to examine the interaction of a RBC with the polymer brush.

2.1.1 Coarse-graining techniques for liquids

For the sake of completeness, we mention here other mesoscale techniques that have been employed for the simulation of liquids:

- DPD

It is the one we have elected. We dedicate the present Chapter to it. The implementation is similar to that of MD and similar es-camotages can be adopted [105]. Both hydrodynamics and thermal fluctuations are taken into account.

- **Lattice Boltzmann**
Fictitious particles move on a regular lattice at discrete time step. They evolve according to the Boltzmann equation, i. e. to the time evolution of a probability distribution function. A streaming term advects particles along the lattice sides and collisions occur when two particles move to the same lattice node. It is particularly useful in case of complicated boundaries, since it is sufficient to refine the mesh to increase the precision. It is a particle-based method, thus it is easy to parallelize.
- **Multi-Particle Collision Dynamics (alias Stochastic Rotation Dynamics)**
It is an off-lattice particle-based method. The coarse-grained particles are grouped in so-called collision cells and upgraded according to a streaming step and a collision step. During the first step particles move ballistically, while in the second step, velocities of particles contained in a cell are rotated of a fixed angle around a random axis. The rule for the upgrade of velocities guarantees momentum conservation.

2.2 The code

We present here the basis of the DPD technique and the set up model for simulation of a polymer brush made of linear chains and the establishment of a parabolic flow inside the channel. As previously mentioned, the coarse-graining DPD procedure applies to both solvent molecules and polymer monomers, offering the possibility to (i) reproduce hydrodynamic interactions while retaining a detailed view of the brush dynamics on the scale of the coarse-grained monomers; (ii) access both the polymer dynamics, influenced by the imposed flow, and the flow field, perturbed by the presence and motion of the brush (self-consistence).

2.2.1 DPD methodology

DPD is a coarse-graining of MD, employing both spatio-temporal averaging of interaction potentials as well as grouping of atoms into single particles (the DPD particle). It was introduced by Hoogerbrugge and Koelman in 1992 [106] to simulate isothermal Navier-Stokes equations. It thus grasps hydrodynamics interactions and covers bigger timescales and bigger lengthscales than the usual ones reproducible with MD.

Each of the N point-like DPD particles evolves in time according to Newton's equation

$$m\dot{\vec{v}}_i = \sum_{j \neq i}^N \vec{F}_{ij} \quad (2.1)$$

(with obvious choice for symbols). The forces \vec{F}_{ij} acting on pairs does not fit a molecular potential and it is gauged in consequence of the coarse-graining level. It holds three contributions: a conservative one, $\vec{F}^C(r_{ij})$, a dissipative one, $\vec{F}^D(r_{ij})$, and a stochastic one, $\vec{F}^S(r_{ij})$. These are all central forces such that $\vec{F}_{ij} = -\vec{F}_{ji}$, thereby guaranteeing local momentum conservation. All of them act within the same distance range r_c , that is chosen as the lengthscale unit (see Sect. 2.3). The conservative force has the following expression:

$$\vec{F}^C(r_{ij}) = \begin{cases} a_{\alpha\beta} \left(1 - \frac{r_{ij}}{r_c}\right) \hat{r}_{ij} & r_{ij} \leq r_c, \\ 0 & r_{ij} > r_c \end{cases} \quad (2.2)$$

with the definitions $\vec{r}_{ij} = \vec{r}_i - \vec{r}_j$ for the vector distance between the i -th and j -th particle, $r_{ij} = |\vec{r}_{ij}|$ and $\hat{r}_{ij} = \vec{r}_{ij}/r_{ij}$. It is a conservative soft-core repulsive force, corresponding to the following potential

$$V(r_{ij}) = \begin{cases} -a_{\alpha\beta} \left(r_{ij} - \frac{r_{ij}^2}{2r_c} - \frac{r_c}{2}\right) & r_{ij} \leq r_c, \\ 0 & r_{ij} > r_c \end{cases} \quad (2.3)$$

where the constant value $a_{\alpha\beta}r_c/2$ has been added to shift the potential to zero at $r = r_c$. According to standard DPD, the functional shape of Eq. (2.2) comes from averaging a Lennard-Jones 12-6 potential over short time scales and small lengthscales, thus measuring the effective potential between *clusters* of liquid molecules [107]. Fast dynamics (the number of collisions with neighbors, known as the *cage effect* of simple liquids) is averaged out, resulting in an only-repulsive interaction. The softness is justified by the *blob* nature of DPD particles that, containing also empty space, should have the possibility to overlap. We note that the absence of divergences in Eq.(2.3) entails the advantage of DPD with respect to MD: while a hard-core potential imposes a maximum integration time-step to avoid excessive forces, the soft-core interaction allows for bigger time step values. The constant $a_{\alpha\beta}$ measures the force between two completely overlapping particles, where the indexes α, β indicate the particle type

(solvent or polymer, in our case). It controls the density fluctuations of the system and it is casted from the compressibility of the modeled fluid (see App.A).

The two other extra forces account for the loss of details in the coarse-graining procedure, namely the huge amount of collisions occurring between real molecules and constituting the microscopic foundation of transport properties, such as viscosity and diffusivity. The dissipative force takes the following form:

$$\vec{F}^D(r_{ij}) = -\gamma w^D(r_{ij})(\hat{r}_{ij} \cdot \vec{v}_{ij})\hat{r}_{ij}, \quad (2.4)$$

where the standard choice in literature for the “weight function” $w^D(r_{ij})$ is:

$$w^D(r_{ij}) = \begin{cases} \left(1 - \frac{r_{ij}}{r_c}\right)^2 \hat{r}_{ij} & r_{ij} \leq r_c, \\ 0 & r_{ij} > r_c. \end{cases} \quad (2.5)$$

Other choices for the power law of the weight function tune the liquid viscosity [108]. Precisely, Eq.(2.4) answers for the energy loss, introducing a friction among particles proportional to the relative velocity $\vec{v}_{ij} = \vec{v}_i - \vec{v}_j$ and to a factor γ that depends on the temperature T . To balance the dissipative force, a random force is also necessary:

$$\vec{F}^S(r_{ij}) = \sigma w^S(r_{ij})\theta_{ij}(\Delta t)^{-\frac{1}{2}}\hat{r}_{ij} \quad (2.6)$$

where σ is related to temperature, $w^S(r_{ij})$ is another weight function and θ_{ij} is a random number extracted from a gaussian distribution having the following characteristics:

- zero averaged: $\langle \theta_{ij}(t) \rangle = 0$
- independent in time and among couples: $\langle \theta_{ij}(t)\theta_{lm}(t') \rangle = (\delta_{il}\delta_{jm} + \delta_{im}\delta_{jl})\delta(t - t')$.

The condition $\theta_{ij} = \theta_{ji}$ has to be verified in order to locally conserve momentum. The factor $1/\sqrt{\Delta t}$ in Eq. (2.6) comes from the discretization procedure of a Wiener process and ensures that the particle self-diffusion coefficient is independent from the time step value [109]. The two forces $\vec{F}^D(r_{ij})$ and $\vec{F}^S(r_{ij})$ act as a thermostat.

It has been proved by Español and Warren [110] that to reproduce the correct equilibrium probability distribution $f_{eq}(r_i, p_i)$ of the NVT

ensemble

$$f_{eq}(r_i, p_i) \propto \exp \left(-\frac{1}{k_B T} \left(\sum_i \frac{p_i^2}{2m} + \sum_{i>j} V(r_{ij}) \right) \right), \quad (2.7)$$

with p_i the i -th particle momentum and V the potential arising from F^C , the dissipative and random forces have to verify two constraints:

$$w^D(r_{ij}) = [w^S(r_{ij})]^2 \quad \text{and} \quad \gamma = \frac{\sigma^2}{2k_B T}. \quad (2.8)$$

In addition to these basic DPD forces, other kinds of interaction can be included in the DPD frame according to the specific simulated system. In the present case, to mimic polymers, linear chains of DPD particles are connected by a finitely extensible nonlinear elastic potential (FENE) [111]

$$\vec{F}_{ij}^{FENE} = -2kR^2 \frac{r_{ij} - r_{eq}}{R^2 - (r_{ij} - r_{eq})^2} \hat{r}_{ij} \quad r_{ij} - r_{eq} < R \quad (2.9)$$

where k is the spring constant, r_{eq} the neighbor equilibrium distance and R the maximum allowed extension. An extra monomer is added to each chain as *anchor*, i.e. grafting point. Grafting point coordinates are randomly chosen from a uniform distribution and located on a flat surface $z = z_{wall}$ according to the imposed grafting density σ_{graft} , defined as $\sigma_{graft} = N_{ch}/(L_x L_y)$ with N_{ch} the number of chains composing the brush. The anchor centers of mass are aligned with the wall z coordinate and their position is not updated. Note that polymers are non-ideal ones since they also interact via the DPD repulsive force, that operates as an excluded volume potential. The values for all the parameters will be specified in Sect.2.3.

2.2.2 Details on the algorithm

The code integrates the Newton's equation, Eq. (2.1), for each particle using the finite difference Velocity Verlet (VV) algorithm. The VV algorithm calculates at each time step $t = n\Delta t$, $n = 0, 1, 2, \dots$, both particle position $\vec{r}_i(t)$ and velocity $\vec{v}_i(t)$. In its original form it is composed of three steps (in the following we omit the vector symbol $\vec{\cdot}$ for practical reasons):

1. $r_i(t + \Delta t) = r_i(t) + v_i(t)\Delta t + \frac{a_i(t)}{2}\Delta t^2$

$$\begin{aligned}
2. \quad & F_i(t + \Delta t) = F_i(r(t + \Delta t)) & (2.10) \\
3. \quad & v_i(t + \Delta t) = v_i(t) + \frac{a_i(t + \Delta t) + a_i(t)}{2} \Delta t
\end{aligned}$$

where $a_i(t) = F_i(t)/m$ is the acceleration of the i -th particle calculated from the total force F_i acting on the mass m . With this structure the algorithm has an error due to discretization of order $O(\Delta t^3)$. In the third integration step the presence of the updated acceleration $a(t + \Delta t)$ confers to the algorithm the two important features of being reversible and symplectic.

However, since in DPD forces depend also on velocities, the reported algorithm (2.10) must be modified [109]. Another step is then introduced before force calculation, involving fictitious velocities evaluated at an intermediate time between t and $t + \Delta t$. Thus, the DPD Velocity Verlet reads:

$$\begin{aligned}
1. \quad & r_i(t + \Delta t) = r_i(t) + v_i(t)\Delta t + \frac{a_i(t)}{2}\Delta t^2 \\
2. \quad & \tilde{v}_i \equiv v_i(t + \lambda\Delta t) = v_i(t) + \lambda a_i(t)\Delta t & (2.11) \\
3. \quad & F_i(t + \Delta t) = F_i(r(t + \Delta t), \tilde{v}) \\
4. \quad & v_i(t + \Delta t) = v_i(t) + \frac{a_i(t + \Delta t) + a_i(t)}{2}\Delta t
\end{aligned}$$

In the literature the common choice is $\lambda = 1/2$ [109]. Applied to DPD, the error of such an algorithm cannot be determined *a priori* because of the stochastic force. Then, a temperature check can serve as control, given that the system temperature T has to keep constant to the set value (see Eq.(2.8)). We show a typical temperature plot in Fig.2.1.

2.2.3 The system geometry and the boundary conditions

Our simulated system is composed by N particles and is enclosed in a parallelepiped box of sides L_x, L_y, L_z . A fraction N_m of the total number N , is reserved to monomers. With N_{ch} polymers chains composed by n (coarse-grained) monomers, it holds $N_m = nN_{ch}$ (anchors not counted). For the sake of ease and computational time, indeed, we attach polymers only to the bottom wall $z_{wall} = 0$ (see Fig. 2.3). On the x - and y -axes we impose periodic boundary conditions, while at $z = 0$ and $z = L_z$ two impenetrable parallel walls of infinite mass are set, thus obtaining a *slit-pore* geometry. DPD forces are active between particles and walls within

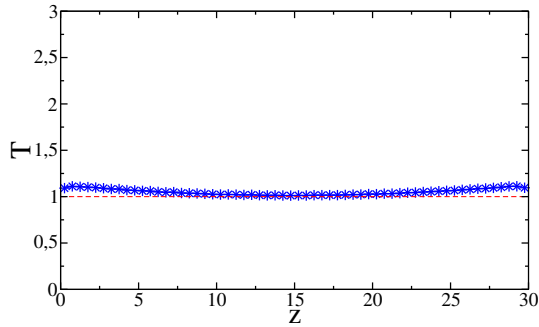


Figure 2.1: Temperature plot (blue stars) for the solvent in a slit-pore channel, $L_x = 30$, $L_y = 5$ and $L_z = 30$. The temperature is calculated as $k_B T = \frac{m}{3} \langle (v_{i,x} - \langle v_x \rangle)^2 + (v_{i,y} - \langle v_y \rangle)^2 + (v_{i,z} - \langle v_z \rangle)^2 \rangle$, where $\langle \dots \rangle$ indicates the ensemble average over fluid particles $i = 1, \dots, N_{fl}$, and $k_B = 1$. At the wall, since the bounce back method (see Sect.2.2.3 of the main text) produces a bigger velocity dispersion, we observe a temperature that is several percent higher than the set one ($T = 1$, red line).

the same cut-off radius r_c according to the following expressions [112]:

$$\begin{aligned} \vec{F}_i^C &= a_w \left(1 - \frac{|\bar{z}_i|}{r_c} \right) \hat{z}_i \\ \vec{F}_i^D &= -\gamma \left(1 - \frac{|\bar{z}_i|}{r_c} \right)^2 v_{i,z} \hat{z}_i, \\ \vec{F}_i^S &= \sigma \left(1 - \frac{|\bar{z}_i|}{r_c} \right) \theta_{ij}(\Delta t)^{-\frac{1}{2}} \hat{z}_i \end{aligned}$$

with $\bar{z}_i = z_i - z_{wall}$, where $z_{wall} = 0, L_z$ and z_i and $v_{i,z}$ the z -component of, respectively, the i -th particle position and velocity. The conservative force coefficient a_w is typically lower than the one set between particles in order to avoid artificial depletion layers along walls [113]. The alignment of all these forces along \hat{z} is simpler to implement than the arrangement of one or more layers of frozen particles to mimic the rigid wall and it does produce the expected boundary behaviors.

In order to produce a parabolic flow inside the channel (e.g. along the x direction) a constant acceleration $\vec{A} = A\hat{x}$ is applied to all fluid particles:

$$m\dot{\vec{v}}_i^{fluid} = \vec{F}_{ij}^{fluid} + m\vec{A}. \quad (2.12)$$

Analytically, this choice is fully equivalent to the application of a pressure drop at the inlet/outlet of the channel, but it is easier to handle

in simulations where periodic boundary conditions are needed. In turn, these fluid particle exchange momentum with the chains, dragging them. Different values of A allow us to probe different dynamic regimes. We recall that in slit-pore geometry a laminar flow has a parabolic shape:

$$\begin{aligned} v_x(z) &= \frac{\Delta P}{2\eta L_x} \left(\left(\frac{L_z}{2} \right)^2 - \left(z - \frac{L_z}{2} \right)^2 \right) \\ &= \frac{\rho_m A}{2\eta} \left(\left(\frac{L_z}{2} \right)^2 - \left(z - \frac{L_z}{2} \right)^2 \right), \end{aligned} \quad (2.13)$$

obtained as stationary solution of the Navier-Stokes equation. Here, ρ_m is the mass density.

Given the softness of the conservative interaction potential, a repulsive force of the kind in Eq. (2.2) is not enough to prevent particles from escaping the box. It is then necessary to implement an additional mechanism to bring back particles that cross the wall line. The literature reports three different options [113, 114]:

1. *specular reflection*, in which the normal component of the velocity of the particle hitting the wall is reversed while the parallel component is conserved

$$v_{\parallel} \rightarrow v_{\parallel} \quad , \quad v_{\perp} \rightarrow -v_{\perp} \quad (2.14)$$

2. *thermal wall*, in which new velocity components are randomly sampled from the following distributions:

$$\begin{aligned} f(v_{\parallel}) &= \sqrt{\frac{m}{2\pi k_B T}} e^{-(mv_{\parallel}^2)/(2k_B T)} \\ f(v_{\perp}) &= \frac{m}{k_B T} |v_{\perp}| e^{-(mv_{\perp}^2)/(2k_B T)} \end{aligned}$$

3. *bounce back reflection*, in which the whole particle velocity vector is reversed

$$\vec{v} \rightarrow -\vec{v}. \quad (2.15)$$

We use the last one. The bounce-back mechanism, by construction, is consistent with the no-slip condition at the wall

$$\vec{v}_{\parallel, solvent}(z_{wall}) = 0, \quad (2.16)$$

as proved by Fig. 2.2, showing the comparison with thermal wall reflection for the same system. On the other hand, the bounce back produces a

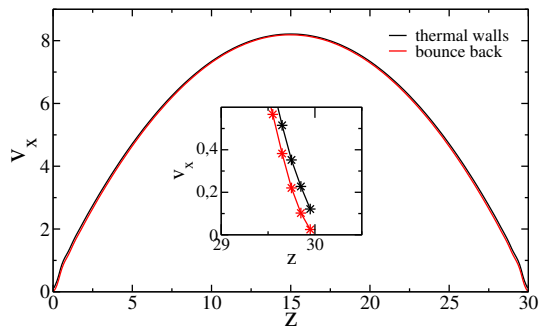


Figure 2.2: A comparison between velocity profiles $v_x(z)$ in a slit-pore channel, $L_x = 30$, $L_y = 5$ and $L_z = 30$, obtained with two different reflection mechanisms at the walls: (red) bounce back and (black) thermal wall. The inset highlights how the no-slip condition is better verified by the bounce back procedure. The applied acceleration is $A = 0.02$.

bigger velocity dispersion at the wall [114] where the temperature is, on consequence, some percent higher than the fixed one (see again Fig. 2.1).

2.3 DPD and physical units

We chose the DPD units such that $r_c = 1$, $m_i = 1$ and $k_B T = 1$. The integration time step is $\Delta t = 0.02$. We underline that such value is at least one order of magnitude bigger than the usual ones set for MD simulations and, thanks to the softness of the potential, is enough to make the system reach the equilibrium/steady state. We set the system number density $\rho = N/(L_x L_y L_z) = 3$ [109]. This choice is motivated by the following compromise: low density values ($\rho < 2$) make the used relation Eq.(A.4) be invalid, while high density values increase the computational cost since the number of particles inside the interaction volume r_c^3 rises. The number of monomers per chain ranges from $n = 20$ to $n = 45$ and the grafting density σ_{graft} spans from $\sigma_{graft} = 0.1$ to $\sigma_{graft} = 1.5$. Since the total number of DPD monomers N_m is subtracted to the total amount of particle N , the actual number of solvent particles is $N_s = N - N_m = \rho L_x L_y L_z - n \sigma_{graft} L_x L_y$. Following Ref. [109], we fix the solvent-solvent interaction parameter a_{SS} relating it to the dimensionless compressibility of water $\kappa_T^{-1} = 1/(\rho k_B T \kappa_T)$, where κ_T is the fluid compressibility. As discussed in App. A, a comparison between the compressibility calculated from the equation of state of the simulated

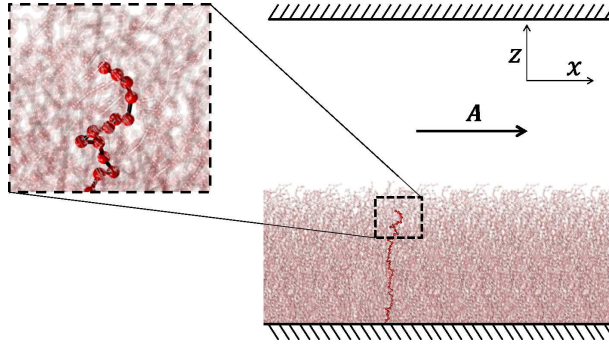


Figure 2.3: Schematic representation of the investigated slit-pore system. Polymers are grafted at the bottom wall $z = 0$ while the rest of the channel is occupied by solvent particles. An additional sketch is provided with a zoom on a typical chain (highlighted in red). The constant acceleration A is applied along the x axis to all solvent particles.

DPD system and the experimental data suggests $a_{SS} = 75k_B T / \rho r_c^4 = 25$. We assume that the polymer-polymer interaction parameter has the same value (e.g. $a_{SS} = a_{PP}$), while we select a smaller value for the solvent-polymer parameter $a_{SP} = 20$ (*good solvent* conditions). For the interaction with walls we set $a_w < a_{SS}$ to avoid an artificial depletion zone along the walls and we choose $a_w = 6$. The noise amplitude is fixed to $\sigma = 3$, as in previous literature [109]. It is worth noticing that with higher values for σ the code takes more time to reach the equilibrium/steady state. For the FENE potential we use $r_{eq} = 0.86$, $R = 1$ and $k = 50$.

As in all scale-free mesoscale techniques, also in DPD the choice for the physical units depends on the desired level of coarse-graining and it is not fixed *a priori* since the DPD potential, Eq.(2.3), is independent of the specific physical system. We establish units by comparison with macroscopic properties of our reference physical system (i.e., endothelial glycocalyx in water). We fix the physical lengthscale l_{phys} relating the spacing between different filaments of the glycocalyx network, $d_{phys} = 20\text{nm}$ [14] with the average distance between anchor points of our brush, $d_{DPD} = \sqrt{1/\sigma_{graft}} = 0.82$:

$$l_{phys} = d_{phys}/d_{DPD} = 24 \times 10^{-9}\text{m}.$$

We underline that with this choice also the brush thickness is in the range of endothelial glycocalyx (100 nm \div 1000 nm [37]).

As for the physical mass scale m_{phys} and physical time scale t_{phys} , we exploit the comparison between viscosities and between energies. The viscosity of water η_{phys} is $\eta_{phys} = 10^{-3}\text{Pa}\cdot\text{s}$ at 300K and the DPD viscosity η_{DPD} in a bare channel, estimated from the slit-pore velocity profile relation $\eta = m\rho A(L_z/2)^2/2v_{max}$, where v_{max} is the maximum velocity, corresponds in our case to $\eta_{\text{DPD}} = 0.84$. The physical energy scale is defined as $e_{phys} = k_B T_{phys}$, with $T_{phys} = 300\text{K}$. Thus we can write down the following relations:

$$m_{phys} = \frac{\eta_{phys}}{\eta_{\text{DPD}}} t_{phys} l_{phys},$$

$$t_{phys} = \frac{l_{phys}}{v_{phys}} = \frac{l_{phys}}{\sqrt{\frac{3k_B T_{phys}}{m_{phys}}}},$$

from which we extract

$$t_{phys} = \frac{l_{phys}^3}{3k_B T_{phys}} \frac{\eta_{phys}}{\eta_{\text{DPD}}} = 1.8 \times 10^{-6}\text{s}, \quad (2.18a)$$

$$m_{phys} = \frac{\eta_{phys}}{\eta_{\text{DPD}}} t_{phys} l_{phys} = 5.1 \times 10^{-17}\text{kg}. \quad (2.18b)$$

We underline that the key reason for the DPD speed-up with respect to MD simulations can be summarized by saying that *the Schmidt number for the simulated fluid is low* [115]. By definition, the Schmidt number Sc is the ratio of the kinematic viscosity over the self-diffusion coefficient:

$$Sc = \frac{\nu}{D} = \frac{\eta}{\rho D}. \quad (2.19)$$

For a liquid it should be of order $O(10^3)$ since momentum transport is more efficient than mass transport. The DPD methodology, averaging over fast time scales and short length scales, produces instead a gas-like Schmidt number $Sc_{\text{DPD}} \sim O(1)$. This is actually the consequence of the soft-core repulsive DPD interaction potential, namely the removal of the cage effect of liquids, as discussed in Sect.2.2.1. In conclusion, DPD loses atomistic details but it is proved to be a coherent coarse-graining method.

2.4 The coarse-graining of the RBC membrane

As discussed in the previous Chapter, the interaction between polymer brushes and deformable flowing objects has been not elucidated yet. We

are not aware of previous numerical studies addressing such problem. Here, we consider the specific case of one RBC, as, flowing through microcapillaries, approaches the space domain of the endothelial glycocalyx. The size of a polymer is negligible with respect to the cellular scale of a RBC, nevertheless it is legitimate to wonder if the long-ranged hydrodynamics could trigger interactions that propagate the mechanical response of a continuum-like structure, as a dense polymer brush, towards the deformable surface of the cell. In order to investigate such questions, we exploit a coarse-grained model of the RBC membrane that can be embedded in our DPD code and therefore coupled with hydrodynamics and grafted polymers. Created by Pivkin and Karniadakis [116] and subsequently refined by Fedosov and coworkers [104], we present it hereafter.

The cell is considered as a closed surface containing a DPD fluid of viscosity η_{in} and immersed in a DPD fluid of viscosity η_{out} . At physiological conditions, the viscosity contrast is $\lambda > 1$ (see Sect.1.3.2 for the definition). The membrane consist of a network of N_v vertices of coordinate \vec{r}_i interacting with each other. Forces take into account the visco-elasticity and bendability of the membrane constituted by the phospholipidic bilayer and its cytoskeletal support. Membrane non extensibility and impermeability are achieved by imposing a volume conservation constraint, as well as a local and a global area conservation constraints. Thus, the free energy V_{MEMB} of the membrane collects all the following contributions:

$$V_{MEMB} = V_{elastic} + V_{bending} + V_{area}^{local} + V_{area}^{global} + V_{volume}. \quad (2.20)$$

The viscosity term, being a dissipative one, is not expressed by a potential and will be introduced directly in Sect. 2.4.2 among forces.

2.4.1 The stress-free triangulation

Building up the equilibrium membrane means basically to define a surface triangulation and give to it the desired shape.

Triangulation A uniform triangulation is produced assigning coordinates to each vertex point and fixing the links to its neighbors, such that triangles are as regular as possible. To this end, we make use of the *point charges* method, sketched in Fig. 2.4. It consists in generating a set of randomly distributed points on a spherical surface (Fig. 2.4.(a)) and in treating these points as electric charges: defined an electrostatic-

like potential, $\Phi = \sum_i \phi_i = \frac{1}{2} \sum_{i,j \neq i} \frac{1}{r_{ij}}$ (where $i, j = 1, \dots, N_v$), we let the system relax to the energy minimum while points are constrained on the sphere (Fig. 2.4.(b)). This procedure assures a uniform distribution of points. Finally, the convex hull is calculated, namely the minimal convex surface that contains all points (and therefore all links between them) (Fig. 2.4.(c)). It is basically a set of triangles approximating the surface. In this way, a membrane triangle tessellation is drawn and links between points are univocally indexed. For N_v vertices, the number of triangles N_t is $N_t = 2(N_v - 2)$. The number of links N_s , coincident with the number of dihedral, is $N_s = 3(N_v - 2)$.

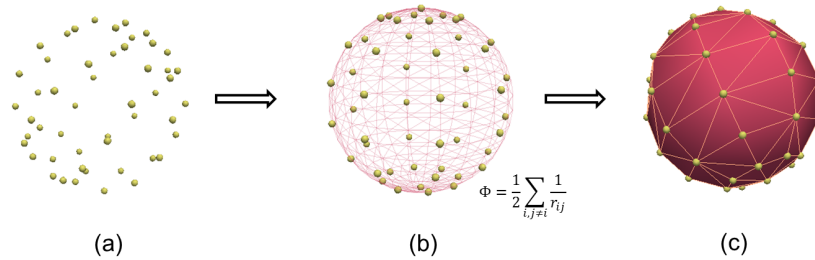


Figure 2.4: An example of the three-step *point charge* method used to generate a uniform surface triangulation: (a) points are randomly distributed all over the surface; (b) by using an electrostatic-like interaction potential between pairs, $\phi(r_{ij}) = 1/r_{ij}$, points are uniformly redistributed on the surface; (c) the convex hull is calculated, thus a list of triangles approximating the surface is associated to the point set.

Desired shape It is assumed that at equilibrium the membrane has the RBC typical discoidal biconcave shape. Thus, we impose the following relationship for the Cartesian coordinates of each vertex $\vec{r}_i = \{x_i, y_i, z_i\}$:

$$x_i = \bar{x} \pm D_0 \sqrt{1 - \frac{4(y_i^2 + z_i^2)}{D_0^2}} \left[a_0 + a_1 \frac{y_i^2 + z_i^2}{D_0^2} + a_2 \frac{(y_i^2 + z_i^2)^2}{D_0^4} \right] \quad (2.21)$$

where coordinates $\{\bar{x}, y_i, z_i\}$ correspond to a disk of radius $D_0/2$. The effect of such operation is schematized in Fig.2.5(a). The choice of coordinates in Eq.(2.21) fixes the RBC initial orientation: comparing with the reference system initially defined (Fig.2.3), the disk is transversal to the channel length. We finally proceed with a second relaxation procedure. Indeed, the final triangulation, shown in Fig.2.5(b), is found by

minimizing the elastic energy $V_{elastic}$: if a random exchange between the diagonals of adjacent triangles lowers it, the switch is done and, if a small random displacements of vertices, again, turns to be more energetically favorable, vertex positions are updated (it should be taken care, for this second move, that vertex new position has not to escape the previously assigned discoidal shape). Solvent is not considered at this stage.

It is important to note that such triangulation cannot be perfectly regular: triangle sides can have different lengths and vertices does not necessarily display a 6-fold symmetry, as highlighted in Fig.2.5(b). Therefore the use of a single value for the equilibrium distance l_0 of $V_{elastic}$ (see Sect.2.4.2 for the definition) would introduce artificial stresses on the membrane, inducing unphysical bucklings on the surface. To eliminate such anomalies, we use the stress-free variation [104, 117]. According to such procedure, a loop over the N_s links records the equilibrium distances l_0^s , $s = 1, \dots, N_s$, for each dihedral and the implementation of the cell dynamics will consider the effective l_0 from such distribution. It is important to note that a distribution of equilibrium bond lengths l_0^s implies a distribution for all the quantities depending on l_0 . We will explicit them in Eqs.(2.34) and (2.36), but here we declare them in advance: l_m , k_p and A_0 .

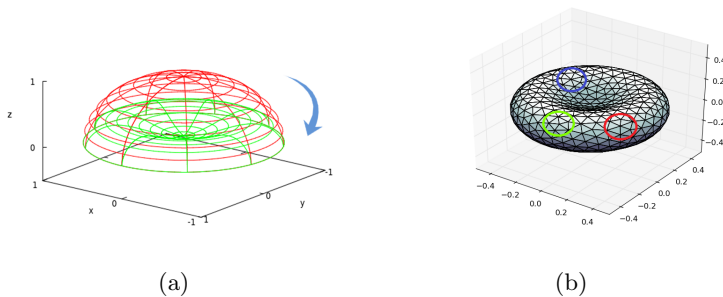


Figure 2.5: Towards a plausible shape of a healthy red blood cell at equilibrium: (a) a spherical distribution of points is turned in a discoidal biconcave distribution by acting with Eq.(2.21) on one point coordinate (to obtain the plotted image the x and z coordinates of the mentioned equation have been exchanged); (b) three dimensional representation of the discoidal biconcave shape finally obtained. Here, $N_v = 500$. As underlined by the colored circles, the triangulation is not perfectly isotropic: points are indicated with 6 neighbors (red), with 5 neighbors (green) and with 7 neighbors (blue).

2.4.2 Membrane energy

We now give an explicit form to the energy terms describing membrane interactions (viscosity term excluded). Forces on each vertex i , $i = 1..N_v$, will be then calculated as $\vec{f}_i = -\partial V(\vec{r}_i)/\partial \vec{r}_i$. For the ease of notation, we write the following potentials using l_0 , but we recall that the code use different values l_0^s , $s = 1..N_s$, according to the membrane stress-free variation (see previous Subsection).

Elastic term Several expressions have been considered in previous works [104, 116]. We choose the following:

$$V_{elastic} = \sum_{i \in 1..N_v} \left\{ -\frac{k_s}{2} \ell_m^2 \log \left[1 - \left(\frac{r_{ij}}{\ell_m} \right)^2 \right] - \frac{k_p}{r_{ij}} \right\} \quad (2.22)$$

where $\vec{r}_{ij} = \vec{r}_i - \vec{r}_j$ is the vector distance between vertices i and j and $r_{ij} = |\vec{r}_{ij}|$. The first term in brackets is an attractive FENE potential, where the parameter ℓ_m is the maximum allowed extension; the second one is a repulsive elastic potential. The equilibrium distance l_0 is thus given by $(\partial V_{elastic}/\partial r_{ij})_{l_0} = 0$. This latter condition will turn to be useful in the following for the calculation of k_p in Eq.(2.34).

Bending term The bending energy is depending on the triangle relative orientation:

$$V_{bending} = \sum_{s \in 1..N_s} k_b [1 - \cos(\theta_s - \theta_0)] \quad (2.23)$$

where θ_s is the angle between the normal vectors of two adjacent triangles of common edge s and θ_0 is the spontaneous angle. For a generic triangle T_{ijk} the normal vector $\vec{\xi}$ is calculated as $\vec{\xi} = \vec{a}_{ji} \wedge \vec{a}_{ki}$, where $\vec{a}_{ij} = \vec{r}_i - \vec{r}_j$.

Area conserving terms The area constraints have the form of elastic potentials. The local constraint reads:

$$V_{area}^{local} = \sum_{t \in 1..N_t} k_d \frac{(A_t - A_0)^2}{2A_0} \quad (2.24)$$

where A_0 is the equilibrium triangle area and A_t is the instantaneous one. We define $A_t = |\vec{\xi}|/2$, with $\vec{\xi}$ the triangle normal vector. The global

constraint yields:

$$V_{area}^{global} = k_a \frac{(A - A_0^{tot})^2}{2A_0^{tot}} \quad (2.25)$$

where A_0^{tot} is the total surface area and A is the instantaneous one $A = \sum_{t \in 1 \dots N_t} A_t$.

Volume conserving term For the constant volume constraint we exploit, again, an elastic potential:

$$V_{volume} = k_v \frac{(V - V_0^{tot})^2}{2V_0^{tot}} \quad (2.26)$$

where V_0^{tot} is the equilibrium total volume, while the instantaneous total volume is $V = \sum_{t \in 1 \dots N_t} V_t$. Here, the volume V_t is the one associated to each triangle, $V_t = (\vec{\xi} \cdot \vec{t}_c)/6$ where \vec{t}_c is the triangle center-of-mass $\vec{t}_c = (\vec{r}_i + \vec{r}_j + \vec{r}_k)/3$.

Viscosity term To mimic the membrane viscosity both a dissipative and a random force are computed between neighbor vertices, as within the usual spirit of DPD. In addition to the central term, proportional to a dissipation factor γ_C , a new term proportional to γ^T is included to enhance viscosity: it is non-central but still depending on the relative velocity \vec{v}_{ij} . As consequence, the random force, too, will gain another contribution:

$$\begin{aligned} \vec{f}_{ij} &= -\gamma^T \vec{v}_{ij} - \gamma^C (\vec{v}_{ij} \cdot \hat{r}_{ij}) \hat{r}_{ij} \\ &+ \sqrt{2k_B T} \left(\sqrt{2\gamma^T} \frac{d\bar{W}_{ij}^S}{dt} + \sqrt{3\gamma^C - \gamma^T} \frac{tr[dW_{ij}]_{\parallel}}{3dt} \right) \hat{r}_{ij} \end{aligned} \quad (2.27)$$

where $d\bar{W}_{ij}^S$ is the traceless symmetric part of the Wiener increment matrix and $tr[dW_{ij}]$ is its trace. For the Wiener increment it holds $dW_{ij}/dt = \theta_{ij}$, where θ_{ij} is a random number from a Gaussian distribution having the same features listed for Eq.(2.6).

The expressions for the corresponding forces are listed in App. B.

2.4.3 Boundary conditions and cylindrical geometry

Impermeability of the membrane is conferred by avoiding at each time step that internal or external solvent particles cross the membrane. In case of crossing, a bounce-back mechanism calculates the particle new ve-

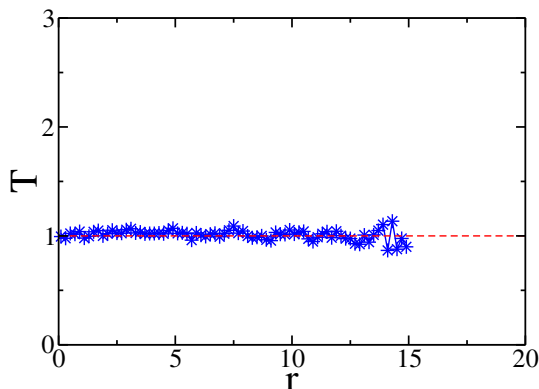


Figure 2.6: Temperature plot in cylindrical pore (blue stars) compared to the set value $T = 1$ (red line). The temperature is calculated as $k_B T = \frac{m}{3} \langle (v_{i,x} - \langle v_x \rangle)^2 + (v_{i,y} - \langle v_y \rangle)^2 + (v_{i,z} - \langle v_z \rangle)^2 \rangle$, where $\langle \dots \rangle$ indicates the ensemble average over fluid particles $i = 1, \dots, N_{fl}$, and $k_B = 1$. The pore sizes are $L_x = 10$, $L_y = L_z = 30$ and the applied acceleration is $A = 0.005$. Temperature keeps constant along the channel radius, as it must be. Slight fluctuations at $r = 5$ are due to lower statistics at the center than at the channel periphery.

locity. Vertex velocities, instead, are not updated: the cell is considered as infinitely massive. The algorithm to implement these boundary conditions is reported in App.C and it has to be repeated in order to check possible multiple collisions. Here, we underline that the bounce-back rule in this case is not simply $\vec{v}_i \rightarrow -\vec{v}_i$, but rather $\vec{v}_i \rightarrow 2\vec{v}' - \vec{v}_i$ with \vec{v}' the velocity associated to the triangle which the i -th solvent particle collides with. This choice guarantees, by construction, the new no-slip condition:

$$v_{solvent,\parallel} = v_{RBC} \quad \text{on the membrane} \quad (2.28)$$

where the subscript \parallel indicates the velocity component that is tangential to the membrane.

Since we focus especially on the RBC deformations, it is appropriate to restore the system axial symmetry and switch from a slit-pore to a cylindrical-pore. The channel radius will be indicated as $R = L_y/2 \equiv L_z/2$. We recall that in this geometry the expected velocity profile is the Poiseuille one:

$$v(r) = \frac{\rho A}{4\eta} (R^2 - r^2). \quad (2.29)$$

The increased friction, due to the presence of a larger wall surface with respect to the case of a slit-pore, is paid with a factor 4 instead of 2 at

denominator. A fit of the velocity profile obtained from a test simulation provides the estimation of the viscosity: $\eta = 0.9$, a slightly different value from the one obtained in the slit-pore geometry for the same DPD parameter values. Figure 2.6 shows a typical temperature plot.

In order not to introduce curvature effects on the brush, the choice of lengthscales should verify the following condition:

$$\frac{h_b}{R} \ll 1 \quad (2.30)$$

where h_b is the brush height. Relation 2.30 assures that, locally, polymers behave as on a flat surface.

2.4.4 Coarse-graining level and physical units

The coarse-graining level for the RBC membrane is fixed by the vertex number N_v . It can span within the range $500 \leq N_v \leq 27000$, according to ref. [116]. The upper limit, $N_v = 27000$, represents the so-called *spectrin-level* model. The spectrin-level model basically considers a number of vertices that equals the number of cytoskeleton junctions in a real RBC. The average equilibrium spring length, therefore, is $l_0 = 75\text{nm}$. Of course, even a fully-detailed network, as the spectrin-level one, differs from a real membrane reproduction: with its almost perfect 6-fold geometry, it does not take into account the cytoskeleton irregularities and it rather represents an effective spectrin network. On the other hand, a good resolution for the cell dynamics and deformations is already achievable conforming the vertex number to the lower limit $N_v = 500$. The average distance between vertices will be $l_0 = 300 - 500\text{nm}$. The model by Karniadakis and Fedosov provides the necessary relations to tune parameters according to the chosen coarse-graining level N_v and the physical quantities listed in Tab.1.1 for a real RBC. For this purpose, it calculates elastic moduli and geometrical properties for a perfect 6-fold mesh of equilateral triangles and equates these quantities with the RBC proper ones. We refer the reader to Refs. [104,117,118] for the derivations and report here directly the relations we have used. For the sake of clarity, we consider separately the model parameters that do not depend on the membrane coarse-graining and the parameters that do depend on it.

Parameters that do not depend on the coarse-graining level N_v

The following parameters are directly linked to the macroscopic properties

μ_0 , η_m and k_c of a RBC membrane:

$$k_s = \frac{4\mu_0}{\sqrt{3}} \frac{(1 - x_0^2)^2}{3 - x_0^2}, \quad (2.31)$$

$$k_b = 2 \frac{k_c}{\sqrt{3}}, \quad (2.32)$$

$$\gamma_T = \frac{12}{13\sqrt{3}} \eta_m, \quad (2.33)$$

where the last one follows from the choice $\gamma_C = \gamma_T/3$ [104]. Here, $x_0 = l_0/l_m$ is the ratio between the equilibrium distance and the maximum extension. It is fixed to $x_0 = 1/2.05$ [104]. For the total area and volume, it simply holds $A_{0,RBC}^{tot} = A_{0,DPD}^{tot}$ and $V_{0,RBC}^{tot} = V_{0,DPD}^{tot}$. As for the constraints forces, the relations $k_a + k_d \gg \mu_0$ and $k_v \gg 1$ are imposed to obtain a nearly incompressible membrane.

Parameters that do depend on the coarse-graining level N_v Considering the membrane as a surface of equilateral triangles with side l_0 , the total surface A_0^{tot} can be expressed as $A_0^{tot} = N_t A_0 = 2(N_v - 2)\sqrt{3}l_0^2/4$. Therefore $l_0 = \sqrt{2A_0^{tot}/\sqrt{3}(N_v - 2)}$. This means that l_0 , as well as all the other parameters expressed through it, is coarse-graining dependent. However, we recall that for a stress-free membrane is opportune to set a distribution of effective equilibrium distances l_0^s , $s = 1, \dots, N_s$, calculated from the relaxed triangulation. Thus, also the following quantities will be adjusted for each bond:

$$l_m^s = \frac{l_0^s}{x_0} \quad s = 1, \dots, N_s \quad (2.34)$$

$$k_p^s = k_s (l_0^s)^3 \frac{(l_m^s)^2}{(l_m^s)^2 - (l_0^s)^2} \quad s = 1, \dots, N_s \quad (2.35)$$

where the last relation is obtained by imposing $(\partial V_{elastic}/\partial r_{ij})_{l_0^s} = 0$. Similarly, an equilibrium area is evaluated for each triangle from the Heron's formula knowing the triangle sides l_0^i , l_0^j and l_0^k :

$$A_0^t = \sqrt{\frac{p}{2} \left(\frac{p}{2} - l_0^i\right) \left(\frac{p}{2} - l_0^j\right) \left(\frac{p}{2} - l_0^k\right)} \quad t = 1, \dots, N_t \quad (2.36)$$

with $p = l_0^i + l_0^j + l_0^k$. Finally,

$$\theta_0 = \arccos\left(\frac{\sqrt{3}(N_v - 2) - 5\pi}{\sqrt{3}(N_v - 2) - 3\pi}\right). \quad (2.37)$$

Parameter values and units

A compromise between the condition of Eq.(2.30) and computational cost settles on the choice $L_x = 30$ and $R = 15$. A channel is desired of diameter $D_{phys} = 10\mu\text{m}$, thus we fix the length unit as follows:

$$l_{phys} = \frac{D_{phys}}{2R} = \frac{10\mu\text{m}}{30} = 333\text{nm}. \quad (2.38)$$

On consequence, the RBC diameter $D_{0,DPD}$ results

$$D_{0,DPD} = \frac{D_0}{l_{phys}} = \frac{7.82\mu\text{m}}{333\text{nm}} = 23.5. \quad (2.39)$$

The polymer brush coating will have a width around $h_b \approx 3$. The energy scale is fixed by the temperature: $(k_B T)_{DPD} = 1$ both for the solvent and the cell, since the system is at thermal equilibrium. Thus:

$$e_{phys} = \frac{(k_B T)_{phys}}{(k_B T)_{DPD}} = 0.025 \times 10^{-19}\text{J} \quad (2.40)$$

Again, we fix the time scale such that the solvent viscosity matches the value for water at $T = 300\text{K}$ (see Eq.(2.18a)):

$$t_{phys} = \frac{\eta_{phys}}{\eta_{DPD}} \frac{l_{phys}^3}{3e_{phys}} = 5.5 \times 10^{-3}\text{s} \quad (2.41)$$

The above written choices lead to the following values for the parameters:

$$A_{0,DPD}^{tot} = A_{0,RBC}^{tot}/l_{phys}^2 = 1219 \quad (2.42)$$

$$V_{0,DPD}^{tot} = V_{0,RBC}^{tot}/l_{phys}^3 = 2551 \quad (2.43)$$

$$\mu_{0,DPD} = \mu_{0,RBC}l_{phys}^2/e_{phys} = 279 \quad (2.44)$$

$$k_{s,DPD} = k_s l_{phys}^2/e_{phys} = 135 \quad (2.45)$$

$$\gamma_{T,DPD} = \gamma_T \eta_{DPD}/\eta_{phys} = 9 \quad (2.46)$$

$$k_{b,DPD} = k_b/e_{phys} = 110 \quad (2.47)$$

RBC model parameter	DPD value
D_0	23.5
k_a	4900
k_d	100
k_v	5000
a_0	0.0518
a_1	2.0026
a_2	-4.491
A_0^{tot}	1219
V_0^{tot}	2551
A_0	1.22
x_0	1/2.05
μ_0	279
k_s	135
k_p	845
γ_T	9
γ_C	3
k_{BT}	1
k_b	110
θ_0	0.12

Table 2.1: Parameter values for a coarse-graining level $N_v = 500$ and physical scales defined according to Eqs.(2.38), (2.40) and (2.41). For the sake of conciseness, the subscript ‘‘DPD’’ has been omitted in the left column. The values indicated for l_0 , A_0 , k_p and l_m are averages.

As for the coarse-graining level, we choose $N_v = 500$, yielding on average:

$$l_0 = \sqrt{2A_0^{tot}/\sqrt{3}(N_v - 2)}/l_{phys} = 1.68, \quad (2.48)$$

$$l_m = l_0/x_0 = 3.44, \quad (2.49)$$

$$k_{p,DPD} = k_p/(e_{phys}l_{phys}) = 845, \quad (2.50)$$

$$A_{0,DPD} = A_{0,DPD}^{tot}/(2(Nv - 2)) = 1.22. \quad (2.51)$$

We provide the reader with the list in Tab.2.1 to summarize the parameter values.

We remark that, as a consequence of the chosen lengthscale, the value of l_0 , calculated in Eq.(2.48), is of order unit. It is important that the condition $l_0 \simeq r_c$ is fulfilled, otherwise the membrane would have too big stitches as compared to the interaction radius of solvent particles. Indeed, the membrane is not directly affected by collisions with solvent

particles, since momentum is not redistributed on triangle vertices. Thus the membrane can rearrange only as subdued to DPD interactions with solvents. In conclusion, if the membrane mesh is too large, a big amount of computational time is spent in operations (i.e., solvent collisions with membrane triangles) that do not produce any significant contribution to the observed cell dynamics.

Résumé (french version)

Un canal revêtu d'une brosse de polymères et contenant un liquide simple en écoulement représente un cas emblématique pour la mécanique des polymères hors équilibre. En plus, comme indiqué dans le chapitre précédent, il constitue un modèle minimal qui peut aider à clarifier certains aspects de la circulation sanguine. Un code numérique approprié doit comprendre les interactions hydrodynamiques, qui sont supposées jouer un rôle central pour la dynamique de la brosse, et en même temps il doit permettre une description détaillée des macromolécules de la brosse. Cette prémisse implique de couvrir une échelle de longueur allant du nanomètre jusqu'à des dizaines de micromètres. En conséquence, des simulations de Molecular Dynamics seraient trop coûteuses en temps de calcul et en capacité de mémoire; même avec les ordinateurs les plus performants, il serait impossible de reproduire les longues échelles de temps et de distance qui concernent l'hydrodynamique. D'autre part, il serait prématuré de construire un modèle en continuum pour résoudre les équations de Navier-Stokes sans avoir compris avant les propriétés des polymères qui ont un effet considérable sur le flux. Pour ces raisons, on a opté pour un point de vue intermédiaire et on utilise une technique coarse-grained de la Molecular Dynamics, qui s'appelle Dissipative Particle Dynamics.

La méthode Dissipative Particle Dynamics (DPD) emploie à la fois des moyennes spatio-temporelles pour les potentiels d'interaction ainsi que le regroupement des atomes dans une particule unique (la particule DPD). Elle a été introduite par Hoogerbrugge et Koelman en 1992 pour simuler les équations de Navier-Stokes en conditions isothermes. Ainsi, elle saisit les interactions hydrodynamiques et couvre des échelles de temps et de distance plus grandes que celles habituellement reproductibles avec la Molecular Dynamics. Selon cette méthode on doit résoudre l'équation de Newton pour chaque particule DPD, en considérant que la force agissant sur les paires de particules n'est pas obtenue par des potentiels moléculaires mais est calculée en conséquence du niveau de coarse-graining. Elle contient trois contributions: une partie conservative, une dissipative et une stochastique. Celles-ci sont toutes des forces centrales, en garantie de la conservation locale de la quantité de mouvement. En plus de ces forces de base, d'autres types d'interaction peuvent être inclus dans le cadre DPD, en fonction du système ciblé spécifique. Dans le cas présent, pour simuler les polymères, on ajoute des chaînes linéaires de particules DPD connectées par un potentiel élastique non linéaire à

extensibilité limité (FENE).

Notre code intègre les équations de Newton pour chaque particule DPD en utilisant l'algorithme aux différences finies qui s'appelle Velocity Verlet. Le système simulé est composé de N particules et est enfermé dans un canal à forme de parallélépipède et de côtés L_x, L_y, L_z . Une fraction N_m du nombre N total de particules est réservé aux monomères. Avec N_{ch} chaînes de polymères constituées par n (coarse-grained) monomères, on a $N_m = nN_{ch}$ (monomères d'ancrage non comptés). Pour réduire le temps de calcul on a attaché les polymères seulement dans la paroi de fond $z = 0$. Le long des axes x et y nous imposons des conditions aux limites périodiques, tant que à $z = 0$ et $z = L_z$ deux parois parallèles impénétrables de masse infinie sont posées, obtenant ainsi une géométrie *slit-pore*. Afin de produire un écoulement parabolique à l'intérieur du canal (par exemple, le long de la direction x) on applique une accélération constante $A = A\hat{x}$ sur toutes les particules du fluide.

Compte tenu de la souplesse du potentiel conservatif d'interaction, la répulsion DPD aux parois n'est pas suffisante pour éviter que les particules ne s'échappent du canal. Il est nécessaire de mettre en œuvre un mécanisme supplémentaire pour ramener les particules qui traversent la ligne des parois. Nous avons opté pour la méthode de la *bounce-back reflection*.

Avec notre choix pour les unités physiques le set-up simulé est proche du système physiologique ciblé (glycocalyx endothéliales dans les conditions de la micro-circulation).

Comme indiqué dans le chapitre précédent, l'interaction sous écoulement entre une brosse de polymères et un objet déformable n'a pas encore été élucidé. Nous ne sommes pas au courant d'études numériques précédentes portant sur ce problème. Il est légitime de se demander si la longue distance des interactions hydrodynamiques pourrait déclencher une réponse mécanique qui se propage d'une structure continue, comme l'interface d'une dense brosse de polymères, vers la surface déformable d'une cellule. Afin d'examiner cette question, nous avons exploité un modèle récemment publié de la membrane d'un globule rouge, un modèle coarse-grained qui peut être inclus dans un code DPD et donc couplé avec l'hydrodynamique et les polymères greffés.

La membrane est constituée d'un réseau de N points interagissants les uns avec les autres. Les forces tiennent compte de la visco-élasticité et de la flexibilité d'une membrane d'un globule rouge, dues à la double couche phospholipidique et à son cytosquelette de support. Puisque on

est intéressé surtout aux déformations du globule, il convient restaurer la symétrie axiale du système et commuter d'un canal *slit-pore* à un cylindre. Un nouveau choix plus approprié pour les unités physiques est opéré.

Chapter 3

Equilibrium properties of the brush

A full characterization of the polymer brush is achieved by calculating equilibrium properties. The comparison with well-settled theories and experiments provides a validation of our code.

3.1 A basic model for a polymer brush

Single free polymers have been extensively studied. Their widespread presence in nature together with the possibility to be synthesized in laboratories has made of them a favorite object of investigation concerning both fundamental and applied science. New materials like Teflon, PVC and plastic solar cells are just a few of the polymeric ingredients of modern industry [119], while protein folding and self-assembly properties of DNA are recent fields which biomedicine and nanotechnology has pointed a spotlight on [120–122]. Such a prolific amount of research has stemmed from a simple universal definition: a polymer is a macromolecule of repeated subunits (monomers). The theoretical counterpart in physics is a model of masses connected via springs. It is amazing how such a minimal model unifies the vision of the great variety of polymers. The reason for this success is in the very large polymerization degree n (i.e., the number of monomers per macromolecule): the statistics of configurations becomes dominant over the chemistry of bond type and scaling laws become the key in determining the polymer behavior.

As an example, let's consider one of the most representative quantities: the “end-to-end distance” R_{ee} , namely the typical length scale between the two extreme monomers. It gives a measure of the polymer average size. For a freely flexible chain of n subunits of size a , R_{ee} scales like the radius of gyration, R_g , defined as the root mean square distance between monomers:

$$R_g = \sqrt{\frac{1}{n} \sum_{k=1}^n (\vec{r}_k - \langle \vec{r} \rangle)^2}, \quad (3.1)$$

where \vec{r}_k is the k -th monomer position and $\langle \vec{r} \rangle$ is the center of mass of the chain. In good solvent conditions, the following relation holds:

$$R_{ee} \propto R_g \sim an^\nu \quad (3.2)$$

with ν called *Flory exponent*. The very first model, developed by Rouse, for the macromolecule equilibrium structure, considers the polymer as an *ideal chain*: subunits can occupy any position of space disregarding their neighbors [123]. In this case, monomers are distributed as subsequent positions of a random walk and the Flory exponent is $\nu = 1/2$. If the model takes into account excluded volume interactions, monomers have not all the space at their disposal, since they must avoid each others and their distribution follows a so-called *self-avoiding random walk* with the Flory exponent assuming the value $\nu = 3/5 \approx 0.588$. In case of a *polymer brush*, main object of the present thesis, the aforementioned relations do not hold anymore. A polymer brush is a three-dimensional matrix of grafted polymers. However, for a complete definition such statement is not sufficient: two different regimes should be distinguished, as sketched in Fig.3.1. As far as the distance d between grafting points is such that $d \gg R_g$, chains do not “feel” each other and similar statistical reasonings as before are valid to estimate R_{ee} . On the other hand, if $d \leq R_g$, polymer chains would significantly overlap so that, to avoid each other, they stretch along the direction perpendicular to the grafting substrate. A balance is reached between a maximal configurational entropy and a minimum cost in excluded volume interactions. This second regime of strongly stretched chains actually defines the polymer brush condition and it is responsible of completely novel features for the system, the physics assumes new characteristics and scalings have to be recasted on new meaningful quantities. It is now convenient to introduce the grafting density σ_{graft} , being $d = (\sigma_{graft})^{-1/2}$.

Polymer brushes are versatile media. There exists a host of different

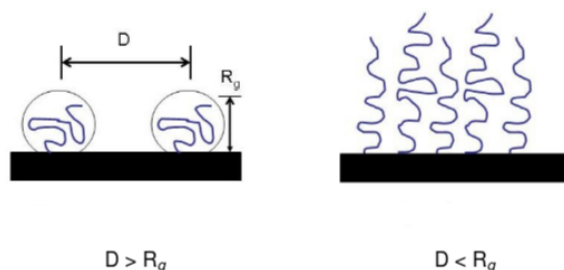


Figure 3.1: The two possible regimes for grafted polymers, depending on the relation between the radius of gyration R_g and the distance d between anchor points: (a) if $R_g < d$ the *polymer mushroom* regime takes place in which macromolecules do not interact directly with each another; (b) if $R_g \geq d$ the excluded volume interaction among polymers forces them to strongly stretch: such condition defines the *polymer brush* state.

kinds of brushes: mixed brushes, in case different polymers are grafted on the same surface (Fig.3.2(a)); block copolymers, in case different kinds of monomers are polymerized onto the same linear chain (Fig.3.2(b)); the polymerization process can be manipulate in order to fix functional groups at the chain free ends to tune different responsivenesses at different stimuli (Fig.3.2(b)). Geometry can play a role if the grafting substrate is flat or spherical (Fig.3.2(c)); the substrate itself can be a solid surface but also an interface between two liquids; moreover, the choice of certain polymers will determine the solvent affinity (Fig.3.2(d)). In conclusion, due to the possibility to design them with the desired features, polymer brushes can be used to tailor physico-chemical properties of any surface. Applications are numerous: they are exploited for colloid stabilization [1–3], as lubricant layers [4–6], as adhesion regulators [7, 8] and for biomedical and technological applications, especially motivated by the discovery that the inner surface of various mammalian organs is decorated by densely grafted macromolecules. Indeed, the endothelial glycocalyx we have introduced in Chap.1 is only one example: similar coatings shield also the mammalian uterus, small intestine and lungs.

Polymer brushes in solvent at equilibrium have been thoroughly investigated in the past [15, 16, 21, 124]. Theoretical predictions and experimental results can be used to test the proposed model, as we are going to check in this Chapter.

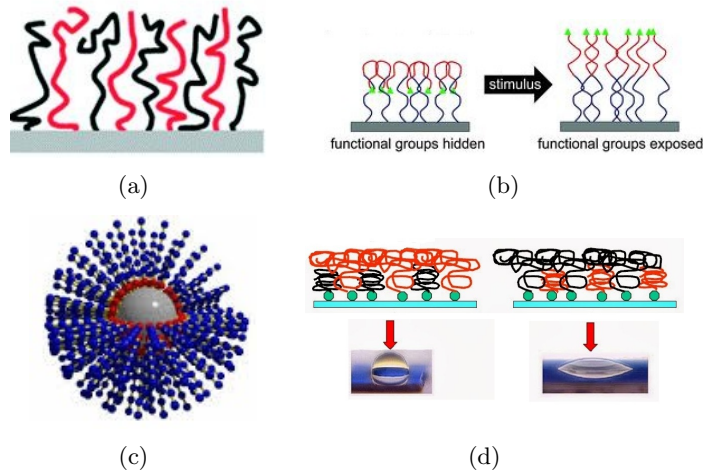


Figure 3.2: Examples of polymer brush architectures: (a) mixed brush, made of different kind of grafted polymers; (b) block copolymer brush, constituted by interchanged blocks of different kind of monomers/polymers in the same linear chain; (c) brush on a spherical substrate; (d) brushes with different solvent affinity.

3.2 Density profiles and scalings

At equilibrium, brush conformation results from the balance between configurational entropy, that tends to make chains visit the whole available space, and excluded volume interactions, which disfavors contact between monomers. The brush is properly described by means of the profile $\rho(z)$, indicating the probability distributions of finding a monomer at distance z from the grafting wall. In Fig. 3.3(a) we show $\rho(z)$ at $\sigma_{graft} = 1.5$ for several degrees of polymerization ($n = 20, 25, 30, 36, 40, 45$). Figure 3.3(b) shows the same quantity at $n = 40$ varying the grafting density ($\sigma_{graft} = 0.1, 0.3, 0.5, 0.8, 1.0, 1.5$). In line with previous theoretical results [16] and numerical studies [124,125], the higher the volume fraction, the more step-like the density profile is.

A definition of the brush height h_b in term of the first moment $\langle z \rangle$ of the probability profile depends on the shape of $\rho(z)$. Assuming that all chains are equally elongated so that free ends are all at the maximum distance from the grafting wall, the profile $\rho(z)$ is step-like (*Alexander model* [93, 94, 126]) and the brush height can be defined as $h_b = 2\langle z \rangle$. A less rigid theory (strong stretching limit of the *self-consistent mean*

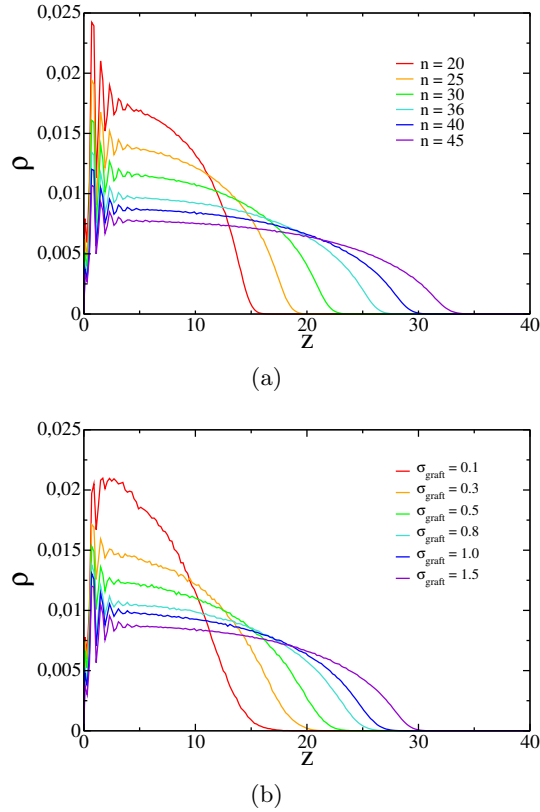
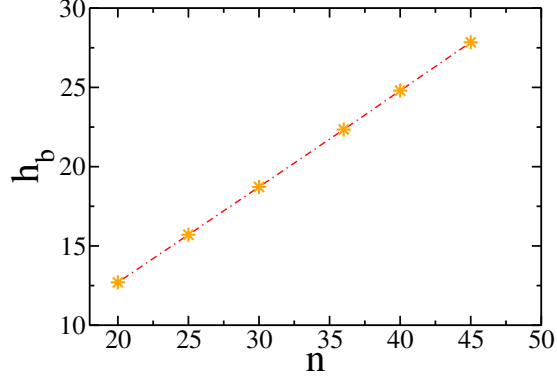


Figure 3.3: Probability distributions of polymer brushes at equilibrium: (a) fixed the grafting density, $\sigma_{graft} = 0.5$, the degree of polymerization n is varied; (b) fixed the degree of polymerization, $n = 40$, the grafting density σ_{graft} is varied. Oscillations near $z = 0$ indicate an ordering: obliged to keep a fix distance from the anchor points, monomers close to the wall constitute an almost layered structure. The qualitative behavior is similar in both cases, thus the higher the volume fraction, the more step-like the probability distribution.

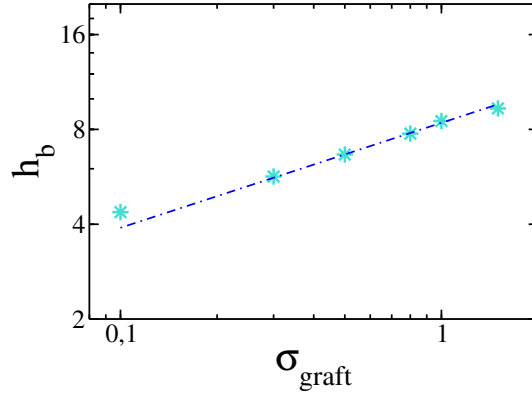
field theory [15, 16]) hypothesizes that monomers of a same chain are distributed as a random walk, therefore the free end position ranges uniformly over the whole brush thickness. In such a case the profile is parabolic, $\rho(z) = \rho(0)(1 - z^2/h_b^2)$, and the brush height is $h_b = \frac{8}{3}\langle z \rangle$. Our simulation results in Fig.3.3 entail a difference with respect to both theories: at the brush periphery, the profile does not drop to zero as a parabola or a step-like function would do: it rather decays smoothly. This is the effect of fluctuations in the distribution of chain ends as compared with the aforementioned theoretical hypotheses. Anyway, we follow the

assumption of a step-like distribution and define h_b as

$$h_b = 2 \frac{\int_0^\infty z \rho(z) dz}{\int_0^\infty \rho(z) dz} \quad (3.3)$$



(a)



(b)

Figure 3.4: Our brush model is perfectly conform to the mentioned scaling laws supported by theory: (a) it fits the linear behavior as function of the chain length n ($\sigma_{graft} = 1.5$) and (b) the power law behavior with power $1/3$ as function of the grafting density σ_{graft} ($n = 40$). To be noticed in (b) the only one point out of the scaling fit: it corresponds to the lowest value of σ_{graft} and it indicates that under such condition polymers are far from the *brush* regime and rather match the *mushroom* regime.

As declared in the previous Chapter, we consider the case of a hydrophilic brush (*good solvent* condition). Surprisingly, the same scaling for h_b is extracted both from the Alexander and from the self-consistent

mean field theories:

$$h_b \sim n\sigma_{graft}^{1/3} \quad \text{under “good solvent” condition.} \quad (3.4)$$

Figure 3.4 shows that Eq.(3.4) is perfectly verified by our data both regarding the linear dependence on n , as well as the $1/3$ power dependence on σ_{graft} .

We report in Fig.3.5 the density profile for the solvent, compared with the brush density: the brush is completely wet, since solvent density inside it does never decay to zero, not even at the grafting wall. We recall that the overall numerical density ρ is fixed to $\rho = 3$ in our DPD simulations.

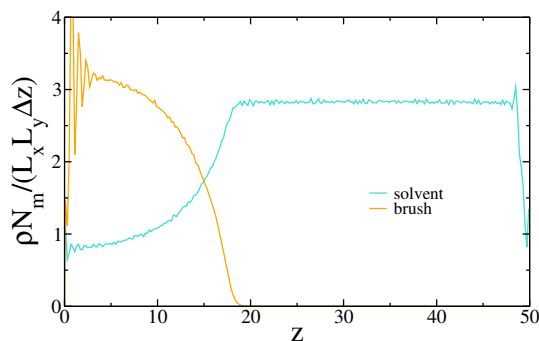


Figure 3.5: Comparison between the solvent and the brush density profiles. With the normalization $N_m/(L_x L_y \Delta z)$, where Δz is the mesh size along z , the ordinate axis actually reports the number of monomers per unit volume. Solvent density is different from zero everywhere, even inside the brush and at the grafting wall, meaning that the brush is wet as it should be the case in *good solvent* conditions. Plots have been realized for $n = 25$.

3.2.1 The longest relaxation time

A characterization of the brush relaxation time is meaningful as only external forces that act on shorter timescales are able to perturb the brush dynamics. To clarify such statement, we resort to the same schematic view as for the Born-Oppenheimer approximation, with the difference that here we will define the opposite limit case. The Born-Oppenheimer approximation is used to break the molecular Schrödinger equation into a nuclear component and an electronic component. Since the nucleus of an atom is extremely massive with respect to electrons, at thermal equilib-

rium it will move at extremely lower velocity: for the electron dynamics the nucleus can be considered to be at a fixed position and, therefore, the two components of the molecular system can be decoupled. Here, the brush is our “electronic cloud” and since we are interested in the out-of-equilibrium brush dynamics, we will focus on the opposite case with respect to the Born-Oppenheimer approximation: the case in which the external force cannot be decoupled and (differently from the nuclear contribution to electron dynamics) expresses on shorter timescales than the brush relaxation one. For this reason, we choose to estimate the longest brush timescale t_{brush} , associated with the adjustment of the whole chain configuration [123]: any force acting on shorter timescale is able to induce interesting dynamics of the brush. To monitor the relaxation of the whole chain configuration we evaluate the decay of the autocorrelation function (ACF), averaged over all distinct polymers, of the end-to-end vector amplitude R_{ee} :

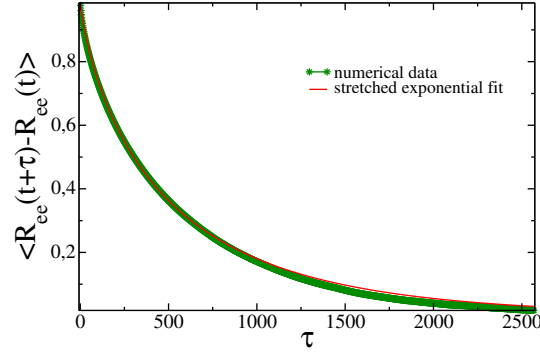
$$ACF[R_{ee}](\tau) = \frac{\langle (R_{ee}(t + \tau) - \langle R_{ee} \rangle)(R_{ee}(t) - \langle R_{ee} \rangle) \rangle}{\langle R_{ee}(t)^2 \rangle - \langle R_{ee} \rangle^2} \quad (3.5)$$

where $R_{ee} = |\vec{r}_0 - \vec{r}_n|$ and \vec{r}_n and \vec{r}_0 are the position vectors of, respectively, the last particle and the anchor of the chain. We have normalized the ACF by the variance. We then identify the timescale t_{brush} as the average time of this decay process:

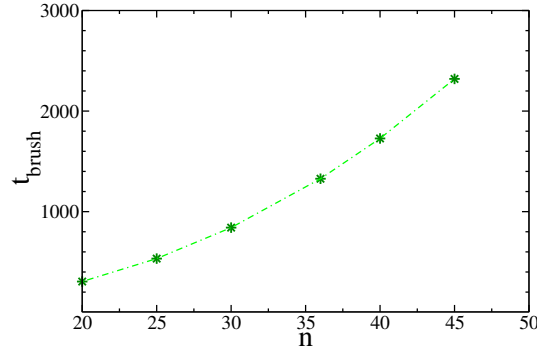
$$t_{brush} = \frac{\int t ACF[R_{ee}](t) dt}{\int ACF[R_{ee}](t) dt}. \quad (3.6)$$

We highlight that, since the ACF function is averaged over all distinct polymers, the relaxation time t_{brush} assumes a dependency on the grafting density and on the degree of polymerization, thus representing a time scale of the whole brush rather than an isolated single-chain property. The decay of the auto-correlation function $ACF[R_{ee}](\tau)$ is well fitted by a stretched exponential $ACF[R_{ee}](\tau) \sim e^{-(\tau/t_o)^\beta}$, where t_o is the characteristic time scale and β , $0 < \beta < 1$, the so-called *stretching exponent* (see Fig.3.6(a)). From the definition in Eq.(3.6), t_{brush} is thus evaluated as $t_{brush} = \Gamma[\frac{1}{\beta}]t_o$. The standard exponential function is recovered for $\beta = 1$ (and in such case the average would simply be $t_{brush} = t_o$). This deviation from the usual exponential decay is commonly associated with heterogeneities in the system and for a free polymer in solution a simple exponential decay is expected. Thus, we ascribe the heterogeneity to the brush structure in the transversal direction with respect to the graft-

ing surface: relaxation cannot be uniform along the single chain, since monomers close to the anchor point experience a stronger excluded volume interaction than monomers at the free end. We report in Fig.3.6(b) t_{brush} as function of n . Despite the chain non-ideality and the presence of the neighbor polymers forming the brush, the curve is quadratic in n , i.e. the same dependence predicted by the Rouse model for free single polymers as ideal chains [123].



(a)



(b)

Figure 3.6: Estimation of the brush longest relaxation time in case $n = 25$ and $\sigma_{graft} = 1.5$: (a) the decay of the end-to-end autocorrelation function (green stars) is suitably fitted by a stretched exponential $R_{ee}(\tau) = e^{-(\tau/t_o)^\beta}$, with $\beta = 0.79$ and $t_o = 479$ (red curve); (b) the relaxation time $t_{brush} = \Gamma[1/\beta]t_o$ is quadratic as function of the chain length n (blue fit, $t_{brush} = A + Bn + Cn^2$ with $A = 344$, $B = -38.2$ and $C = 1.82$).

3.2.2 Chain stiffness

With the model discussed in Sect.2.2.1, our simulated chains are freely flexible. Excluded volume interaction aside, neighboring monomers have no constraints on the reciprocal orientation. Indeed, we have not included in the model any three-body force that takes into account chain bending rigidity. Nevertheless, the coarse-graining applied on polymers transforms the atomic monomers in *blobs* and on the scale defined by the blob size a certain stiffness is intrinsic. Considering physical scales, if the blob has a longer linear size than the persistence length of the real polymer, then the mutual orientation of subsequent coarse-grained monomers along the chain is uncorrelated and neglecting any stiffness is justified. With the physical units reported in Sect.2.3, this turns to be the case of our simulations. Actually, in the DPD approach, particles are assumed to be point-like and no degrees of freedom are taken into consideration for the particle rotation. However, it is reasonable to associate a size to DPD particles from their equilibrium distribution in space: we estimate the DPD blob size ℓ as the average equilibrium distance between neighbor particles of a same chain. Our simulations yield $\ell = 0.90$, in agreement with the theoretical value $\ell = 0.897$ found by the minimization principle $\partial V/\partial r|_{r=\ell} = 0$, where V is the sum of the DPD conservative potential (Eq.(2.3)) and the FENE potential (Eq.(2.9)): $V(r) = -a_{PP} \left(r - r^2/(2r_c) - r_c/2 \right) - kR^2 \log(1 - (r - r_{eq})^2/R^2)$. Here we have used $r = r_{ij}$. The minimization results in a 3rd degree polynomial equation:

$$\begin{aligned} \frac{a_{PP}}{r_c} \ell^3 - \left(a_{PP} + 2 \frac{r_{eq}}{r_c} a_{PP} \right) \ell^2 - \left(\frac{R^2}{r_c} a_{PP} - 2r_{eq} a_{PP} - \frac{r_{eq}^2}{r_c} a_{PP} + 2kR^2 \right) \ell \\ + (R^2 - r_{eq}^2) a_{PP} + 2kR^2 r_{eq} = 0 \end{aligned} \quad (3.7)$$

that can be numerically solved and has one single root for $0 < \ell < 1$. Reporting to physical units, we obtain $l_{pers} = \ell \cdot l_{phys} = 0.9 \cdot 24 \text{nm} \sim 22 \text{nm}$, that is the order of magnitude of typical polymeric persistence lengths (DNA, that is one of the stiffest polymers, has a persistence length around 35nm [127]).

A second source of stiffness can be induced by the FENE potential. In case the distance between neighbors exceeds a certain value starting from which the FENE potential deviates from the elastic regime, non-linearity enters the dynamics and chains stiffen. In Fig.3.7 we report the curve for the effective potential $V = V^C + V_{FENE}$ acting between

neighbor monomers. We also include a plot for $\bar{V} = V^C + V_{harm}$, where

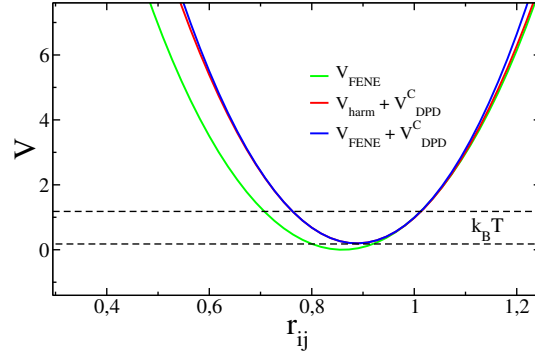


Figure 3.7: Plots corresponding to potential curves: (orange) the FENE potential, (blue) the effective potential between monomers including also the DPD conservative contribution and (magenta) its harmonic counterpart, where V_{FENE} has been replaced by a purely quadratic potential (see the main text for the analytical expressions). Parameter values are listed in Sect.2.3.

$V_{harm} = -k(r - r_{eq})^2$ is the purely elastic potential matching V_{FENE} in the limit of small displacement $r - r_{eq} \ll 1$. Comparing the two plots, it is clear that fluctuations around the equilibrium distance ℓ induced by the non-zero temperature do not push monomers in the nonlinear region of the potential V and differences with respect to the harmonic \bar{V} are not experienced at equilibrium. Therefore, chains act as spring of constant elasticity.

3.3 Polydisperse brush

Polymer brush polydispersity refers to the presence of chains with different molecular weight n . A generic polymer brush has inevitably a degree of polydispersity: a biological example, as the endothelial glycocalyx, reveals itself as highly polydisperse (see Fig.1.2(b)), but even for an experimentally built-up brush is impossible, in practice, to be perfectly monodisperse. The effect of polydispersity on equilibrium brush has been investigated theoretically [128], numerically [129, 130] and by mean of experiments [18, 130]. In this thesis, too, we will not ignore such feature. Here in the present Section we characterize a polydisperse and more realistic brush and compare it to the homodisperse case.

3.3.1 Bimodal distribution

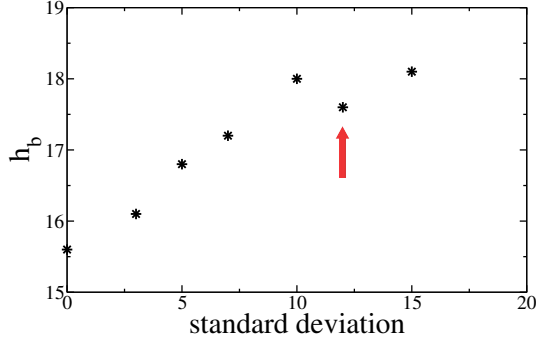


Figure 3.8: The brush height h_b , $h_b = 2 \int_0^\infty z\rho(z)dz / (\int_0^\infty \rho(z)dz)$, as function of the standard deviation of n for a polydisperse brush whose chain lengths follows a Gaussian distribution with fixed average $\langle n \rangle = 25$. The trend is not monotonous, as highlighted by the red arrow.

The first issue to tackle is the choice of an appropriate distribution for the chain lengths n , given that our simulated brush has size limitations and n is restricted to only integer values. Retaining the same $\langle n \rangle$, as a result of an increasing polydispersity, the brush thickness is expected to grow [129], but we show in Fig.3.8 that, for example, with a Gaussian distribution of chain lengths h_b has not a monotonous trend as function of the imposed standard deviation of n , namely of polydispersity. To avoid such artifacts, we opt for a bidisperse brush, that is precisely tunable and not far from experimental cases [18].

A bidisperse brush is characterized by two different chain lengths, n_- and n_+ , and by a mixing ratio indicating the proportion between the two fractions. Following the approach of Ref. [129] we produce different bidisperse brushes by changing n_- and n_+ while maintaining the average chain length $\langle n \rangle$ and overall grafting density σ_{graft} constant. With such choice any particular deviation from the known features can be attributed only to polydispersity itself. We also fix the mixing ratio to (1:1), thus simply $\langle n \rangle = (n_- + n_+)/2$. In Fig.3.9(a) we report the density profiles for $\langle n \rangle = 25$ and $\sigma_{graft} = 1.5$. The polydispersity index PI is calculated as the ratio of the weight average molar mass M_w over the number average mass M_n :

$$PI = \frac{M_w}{M_n} = \frac{\sum_i N_i n_i^2}{\sum_i N_i n_i} \frac{\sum_i N_i}{\sum_i N_i n_i} \quad (3.8)$$

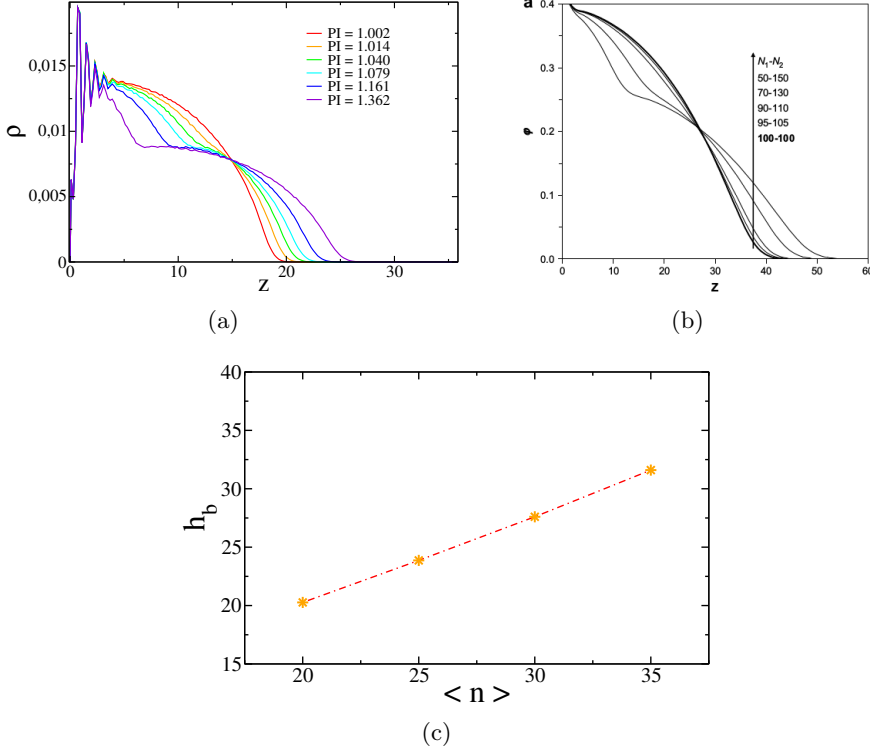


Figure 3.9: Panel (a) shows the density profiles for a bidisperse brush characterized by $\langle n \rangle = 25$ and $\sigma_{graft} = 1.5$. As the polydispersity index grows, the profile assumes a dichotomous trend, indication that the shortest chains are increasingly compressed while the longest ones are more elongated. Panel (b) is extracted from Ref. [129] and compare well with panel (a) (ϕ is the monomer density and N_1 and N_2 correspond to n_- and n_+ in our notation). Panel (c) reports the scaling of the brush height as function of $\langle n \rangle$: as for the homodisperse case, the curve is linear.

where N_i is the number of chains and n_i is the number of monomers per chain. For our bidisperse brush $i = +, -$. The broader is the degree of polymerization range, the larger the PI index; the homodisperse case corresponds to $PI = 1$. For the cases in Fig.3.9(a) we obtain: $PI = 1.002$ for $(n_- = 24, n_+ = 26)$, $PI = 1.014$ for $(n_- = 22, n_+ = 28)$, $PI = 1.040$ for $(n_- = 20, n_+ = 30)$, $PI = 1.079$ for $(n_- = 18, n_+ = 32)$, $PI = 1.161$ for $(n_- = 15, n_+ = 35)$ and $PI = 1.362$ for $(n_- = 10, n_+ = 40)$. With their superimposed parabolas, one on top of the other, the profiles are in perfect agreement with theoretical ones found by numerical solutions of the self-consistent mean field theory [129]. Figure

3.9(b) is reported from Ref. [129] to offer a plain comparison with our data. We can conclude, together with authors of Ref. [129], that in our system, too, the bidispersity induces a segregation of chain ends: while in a monodisperse brush the chain end distribution grows almost linearly with the distance from the grafting surface and then drops to zero at the brush periphery, for a bidisperse brush the chain end distribution has two different peaks, one related to the shortest chains and the other one related to the longest. As the chain length difference between the two fractions increases, the distance between the two peaks increases, meaning that an end-depleted region creates. Such a *segregation effect* indicates that in a bidisperse brush, for the single chain, fluctuations of the free end are strongly suppressed.

On changing $\langle n \rangle$, we check the scaling of the brush height h_b , keeping the same grafting density $\sigma_{graft} = 1.5$ and mixing ratio (1:1) as above. Since profiles resemble superimposed parabolas, it is more appropriate in this case the use of the definition $h_b = \frac{8}{3}\langle z \rangle$, as discussed in Sect.3.2. The plot in Fig.3.9(c) proves that also our DPD numerical simulations, regardless of bidispersity, yield $h_b \sim \langle n \rangle$, as for the homodisperse case. This is also in agreement with numerical solutions of the self-consistent mean field theory according to which such scaling is independent of polydispersity [129].

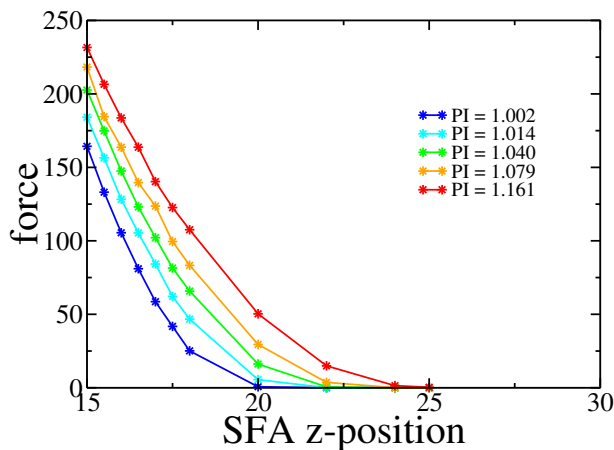


Figure 3.10: Results from simulations of a Surface Force Apparatus measurement (see the main text) for bidisperse brushes with $\langle n \rangle = 25$ and different degrees of polydispersity. The higher is the polydispersity index, the thicker the layer and the easier to compress the brush.

As a last consideration, we simulate a Surface Force Apparatus (SFA) measurement to probe the compressibility of the bidisperse matrix. Those kind of experiments are usually exploited to estimate the brush height: a cantilevered plate is moved closer and closer to the brush interface while measuring the strength of the interaction between the probing tip and the brush. The distance at which the recorded force starts increasing from zero accounts for a good estimation of the brush thickness. In our simulations the brush is compressed by an ideal surface that behaves as a solid wall for monomers but it is completely permeable to solvent particles. As can be inferred by the results reported in Fig.3.10, a bidisperse brush (with $\langle n \rangle = 25$ in the example) does constitute a thicker layer the more and more the polydispersity index is increased. Indeed, forces recorded by the simulated Surface Apparatus depart significantly from zero at bigger and bigger distances from the grafting substrate. At the same time, the increase of polydispersity is accompanied by a decrease in the slope of the force vs. SFA-position curve. In conclusion, at equilibrium the bidisperse brush is thicker but also softer than the equivalent homodisperse one (i.e., with $n = \langle n \rangle$).

Résumé (french version)

On obtient une caractérisation complète de la brosse de polymères en calculant les propriétés d'équilibre. La comparaison de nos résultats avec des théories et des expériences bien établies porte à une validation de notre code. En effet, les brosses de polymères dans un solvant à l'équilibre ont été examinées en profondeur dans le passé, donc on a à disposition des prédictions théoriques pour tester le modèle proposé.

A l'équilibre, la conformation des polymères de la brosse résulte d'un bilan entre l'entropie configurationnelle, qui fait visiter aux chaînes tout l'espace disponible, et les interactions de volume exclu, qui défavorisent le contact entre monomères. Ainsi, la brosse est correctement décrite par le profil $\rho(z)$, indiquant la distribution de probabilité de trouver un monomère à la distance z de la paroi de greffage. Pour la hauteur de la brosse on trouve les mêmes scalings indiqués par le modèle d'Alexander et par la théorie du champ moyen auto-cohérent.

On procède à estimer le temps caractéristique le plus long, associée à la relaxation de la configuration de la chaîne entière, puisque toutes les forces agissantes dans un délais plus court sont capables d'induire une dynamique intéressante de la brosse. Pour calculer le temps de relaxation on évalue la décroissance de la fonction d'autocorrélation, calculée via une moyenne sur tous les polymères de l'amplitude du vecteur end-to-end. On identifie alors ce temps caractéristique avec le temps moyen de ce processus de décroissance. Malgré la non-idéalité des chaînes et la présence des polymères voisins formant la brosse, la courbe est quadratique avec n , c'est-à-dire la même dépendance prédite par le modèle de Rouse pour le single polymère libre visé comme chaîne idéale.

On examine également les propriétés d'équilibre d'une brosse polydispersée. La polydispersité d'une brosse de polymères se réfère à la présence de chaînes de poids moléculaire n différent. Une brosse de polymères générique a inévitablement un degré de polydispersité: un exemple biologique, comme le glycolyx, se révèle très polydispersé, mais même pour une brosse construite expérimentalement est impossible, en pratique, d'être parfaitement monodispersée. L'effet de la polydispersité sur la brosse à l'équilibre a été étudié théoriquement [128], numériquement [129, 130] et expérimentalement [18, 130]. Ici, on opte pour une brosse bidispersée, exemple qui est précisément ajustable et pas loin des cas expérimentaux [18]. Avec leurs paraboles superposées, une au-dessus de l'autre, les profils de densité des monomères sont en parfait accord avec ceux-là théoriques trouvés en résolvant numériquement

la théorie du champ moyen auto-cohérent [129]. On conclut, avec les auteurs de la Réf. [129], que dans un tel système la bidispersité induit une ségrégation des extrémités des chaînes: dans une brosse monodispersée la distribution des extrémités des chaînes croît presque linéairement avec la distance de la surface de greffage, puis tombe à zéro à la périphérie de la brosse; pour une brosse bidispersée cette distribution a deux pics bien séparés, l'un concernant les chaînes les plus courtes et l'autre concernant les plus longues. Comme la différence de longueur entre les deux fractions des chaînes augmente, la distance entre les deux pics augmente, ce qui signifie qu'une région appauvrie d'extrémités va se créer. Un tel effet de ségrégation indique que dans une brosse bidispersée, pour la chaîne simple, les fluctuations de l'extrémité libre sont fortement supprimées.

Enfin, on simule un appareil à force de surface (*Surface Force Apparatus*) pour sonder la compressibilité de la matrice bidispersée. On trouve que à l'équilibre la brosse bidispersée est plus épaisse mais aussi plus souple que l'équivalente monodispersée.

Chapter 4

Polymer brushes under flow

A dense polymer brush subdued to a simple liquid parabolic flow in a slit-pore geometry is investigated. The chosen numerical method allows for a quantitative description of the single chain behavior as well as for the analysis of the flow streamlines. The known effect of flow reversal at the brush-solvent interface is identified and characterized. A novel explication is proposed that integrates previous literature and attributes the phenomenon to polymer collective dynamics, precisely to the onset of a wave traveling over the brush surface.

While the equilibrium properties of a polymer brush have been sealed by the vast literature on the subject, there is lack of data and equivalent consensus for the case of polymer brushes subdued to flow. Most theoretical studies have attempted to model polymer brushes as porous media described by Brinkman-type equations [131] or as a dense collection of very rigid fibers [83]. Those approaches do not include recent results on polymer brushes under flow. As already mentioned in Chap.1, according to such recent studies an unexpected behavior of the velocity profile in the vicinity of the brush surface is highlighted [86, 91, 92]: the velocity field reverses on increasing the flow strength. Aiming at investigating deeply the reasons for such peculiar phenomenology, we undertake a DPD numerical investigation exploring a very large range of imposed flows. As presented in this Chapter, we discover (i) that flow inversion appears in distinct regions of imposed flow values; (ii) that every time flow inversion is observed a surface wave appears, demonstrating that the backflow is strongly associated to a collective (as opposed to single) polymer dynamics; (iii) that the wave properties are consistent with predictions derived by Taylor in his seminal study on microswimmers [132]. Thus, our work

presents a new interpretation for the flow inversion phenomenon and establishes a link between two distinct fields: polymer brushes under flow and microswimmers.

Instead of using the imposed acceleration A as a measure of the flow intensity, we introduce a dimensionless quantity: the Weissenberg number. The Weissenberg number Wi is defined as the ratio $Wi := t_{brush}/t_{flow}$, where t_{brush} is a characteristic structural time of the unperturbed brush and t_{flow} provides an estimate of the typical time scale associated to the flow. Following previous literature [133], we evaluate t_{brush} as the longest polymer relaxation time, calculated in Sect.3.2.1 from the decay of the autocorrelation function of the end-to-end vector amplitude R_{ee} . Regarding t_{flow} , we choose the inverse of the averaged shear rate, $t_{flow} = (\bar{\dot{\gamma}})^{-1}$, where $\bar{\dot{\gamma}}$ is calculated as the ratio between the maximum flow velocity v_{max} in the channel and the corresponding z-coordinate R . Since our brush under flow experiences compression (see Fig. 4.3) and polymers are set only at the bottom wall, both v_{max} and R depend on the imposed acceleration A .

From now on we fix $\sigma_{graft} = 1.5$, determining a distance between grafting points equal to $d = \sqrt{1/\sigma_{graft}} \approx 0.82$. This choice is motivated by analogy with the reference system we aim to investigate: indeed, as discussed in Sect.1.2.1, endothelial glycocalyx is characterized by a high grafting density, with d in the same order of magnitude as the distance ℓ between monomers of a same chain. In our system, a density $\sigma_{graft} = 1.5$ corresponds to $N_{ch} = 225$ chains grafted on the bottom wall. Since a crucial part of the presented analysis has focused on a brush with $\sigma_{graft} = 1.5$ and $n = 40$ for which $t_{brush} = 1746$, we offer in table Tab. 4.1 a list of the correspondences between each value of A and its Wi for such specific case.

4.1 Single polymer dynamics

For single free polymers the conformation at equilibrium and under mechanical stress has been elucidated [93, 123, 134]. In particular, the behavior under shear flow has received significant attention [133, 135]. This last topic is of interest also for the present thesis. It has been shown that, subdued to shear, free polymers perform an aperiodic tumbling, due to the interplay between Gaussian thermal fluctuations of the chain configuration and to the anisotropy introduced by the shear [136–138]. Not a complete flip but a recursive motion is displayed in case the single polymer

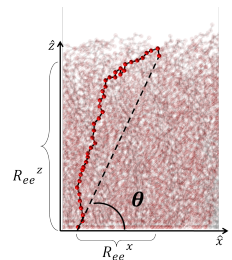
Conversion $A \leftrightarrow Wi$

A	Wi	A	Wi	A	Wi	A	Wi
0.005	45	0.022	208	0.047	409	0.064	612
0.007	64	0.023	218	0.048	413	0.065	616
0.01	91	0.028	275	0.05	418	0.066	627
0.015	137	0.03	297	0.051	420	0.067	642
0.016	147	0.034	340	0.055	430	0.07	737
0.017	158	0.037	375	0.0565	588	0.075	788
0.018	167	0.04	400	0.575	593	0.08	832
0.019	175	0.043	405	0.058	595	0.1	1044
0.02	187	0.045	406.7	0.06	599	0.15	1413
0.021	200	0.046	407.4	0.063	607	0.2	1631

Table 4.1: Tables of conversions between the constant acceleration A , imposed on each solvent particle to obtain a parabolic velocity profile, and the estimated dimensionless Weissenberg number Wi for the case of a polymer brush with $\sigma_{graft} = 1.5$ and $n = 40$.

is grafted on a substrate [139,140]. In both cases, the explanation resides in the presence of thermal fluctuations and in the intrinsic structure of a planar flow, that can be thought as a superposition of a pure rotation and a pure elongation [141]. However, things get rapidly more complicated in case polymers are *densely* grafted: the brush interior is screened to hydrodynamic interactions, while the surface is exposed to flow and, as we endeavor to elucidate in this thesis, it can drive a polymer collective motion. An explanation for such dynamics should take into account the crucial role of the hydrodynamics interplay with brush entropic and osmotic forces. However, before focusing on collective effects, we portray the single polymer averaged dynamics.

Under flow, chains tilt. As in the sketch below, we identify the tilting angle with θ , defined as the angle between \hat{x} (the flow direction) and $\vec{R}_{ee} \equiv (R_{ee}^x, R_{ee}^y, R_{ee}^z)$. Its evaluation reads:



$$\theta = \arccos \left\langle \frac{R_{ee}^x}{R_{ee}^{xz}} \right\rangle \quad (4.1)$$

where $R_{ee,xz}$ is the modulus of the \vec{R}_{ee} projection on the xz plane ($R_{ee}^{xz} = \sqrt{(R_{ee}^x)^2 + (R_{ee}^z)^2}$). The average $\langle \dots \rangle$ is both over time and over all chains. A smaller value of θ corresponds to a larger inclination. The tilting as function of Wi is plotted for different n in Fig.4.1(a). We notice that tilting is detectable as soon as Wi is non-zero. In addition to the average value, we visualize the distribution $f_n(\theta)$ of tilting angles itself: of course its mean moves to smaller values as function of Wi , but it gets also more asymmetric. We report such distributions in Fig.4.1(b) for $n = 40$. At $Wi = 1413$ the distribution $f_{40}(\theta)$ is narrower, as expected for really high flow. A precise quantification of the asymmetry is given in Fig.4.1(c) by the skewness a of $f_{40}(\theta)$:

$$a = \frac{\int f_{40}(\theta)(\theta - \langle \theta \rangle)^3 d\theta}{(\int f_{40}(\theta)(\theta - \langle \theta \rangle)^2)^{(3/2)}}. \quad (4.2)$$

The relative elongation, defined as the average end-to-end distance R_{ee} relative to the equilibrium value, is plotted in Fig.4.2 for several n : it increases as the flow gets higher. The tilting contributes with a stronger effect if, despite such elongation, the flow increase results in a compression of the brush, as reported in Fig.4.3. We note that while tilting is detectable as soon as the flow is switched on, elongation and compression change significantly only for $Wi > 100$. We stress our finding of a decrease of the brush height as function of Wi . Actually, it adds a result to the still open, longstanding debate about whether a polymer brush swells or compresses as subdued to flow: the literature contains contrasting analyses according to which the layer should thicken [21], or rather thin [22], or even keep constant [23]. From our simulations, we conclude that at low shear flow the brush height is not affected, while at high shear flow it thins. No swelling effects are detected and, as far as we know, no numerical simulations have ever documented it and the experimental data reporting on it did not display direct measurements, they rather pertained trends of mechanical quantities (increase of normal forces) that have been interpreted as a brush height increase [24]. We relate the brush thinning to chain stiffening under flow and we attribute such stiffening to a purely entropic effect (rather than to FENE nonlinearity). Indeed, we can exclude a FENE contribution by calculating the root mean square (rms) of the distance between neighbor monomers, as reported in Fig.4.4(a). At really high flow ($Wi = 1631$) such rms for the outer monomers reaches a value $rms \approx 0.15$, that is bigger than the equi-

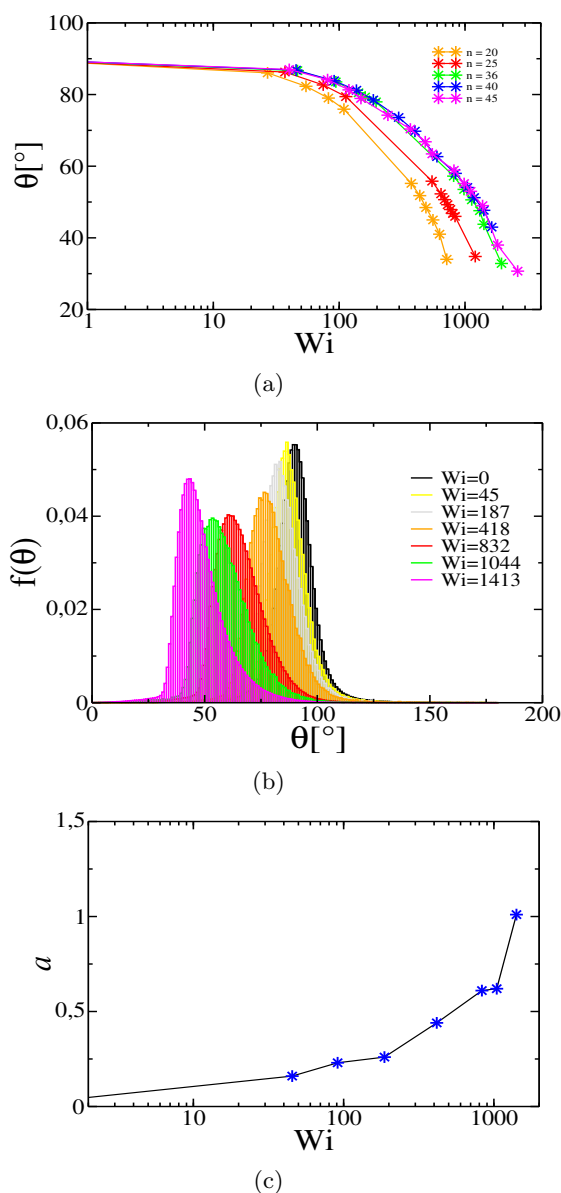


Figure 4.1: Characterization of chain average tilting: (a) measure of the tilting angle, sketched in the inset, as function of Wi for different chain lengths n ; (b) tilting angle distribution at different Wi for $n = 40$; (c) the skewness of the tilting angle distribution $a = \int f_{40}(\theta)(\theta - \langle \theta \rangle)^3 d\theta / (\langle \theta^2 \rangle - \langle \theta \rangle^2)^{3/2}$.

librium one ($rms = 0.1$ induced by thermal fluctuations), nevertheless monomers still experience a linear elasticity: recalling Fig.3.7, a displace-

ment Δr of an amount $\Delta r = rms \approx 0.15$ with respect to the equilibrium distance $\ell = 0.90$ still falls in the region of equivalence between the FENE and its linear version potential. Thus, it is basically the elongation and ordering of chains that break down the static equilibrium balance between entropy and excluded volume interaction enhancing the first one and contributing to the decrease of h_b . We complete the description on the h_b decrease by showing, in Fig.4.4(b), some density profiles for $n = 40$ at different Wi : as the flow gets higher, plot tails concentrate in a narrower region, monomers redistribute closer to the grafting wall and the trend is similar to the effect of an imposed compression on the brush surface (see, for example, Fig.??). A last consideration is worthwhile regarding the rms of the distance between neighbors in Fig.4.4(a) and, especially, the plot at the highest flow ($Wi = 1631$): a bigger displacement with respect to the equilibrium value, fixed by thermal fluctuations, is measured all along the chain, pointing to the mechanotransduction function of a polymer brush. Indeed, even for a completely flexible polymer brush as the one we simulate, at high enough flow, the shear stress is transmitted also in the hydrodynamically screened region [142].

For R_{ee} , θ and h_b the trends exhibited by long chains ($n \geq 36$) fall on the same curves. Therefore, for the following analysis we will fix a specific molecular weight and choose $n = 40$.

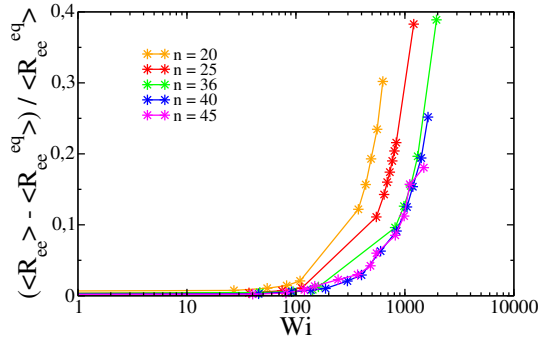


Figure 4.2: Relative chain elongation is reported as function of Wi and for different chain lengths n . Chain elongation is calculated as the average end-to-end vector amplitude R_{ee} relative to the equilibrium (without flow) value R_{ee}^{eq} .

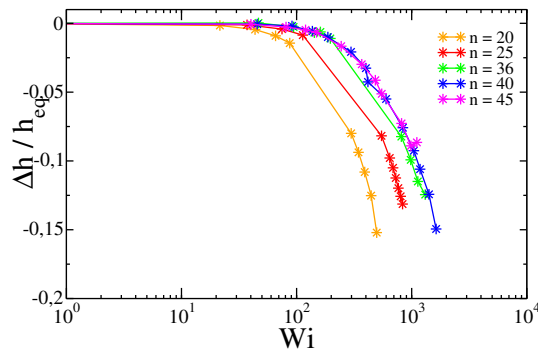
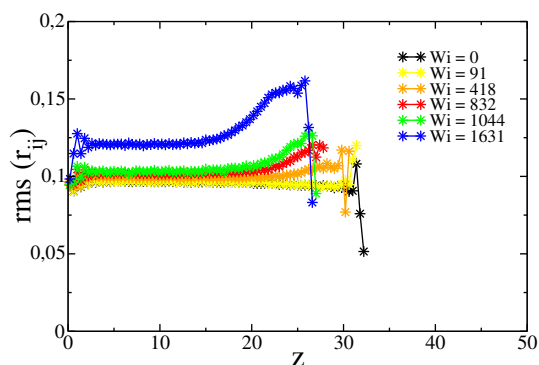


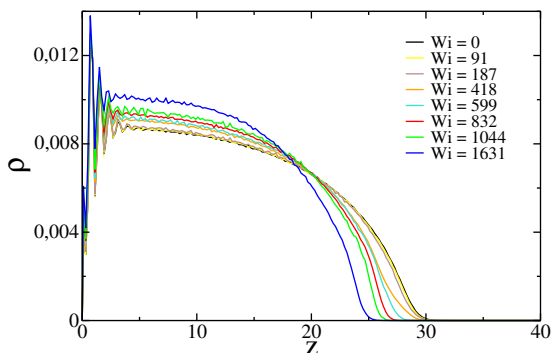
Figure 4.3: The brush height h relative to the equilibrium value h_{eq} as function of Wi and for different chain lengths n . The brush height is defined in Sec. 3.3. For $Wi < 100$ the height keeps basically constant, while for $Wi > 100$ the flow has the effect to compress the brush.

4.2 Solvent velocity field: the flow inversion

The solvent velocity profile $v_x(z)$, calculated by averaging the x -component of the velocity for each solvent particle as a function of its position z , is shown in Figs. 4.5.(a)-(b) for two Wi values, providing two typical examples. As expected, the functional shape of $v_x(z)$ in the region around the largest velocity v_{max} is well represented by a parabolic function with the expected amplitude. For all studied Wi , the parabolic function predicts that v_x vanishes when z approaches the brush height h_b , suggesting that the presence of a dense polymer brush restricts the pore by an amount equivalent to h_b . The velocity profile in the region $z < h_b$, i.e. the region densely occupied by the brush, is of particular interest. In some cases, *e.g.* the one presented in Fig. 4.5.(a), the fluid velocity inside the brush is small, consistent with a picture in which the hydrodynamic interactions are effectively screened by the presence of the polymer layer. In other cases, as shown in Fig 4.5.(b), the velocity profile exhibits a flow inversion at the interface between the brush and the bulk, *i.e.* around $z \sim h_b$, as previously documented for an analogous system [86], as well as when the solvent is replaced by a polymer melt [91,92]. In these previous studies, the onset of flow inversion was associated to the shear rate exceeding a certain threshold [86]. By contrast, we find that flow inversion takes place in distinct disconnected windows of Wi values. Indeed, we discover the existence of at least three different windows of flow intensities in which a backflow is observed. In between these regions the velocity profile at $z \sim h_b$ remains positive, resembling the one in Fig. 4.5.(a). Figure 4.5.(c)



(a)



(b)

Figure 4.4: In (a) the root mean square of the distance between neighboring monomers, $\text{rms}(r_{ij}) = \sqrt{\langle r_{ij}^2 \rangle}$, is plotted against the distance from the grafting wall and for different Wi . In (b) brush density profiles at different Wi are shown: as the imposed flow increases, monomers redistribute closer to the grafting wall, as in the case of a brush compression. Both panels regard a homodisperse brush with $n = 40$.

shows the minimum value v_{min} of the profile $v_x(z)$ near the surface of the polymer brush, as a function of Wi . By this definition, flow inversion is observed when $v_{min} < 0$. The identified three backflow regions fall around $Wi \sim 200, 400, 600$, respectively.

In Refs. [86, 91, 92] it was argued that the backflow is a consequence of the dynamics of single grafted chains, which undergo a recursive, imperfect cycle composed of: tilting, elongation and recoiling. Indeed, an elongated chain (and thus exposed to flow) is dragged by the shear stress along the flow direction and then recoiled back by entropic forces. By

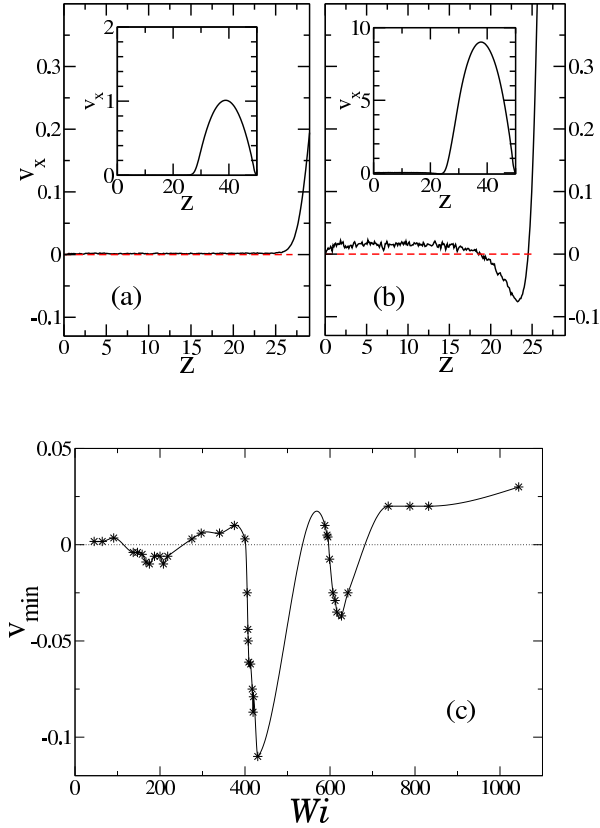


Figure 4.5: Panels (a) and (b) show the velocity profile in the whole channel (insets) and in the region close to the brush (main panels). In both cases, corresponding to (a) $Wi = 45$ and (b) $Wi = 418$, the profile is parabolic around v_{max} . In (a) no backflow is registered, while in (b) the flow inversion at $z \sim h$ is evident. Panel (c) reports the minimum value v_{min} of the $v_x(z)$ profile for different Wi (symbols). The line is a guide for the eye. It is possible to recognize three regions for which v_{min} assumes a negative value, signaling the presence of a backward flow.

examining the polymer trajectories we confirm the presence of such recursive motion for all Wi values, but such a cyclic motion is always observed (see the sequences in Fig.4.6), regardless of the presence of the backflow. Hence, the single-polymer motion alone is not enough to explain the onset of flow inversion.

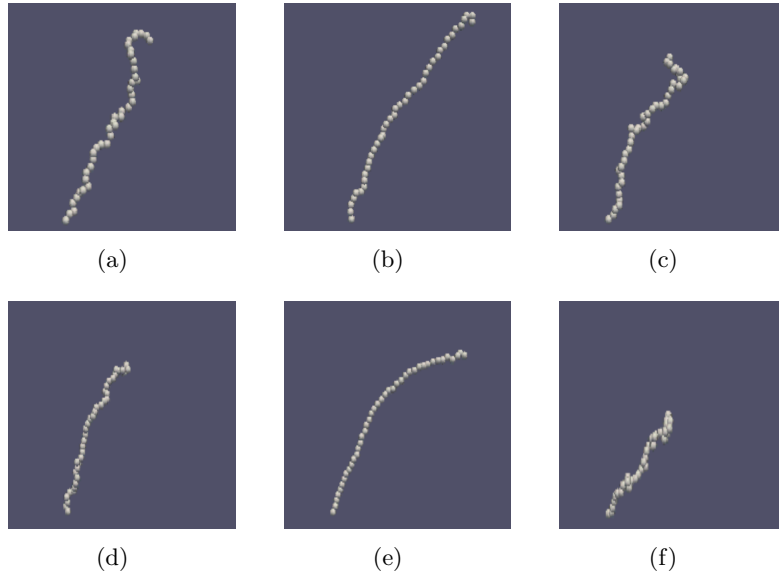


Figure 4.6: Comparison between two typical sequences for a sample chain inside the brush: (a-b-c) a case where backflow is observed ($Wi = 838$); (d-e-f) a case in which no backflow is recorded ($Wi = 1044$). In both sequences the recursive motion is detectable.

4.3 Collective polymer dynamics: brush surface waves

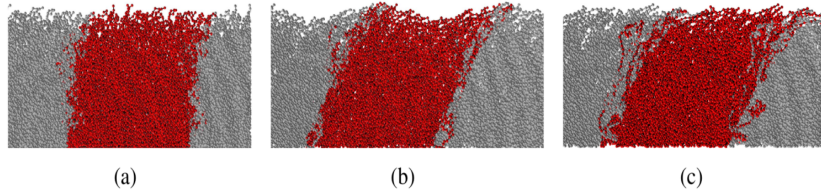


Figure 4.7: Sketches of the whole brush, corresponding to (a) $Wi = 91$, (b) $Wi = 418$ and (c) $Wi = 588$. In (a) the brush surface is basically flat, in (b) the surface is modulated by a traveling wave with $\lambda \sim L_x = 30$, $\nu = 0.077$ and $b = 1.18$ while in (c) the brush filaments tilt but no surface waves are present. We show the central box (in red) and the two nearest replicas (in grey) to highlight the periodic nature of the waves.

Investigating space and time correlations among different polymers, we discover a wave traveling over the brush surface in the same direction

as the imposed flow. The wave arises *if and only if* a backflow is present, suggesting a strong association between the surface wave and the capability of the brush to produce an inversion of the flow velocity around $z \sim h_b$. A visual inspection of the brush and of its dynamics nicely shows the collective behavior of the polymers. Figure 4.7.(a),(b) and (c) show typical snapshots of the system at low flow (no wave), intermediate flow (a surface wave appears) and at higher flows where waves are absent, respectively. We find that this traveling wave has a clear spatial periodicity of the order of the simulation box and a non-negligible amplitude. We characterize the surface wave by evaluating its frequency ν , wavelength λ and oscillation amplitude b . In order to do so we define the brush surface $S(x, t)$ as the position of the farthest monomer from the grafting wall occupying at time t the coordinate x , averaged over all y . The power-spectrum of the time Fourier transform of $S(x_0, t)$ (for an arbitrary x_0 value, inset of Fig. 4.8.(a)) displays, in all cases in which a flow inversion is observed, a sharp peak at a given frequency, as exemplified in Fig. 4.8.(a). We associate the position of this peak with the characteristic wave frequency ν . In some cases a much less intense peak is also observed at 2ν . Fourier transforming the signal $S(x, t_0)$ in real space for an arbitrary t_0 and averaging over all configurations provides a quantification of the wavelength λ . As shown in Fig. 4.8.(b), for all cases in which a flow inversion is present we find, as in the time domain, a dominant contribution from the longest λ that can propagate in a periodic system of size L_x and from its second harmonic (e.g. from wavenumbers k equal to $\frac{2\pi}{L_x}$ and $\frac{4\pi}{L_x}$). Fig. 4.8.(c) shows the Wi dependence of ν for systems with the same L_x (e.g. same λ). In each of the three disconnected regions of Wi values where flow inversion is present, ν increases approximatively linearly with Wi . Finally, we define the wave amplitude b as the standard deviation of $S(x, t)$ and the wave average height as $S \equiv \langle S(x, t) \rangle$. At our knowledge, the present study is the first one in reporting on the observation of a wave over a polymer brush surface. Neither previous simulations nor experiments have revealed such possible dynamics. Theoretical analyses have addressed the description of a brush surface deformation and modeled it as a monochromatic wave, but in those cases the deformation was imposed and not the result of hydrodynamic coupling [143, 144]. We will refer to one of those studies in the following part of this Chapter, but a deep and satisfactory investigation of this dynamics is a novel landscape to be drawn. We attempt such issue in the following.

We interpret the co-presence of flow inversion and surface waves in

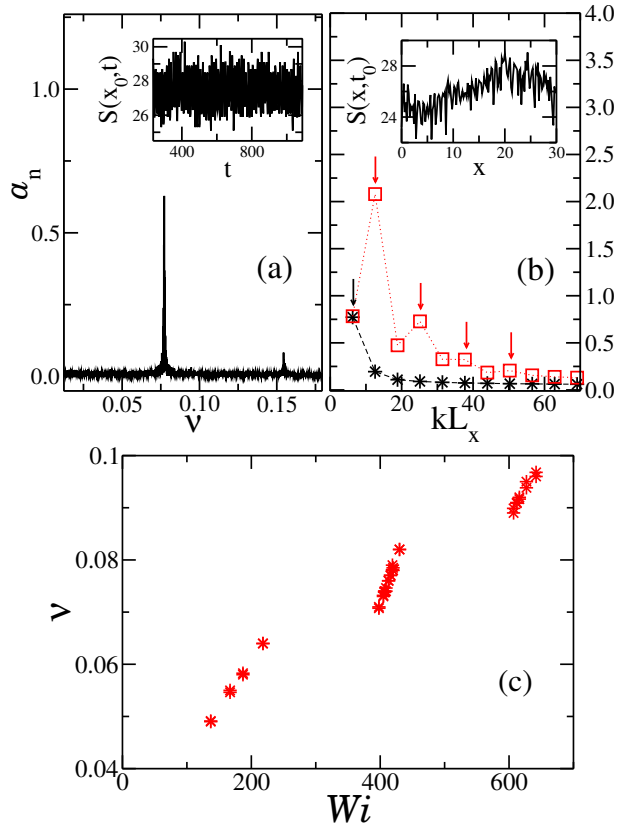


Figure 4.8: Fourier power-spectra: (a) in the frequency domain ν for the signal $S(x_0, t)$, (b) in the wavenumber domain $k = 2\pi/\lambda$ for the signal $S(x, t_0)$ (red squares indicate the spectrum in a bigger system $L_x = 180, L_y = 5$ and $L_z = 150$). The arrows highlight the position of the peaks. In both panels the first and second harmonics are present. The two insets show typical signals in real space. Panel (c) shows the characteristic frequency of the waves, which are found to be monotonically increasing functions of Wi .

light of the work done by Taylor on the mobility of microswimmers [132]. The idea is to map the polymer recursive motion, that we have described in Sect.4.2, into the dynamics of microswimmer cilia. A microswimmer is a microorganism that is able to propel itself at low Reynolds numbers by producing a two-step motion composed of a stroke and of an antistroke; the net effect of the periodic alternation of the stroke and antistroke results in a propelling velocity of the organism. In a similar way, we consider the recursive motion of the single polymer chain as composed of a “stroke” (the stretching and elongation along the flow direction) and an

“antistroke” (the entropic recoiling). The net effect is, in this case, the solvent backflow. Since it is detected only if polymers display a collective motion and produce a wave, we thus resort to the Taylor study. In his seminal paper, dating back to 1951, Taylor investigates the motion of a viscous fluid near a sheet under which sinusoidal waves are propagated with velocity U . If the ratio between the wave amplitude b and the wavelength λ is not too small, the sheet moves with a velocity V_{Taylor} in the opposite direction with respect to U . The relation between the sheet self-propelling velocity and the travelling wave features reads:

$$\vec{V}_{Taylor} = -\frac{2\pi^2 b^2}{\lambda^2} \left(1 - \frac{19}{4} \frac{\pi^2 b^2}{\lambda^2}\right) \vec{U}. \quad (4.3)$$

We associate the two-dimensional sheet with the brush surface and U with the velocity $\lambda\nu$ of the brush surface wave. Since the polymer brush is grafted to the wall and cannot translate but it affects the fluid close to its surface, we identify V_{Taylor} with the velocity of the solvent at the brush interface v_{min} . Therefore we exploit Eq. (4.3) to build a precise relation between the parameters entering in the wave phenomenon and the parameters controlling the flow inversion. Figure 4.9 shows, for each set of b , λ and U values associated to a specific Wi giving flow inversion, the comparison between $|V_{Taylor}|$ (calculated from Eq. (4.3)) and $|v_{min}|$. The trends associated with the behaviour of $|v_{min}|$ are perfectly recovered by the self-propelling velocity of a Taylor’s micro-swimmer, suggesting that the elastic brush can be considered as an anchored micro-swimmer, unable to move but able to propel the surrounding liquid.

We note that the Reynolds number Re_{DPD} for the simulated system is in the order of hundreds: $Re_{DPD} = \rho V l / \eta \sim 10^2$. This does not mean that the dynamics we have discussed so far corresponds to *liquid* dynamics at high Re . As a matter of fact, it should be recalled that the Schmidt number is $Sc_{DPD} \ll Sc_{liquid}$ in consequence of the operated coarse-graining. As discussed in Sect.2.3, the coarse-graining procedure makes the DPD fluid similar to a gas rather than a liquid, giving priority to length- and time- scalings, while sacrificing transport properties. In other words, a low Sc implies that hydrodynamic interactions do not propagate enough rapidly when compared to the time it takes anything to move. This explains why raising the Wi number in a DPD simulation guarantees the efficacy of hydrodynamics. We take this into consideration to determine

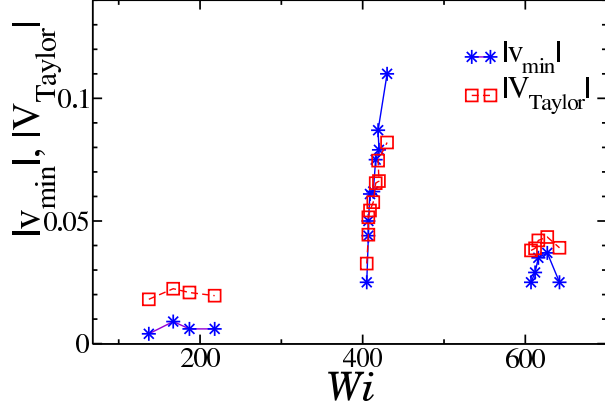


Figure 4.9: The mapping between the absolute value of the velocity profile minimum $|v_{min}|$ (stars) and the velocity V_{Taylor} obtained by plugging in Eq. (4.3) the wave amplitude b , the wavelength λ and the wave velocity $U = \lambda\nu$ evaluated for the brush surface wave at the given Wi .

the equivalent physical system and assume, here, the following mapping:

$$Sc_{DPD}Re_{DPD} = Sc_{liquid}Re_{liquid} \quad (4.4)$$

Therefore, our simulation set-up corresponds to water at $Re_{liquid} = Sc_{DPD}Re_{DPD}/Sc_{liquid} = 10^{-1}$. The successful analogy with the Taylor's work, valid in Stokes regime, is consistent with this mapping.

4.4 Polidispersity

We have dedicated one section of the previous Chapter to bidisperse brushes. Here we show the effect of their exposure to parabolic flow and detect how a mixture of different chains affects the velocity field and the phenomenology of flow inversion. At fixed $\langle n \rangle$, we observe a decrease of the maximum velocity with increasing PI , as plotted in the inset of Fig.4.10. Looking at the detail of the velocity profiles in Fig.4.10, such decrease turns to be the natural outcome of the increased brush height $h_b^{(PI)}$, that changes from $h_b^{(1)} = 20$, in the case of homodisperse brush with $n = 25$, to $h_b^{(1.362)} = 26$, in the case of bidisperse brush with $PI = 1.362$

($n_- = 10$ and $n_+ = 40$ and mixing ratio (1:1)). Indeed, from Eq.(2.13):

$$\frac{v_{max}^{(1)} - v_{max}^{(1.362)}}{v_{max}^{(1)}} = \frac{(z_{vmax}^{(1)} - h_b^{(1)})^2 - (z_{vmax}^{(1.362)} - h_b^{(1.362)})^2}{(z_{vmax}^{(1)} - h_b^{(1)})^2} \sim 0.36 \quad (4.5)$$

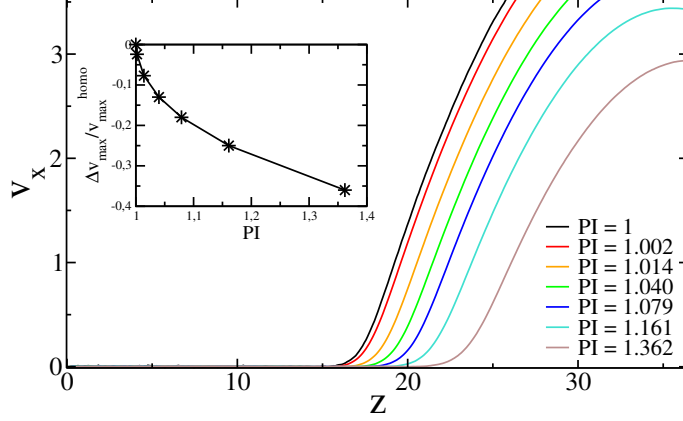


Figure 4.10: A portion is shown of the velocity profiles regarding bidisperse brushes with $\langle n \rangle = 25$ and different PI . The flow is imposed by mean of the constant acceleration $A = 0.01$. The PI values indicated in the legend correspond to the same fractions and mixing ratio as declared in Sect.3.3. The inset reports the v_{max} relative to the homodisperse brush with $n = 25$ as function of PI .

Moreover, polydispersity lowers the backflow, as evident from Fig.4.11. A reason for such effect could be traced out in the reduced chain density at the brush surface, since only the longer species actually feels hydrodynamic interactions, the shortest one being subdued to an enhanced compression (see the segregation effect discussed in Sect.3.3).

4.5 Possible origins of the surface wave

In Sect. 4.3 we have characterized the brush surface wave and investigated its link with flow reversal. By using the Taylor's relation of Eq.(4.3), we have provided a quantification of the backflow knowing the wave features. However, the mechanism leading to the onset of such propagating wave has not been clarified yet. For sure, in the present case, hydrodynamics is the driving force, but the conditions determining the wave formation have still to be identified. In addition, the presence of oscillations of finite amplitude suggests that a possible resonance effect may arise. Let's first

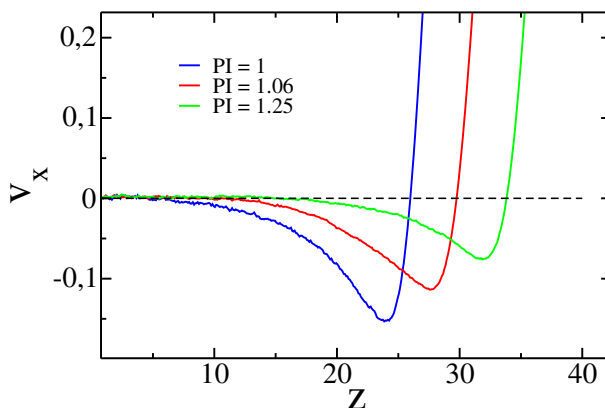


Figure 4.11: Zoom on velocity profiles in the brush region for bidisperse brushes with $\langle n \rangle = 40$ and $A = 0.05$. For such an imposed flow, the homodisperse brush ($PI=1$, in blue) displays flow reversal. On increasing PI the effect of the backflow is reduced. The two polydispersity indices $PI = 1.06$ and $PI = 1.25$ correspond to $(n_- = 30, n_+ = 50; 1;1)$ and $(n_- = 20, n_+ = 60; 1;1)$ respectively.

recall the basis of a resonant mechanism to see if it fits our present case study. An elastic structure subdued to small deformations in the vicinity of a stable equilibrium point is well described by a linear theory. The general solution for the dynamics is a linear superposition of the normal modes, harmonic oscillations characterized by a natural frequency and one independent from the other. Normal modes, thus, constitute a basis of decoupled oscillators. An external force \mathcal{F} acting on the system can excite unstable modes and give rise to resonances, namely the exponential growth of mode amplitudes with the appearance of spontaneous oscillations at preferential frequencies. In some cases, an additional effect can be produced and enter the dynamics: mode coupling. If the force is weak, $\mathcal{F} = \varepsilon f$, a linear theory is still acceptable and new solutions for the dynamics will consist in finding the new normal modes. In other words, the external force modifies the natural frequencies. Regarding polymer brushes, the flat interface represents the equilibrium state, while the developing of the traveling wave marks an instability driven by the hydrodynamic force. If the brush can be reasonably characterized as an elastic medium, then a resonance can take place. In such case, we need to identify the elastic modes that enter the dynamics and become unstable if excited by hydrodynamics. Before addressing such question, we review in the following some examples of surface waves that can offer a guideline

to deal with our specific case.

4.5.1 An overview on surface waves

In physics, surface waves are encountered in many fields. A polymer brush has intermediate properties in between a matrix of disconnected filaments, as it is actually built, and a continuous medium, as it is more conveniently considered when, for example, wave properties are analyzed. To dig into the possible origins of our specific wave or, at least, deepen the discussion on such regard, we propose hereafter an overview on various surface waves both on continuous and on filamentous systems.

Among the surface waves over continuous systems we mention: Rayleigh waves, propagating along solid surfaces [145], surface gravity waves, propagating along liquid surfaces [146], and fluttering, driven by hydrodynamics over elastic surfaces [147, 148].

1. Rayleigh waves

Rayleigh waves are acoustic waves that propagate at the surface of solid media. They induce both a transversal and longitudinal motion of particles and thus the overall particle trajectory is an ellipse with the major axis perpendicular to the surface. Particles at the surface track their ellipse in a counter-clockwise manner (for waves propagating from left to right). As the depth from the surface increases, the particle ellipse shrinks.

Those kind of waves are produced during earthquakes as a result of the superposition of compression and shear waves in the bulk where the epicenter is located. Involving up-down motion as well as back-and-forth motion, they are responsible for the most damage.

2. Surface gravity waves

Wind flowing at the water surface produces gravity waves by means of two main mechanisms: a transfer of energy by normal pressure and a transfer of energy by shear forces. Indeed, when blowing wind is in the turbulent regime, the velocity field, instead of being laminar and smooth, displays random fluctuations with respect to the mean flow. On consequence, a random fluctuation of stresses arises, acting both tangentially and normally on the air-water interface. If such fluctuating pressures have a frequency and wavelength that match water modes, a resonance arises that makes the wave amplitude grow. The Airy wave theory, valid for small wave amplitudes, yields

the following relations: in case of deep water ($\lambda \ll h$, where λ is the wavelength and h is the water depth), the wave angular frequency reads $\omega = \sqrt{gk}$ where g is the acceleration due to gravity, while in the limit of shallow water ($\lambda \gg h$), waves are non-dispersive and their speed is given by $c = \sqrt{gh}$.

Once the surface has been roughened, a new mechanism, so-called *critical-layer mechanism*, takes place: when the wave speed reaches the wind mean flow speed, the energy exchange from wind to water is more efficient and the wave keeps growing.

Within the linear theory of small amplitudes, water particles move in circles whose radius decreases with depth. The motion is clockwise (for a wave traveling from left to right).

3. Fluttering

A theory by Kumaran first [147] and Mahadevan [148] focuses on an elastic compressible structure in confined geometry and investigate the possibility of resonance mechanisms induced by viscous fluid flow. Indeed, the pressure load exerted by a viscous fluid flow produces hydrodynamic coupling and drives the system towards an instability called *flutter*, *i.e.* the appearance of spontaneous oscillations at given frequencies. Thus, hydrodynamics coupling makes an elastic mean become unstable even at low Reynolds numbers. As elucidated in Ref. [147,148], in the limit of weak hydrodynamic coupling and small amplitudes, the system always develops a fluttering instability for Weissenberg numbers larger than a certain critical value. Some phenomena in this category are familiar to common observation: flapping of a flag or of a sail, as well as snoring.

Among surface waves over a disconnected system of vibrating objects we briefly discussed two examples: metachronal waves [149, 150] and waves over crop canopies [151, 152].

1. Metachronal waves

A metachronal wave is produced by individual parts of a system performing the same motion one after the other. Thus, it differs from a synchronous motion in which the individual parts move in the same way all together. It is known to develop in ciliated systems, namely flat surfaces covered by a matrix made of equally spaced flexible filaments [149, 150]. Exposed to a flow, filaments do not interact directly, but thanks to the long-range of hydrodynamics interactions, after some transient time, they reach a state

whose dynamics is characterized by a regular phase shift between subsequent filament rows. In those cases the matrix is composed by active matter elements and the sequence of configurations they assume is assigned *a priori* (on the contrary, polymer brushes are passive media).

2. Waves over canopies

A model for the wave formation on passive media such as crop canopies (because of flowing wind) or aquatic vegetations (because of water flow) has been developed by De Langre *et al.* [151, 152]. They require also the inertial term of Navier-Stokes (NS) equations to account for the instability initiating the surface modulation. Indeed, it is assumed that the canopy is partially crossed by the wind and the wind is slowed down inside it, therefore a velocity difference ΔU is assumed between wind over the canopy and wind inside the canopy. This difference, together with the possibility to neglect the viscous term of the NS equations, gives rise to the Kelvin-Helmholtz instability in the fluid and vortices (billows) are displayed. When the unstable modes frequencies equal the natural vibrational mode of the filaments, the canopy itself exhibits a wavy surface. The two systems, canopy and fluid, couple. An interesting outcome of such model is that inside the range of ΔU producing coupling, a frequency lock-in mechanism takes place: on increasing ΔU , the fluid unstable mode frequencies are expected to increase too while, in case of coupling, they block onto the canopy frequency. The energy provided to the system results rather in an increased oscillation amplitude of such unstable modes.

4.5.2 Polymer brush as an elastic solid: importance of the shear modulus

Our dense polymer brush presents non-trivial dynamics and nonlinearities come into play along with the increase of Wi . However, in the limit of small perturbations, that we identify with the region $0 < Wi \leq 138$ (till the first wave appearance), the Fredrickson's theory provides a useful characterization for a polymer brush [143]. According to such theory, the brush is envisioned as a solid, more precisely as an incompressible continuum elastic film. Indeed, its free energy for small surface deformations has the same expression as for a solid, at all wavelengths. The brush surface wave of wavenumber q and angular frequency ω is therefore classified

as a Rayleigh wave with the following dispersion relation:

$$\omega = \sqrt{\frac{G}{\rho_m}} q, \quad (4.6)$$

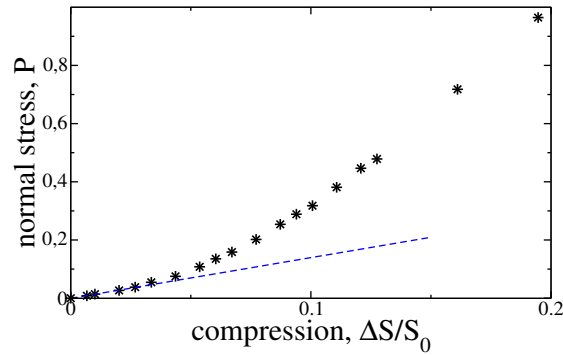
with G and ρ_m the shear modulus and the mass density of the brush medium. Guided by such analogy with a solid, we calculate the elastic moduli of our dense polymer brush: the Young modulus Y and the shear modulus G . The following analysis does not pretend to be complete nor conclusive: it is proposed as a dimensional guideline and the development of a model equation is postponed to future works.

We plot in Fig.4.12(a) the relation between an imposed compression and the correspondent brush stress response. We simulate a Surface Force Apparatus experiment (see also Sect.3.3) and compress the brush by mean of an ideal plate posed at a certain distance from the grafting wall; the plate behaves as a rigid wall of infinite mass (which a bounce-back reflection is applied on) for monomers, while it is transparent to solvent particles. The stress is estimated by $P = F/A$, where F is the time average of the total DPD conservative force exerted by each monomer on the plate surface of area A . In Fig.4.12(b), on the other hand, we show the relation between a shear stress exerted on the brush and the correspondent shear strain. The shear stress is imposed by the flow and it is calculated as $\sigma = \eta \overline{Wi}/t_{brush} = \eta \bar{\gamma}$, while the shear strain is the average of the component along the flow direction of the end-to-end vector, $\Delta x = \langle R_{ee,x} \rangle$. It is evident from the two figures how those relations are not simply linear ones. On consequence, the polymer brush has a nonlinear elastic character that comes into play as the Wi gets higher; more precisely, it gets stiffer and stiffer on increasing the rate of compression/strain.

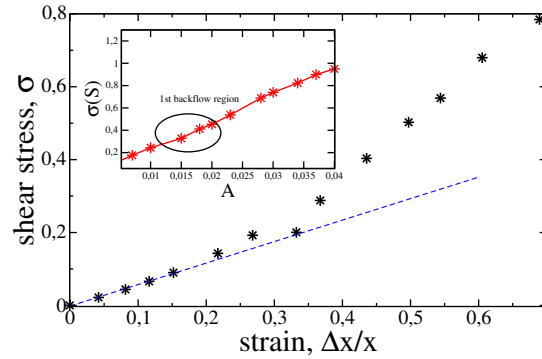
In the region of small deformations, we extract the values of the two elastic moduli, Y and G . A linear fit yields $Y = 1.4$ and $G = 0.59$. Setting $\rho_m \approx 1$ (at the surface layer, monomers have a lower density than the system imposed one, see also Fig.3.5), the dispersion relation in Eq.(4.6) yields $\nu \approx 0.03$, i.e. the same order of magnitude of the observed surface wave frequencies (see Fig.4.8.(c)). This corroborates the idea of the brush surface deformation as a Rayleigh wave. Moreover, we calculate the shear stress at the brush surface S as $\sigma_S = \eta dv(z)/dz|_{z=S}$. From the plot in the inset of Fig.4.12(b) of σ_S as function of the imposed flow A , it is underlined how the first region of flow inversion arises at $\sigma_S(A = 0.015) = 0.34$, thus in the same order of magnitude as G . In other words, instability takes place as soon as the brush experiences at

its surface a shear stress comparable to its shear modulus G . Actually, the shear modulus of our polymer brush results bigger than σ_S of almost a factor 2, but we ascribe such discrepancy to an effective overestimation of the brush shear modulus: the deformations reported in Fig.4.12(b) derive from an average of R_{ee}^x over *all* the chains, while only a fraction of them is effectively exposed to flow, the rest being screened.

As previously declared, our analysis is not exhaustive, but we want to stress the importance of the brush shear modulus in defining a criterion for the onset of polymer brush instabilities. Indeed, these dimensional findings bolster the idea of a resonance between the hydrodynamic shear



(a)



(b)

Figure 4.12: The brush nonlinear response to compression (a) and to strain (b). As the applied normal or tangential load increases, the brush stiffens. The blue plots are linear fits in the region of small deformations yielding an estimation of the brush Young modulus (a) and shear modulus (b). The inset appearing in (b) reports the shear stress σ exerted by the viscous flow on the brush surface S as function of the applied solvent acceleration A .

stress and the brush shear modulus, bringing to the formation of Rayleigh-like waves. We indicate in the following relation

$$\sigma_S \sim G \quad (4.7)$$

the necessary condition for the onset of the instability. Below such threshold we expect the polymer brush to behave as a rigid wall, without inducing any anomaly in the velocity profile. The leading role of G in determining brush instabilities resides also in the evidence that a polymer brush is more easily shear-deformed than compressed. From our simulations, $Y/G \approx 2$, but it is worth noticing that for real polymer brushes $Y/G \approx O(10^2)$, therefore the Young modulus is greater than the shear modulus of some orders of magnitude. For example, the endothelial glycocalyx has $Y = 390\text{Pa}$ [153] and $G = 6.7\text{Pa}$ [154]. Thus, a hydrodynamic load would easier excite shear modes than compression modes.

As elucidated in Ref. [143] the analogy of the polymer brush with a solid incompressible medium holds in the limit of small deformation amplitudes. The phenomenology we have discussed here, however, covers a wide range of Wi and exhibits three well-separated instability regions in which the wave frequency increases as function of Wi (see again Fig. 4.8.(c)). These features are not contemplated in the framework of the Fredrickson's model. We speculate that the richness of our scenario is due to the hydrodynamic coupling and to the strong nonlinear behavior exhibited by the polymer brush, which constitutes a much more complex system than the idealized one considered in Ref. [143]. Specifically, we find that, as a function of the imposed flow, the brush stiffens (Figs.4.12(a) and 4.12(b)) and its height decreases (see Fig.4.3). In addition, the surface modulation is produced by hydrodynamics and hydrodynamics breaks the symmetry of the brush deformation. Those effects are not included in the theoretical framework introduced by Fredrickson *et al.* [143]. The development of an extension of their theoretical approach to the more complicated case of a system with flow-dependent properties is under way.

On consequence of such analysis, we suggest the use of a novel Weissenberg number to discriminate between regimes in which it is possible or not possible that polymer brush instabilities are developed: instead of a t_{brush} estimated by the relaxation of the polymer end-to-end vector amplitude, we propose to cast the brush timescale from a brush collective property and, precisely, to use $t_{brush} = \eta/G$. Thus, the new Weissenberg number reads $Wi = \dot{\gamma}\eta/G$ and the condition $Wi = 1$ corresponds to the

onset of the first shear instability (i.e., the first wave appearance).

Résumé (french version)

Alors que les propriétés d'équilibre d'une brosse de polymères ont été décrites par la vaste littérature sur le sujet, il y a un manque de données et consensus sur la dynamique des brosses de polymères soumises à l'écoulement. La plupart des études théoriques ont tenté de modéliser les brosses de polymères comme couches poreuses décrites par des équations de type Brinkman [131], ou comme une collection dense de fibres très rigides [83]. Ces approches n'incluent pas les résultats récents, mentionnés précédemment dans l'Introduction, sur les brosses de polymères sous écoulement.

Au lieu d'utiliser l'accélération imposée A comme mesure de la force de l'écoulement on introduit une quantité sans dimension: le nombre de Weissenberg. Le nombre de Weissenberg Wi est défini comme le rapport $Wi := t_{brush}/t_{flow}$, où t_{brush} est un temps structurel caractéristique de la brosse non perturbée et t_{flow} fournit une estimation de l'échelle de temps typique associée au flux. En suivant la littérature du domaine, on évalue t_{brush} comme le temps de relaxation des polymères le plus long et t_{flow} comme l'inverse de la vitesse de cisaillement moyenne.

En ce qui concerne la dynamique de la chaîne simple, nous estimons l'angle de basculement moyen, qui augmente en augmentant Wi . Un tel basculement provoque une compression de la brosse (diminution de la hauteur de la brosse).

La mise en œuvre d'un solvant explicite donne la possibilité de calculer de façon auto-cohérente le profil de vitesse du solvant $v_x(z)$, en opérant une moyenne des composantes x de la vitesse pour chaque particule de solvant en fonction de leur position z . La forme fonctionnelle de $v_x(z)$ dans la région autour de la vitesse maximale v_{max} est bien représentée par une fonction parabolique avec l'amplitude attendue pour la solution de l'équation de Navier-Stokes en géométrie *slit-pore*. Pour toutes les valeurs de Wi étudiées, la fonction parabolique prédit que v_x disparaît lorsque z s'approche de la hauteur h_b de la brosse, ce qui suggère que la présence d'une brosse dense de polymères réduit la hauteur du canal d'une quantité équivalente à h_b . Le profil de vitesse dans la région $z < h_b$, c'est-à-dire la région densément occupée par la brosse, se révèle d'intérêt particulier. Dans certains cas, la vitesse du fluide à l'intérieur de la brosse est petite; dans d'autres cas, le profil de vitesse présente une inversion dans la direction du flux à l'interface entre la brosse et le reste du canal. On constate que l'inversion de flux a lieu seulement dans des fenêtres distinctes et déconnectées de valeurs de Wi . En effet, on découvre l'existence d'au moins trois fenêtres différentes pour l'intensité d'écoulement dans

lesquelles le flux inverse est observé.

La littérature soutient que le flux inverse est une conséquence de la dynamique des chaînes greffées simples, qui réalisent un mouvement récursif, un cycle imparfait composé de: inclinaison, allongement et retour. En effet, une chaîne allongée (et donc exposée au flux) est entraînée par la contrainte de cisaillement le long de la direction d'écoulement, puis ramenée en arrière par des forces entropiques. Nous confirmons la présence de ce mouvement récursif, mais un tel mouvement cyclique est observé toujours, pour toutes les valeurs de Wi , que le reflux soit relevé ou pas. Par conséquent, le seul mouvement du polymère simple ne suffit pas pour expliquer les raisons de l'inversion de flux.

On propose, alors, une explication en termes de dynamique collective des polymères. En étudiant les corrélations spatiales et temporelles entre différents polymères, on découvre une onde se déplaçant sur la surface de la brosse dans le même sens du flux imposé. L'onde se produit si et seulement si un reflux est présent, suggérant une forte association entre l'onde de surface et la capacité de la brosse de produire une inversion de la vitesse d'écoulement autour de $z \sim h_b$. Aucune simulation antérieure ni expérience avait révélé une telle dynamique possible. Nous interprétons la coexistence d'inversion de flux et de l'onde de surface au vu du travail de Taylor sur la mobilité des micro-nageurs [132] et construisons une analogie entre les paramètres entrant dans le phénomène de l'onde et les paramètres contrôlant l'inversion de flux. Les tendances associées à la vitesse du reflux v_{min} , valeur minimale du profil de vitesse autour de $z \sim h_b$, sont parfaitement reproduites par la vitesse auto-propulsive d'un micro-nageur de Taylor, suggérant que la brosse peut être considérée comme un micro-nageur ancré, incapable de se déplacer, mais capable de propulser le liquide environnant.

En exposant à l'écoulement une brosse bidispersée, on conclue que la polydispersité abaisse la vitesse du reflux. Une raison de cet effet pourrait être indiquée dans la densité réduite de chaînes à la surface de la brosse, puisque seulement l'espèce des chaînes plus longues est effectivement entraînée par les interactions hydrodynamiques, la plus courte étant soumise à une compression additionnelle (voir l'effet de ségrégation discuté dans le chapitre précédent).

En physique, les ondes de surface sont rencontrées dans de nombreux domaines. Une force externe F agissant sur une structure élastique peut exciter des modes instables et donner lieu à une croissance exponentielle des amplitudes de modes, avec l'apparition d'oscillations à

fréquences préférentielles. Une brosse de polymères possède des propriétés intermédiaires entre une matrice de filaments, telle qu'elle est réellement construite, et un milieu continu, telle qu'elle est plus commodément considérée lorsque, par exemple, les propriétés de l'onde sont analysées. Des exemples d'ondes apparaissant dans des systèmes faits de filaments déconnectés sont les ondes métachronales et les ondes sur les canopées des récoltes, tandis que des exemples d'ondes apparaissant dans des systèmes continus sont les ondes de Rayleigh, se propageantes le long des surfaces solides, les ondes de gravité, se propageantes le long des surfaces liquides, et le *fluttering*, produit par l'hydrodynamique sur des surfaces élastiques.

Selon une théorie de Fredrickson, la brosse peut être envisagée comme un solide, plus précisément comme une couche mince élastique. En effet, son énergie libre pour de petites déformations superficielles a la même expression que pour un solide, à toutes les longueurs d'onde, et ce type d'onde est classé comme onde de Rayleigh. En calculant le module de cisaillement G du système brosse et la contrainte de cisaillement σ expérimentée par les polymères à l'interface de la brosse, on constate que l'instabilité a lieu dès que la brosse subit à sa surface une contrainte de cisaillement comparable à son module de cisaillement.

Comme nous avons déjà déclaré, notre analyse n'est pas exhaustive, mais nous voulons souligner l'importance du module de cisaillement pour établir un critère qui nous permet de reconnaître les instabilités de la brosse de polymères. On indique dans la relation suivante, σG , la condition nécessaire pour la manifestation de l'instabilité (onde). Au-dessous de ce seuil on s'attend à ce que la brosse de polymères se comporte comme une paroi rigide, sans aucune anomalie dans le profil de vitesse du liquide écoulant.

A la suite de cette analyse, on suggère l'utilisation d'un nouveau nombre de Weissenberg pour discriminer les régimes dans lesquels il est possible ou pas que des instabilités soient développées dans une brosse de polymères: on propose de calculer l'échelle de temps de la brosse à partir d'une propriété collective et, précisément, d'utiliser $t_{brush} = \eta/G$. Ainsi, le nouveau nombre de Weissenberg est défini comme $Wi = \dot{\gamma}/G$ et la condition $Wi = 1$ correspond à la première instabilité de cisaillement (c'est-à-dire, la première apparence de l'onde).

Chapter 5

Red Blood Cells through brush coated microchannels

By mean of the coarse-graining model presented in Chapter 2, a RBC is included in the DPD simulations. For the first time the same code handles both polymers and RBCs under flow. The RBC speed and deformation are first estimated in a bare cylindrical pore and then compared with data obtained in a brush coated channel.

Analyses of polymer brushes under simple liquid flow have an importance *per se*, since those systems are ubiquitous in nature and easily built up in laboratories. Even regarding blood circulation it is known that, in most of blood vessels, polymers interact only with plasma: indeed, a cell-free layer separates the endothelial glycocalyx from RBCs (the Fahraeus-Lindqvist effect, illustrated in Sect.1.3.2). Therefore, the polymer dynamics is expected to fall within the case of brush interacting with simple fluid, as treated in the previous chapters. However, in small capillaries, the cell-free layer is significantly reduced and the presence of a wall polymeric coating can turn to be dynamically relevant even for the big cells. Thus, in order to complete the overview on the biological environment presented in Chap.1, we explore the interaction of a RBC with a polymer brush.

A characterization of the single RBC dynamics in microcapillaries with detailed phase diagrams can be found in Ref. [155]. Here, we want to focus on the interaction between the cell and the polymeric coating. At our knowledge, this is the first time that both polymers and RBCs

are handled by the same numerical code. Even if the wide span of the involved physical lengthscales (hundreds nanometers for the brush height, ten micrometers for the cell) actually does not allow a perfect match of the physiological conditions, we believe it is worth addressing the problem with mesoscale and self-consistent DPD simulations. In other words, those simulations could shed light on the more general question pertaining how macromolecular matrices interact with deformable flowing objects and possibly perturb their dynamics.

A picture of the RBC inside a brush coated channel is presented in Fig.5.1. As explained in Sect.2.4.3, we recover axial symmetry and switch from slit-pore to cylindrical pore geometry, so that the cylinder inner surface will be uniformly covered with linear chains. We recall that in this set-up the solvent velocity profile matches the Poiseuille formula (Eq.(2.28)), where the viscosity is $\eta_{out} = 0.9$. The main features of a RBC that are object of measurement in microcapillaries and during microfluidic experiments are the cell shape and speed [62, 156]. We will provide estimations for its velocity and deformation, both in case of bare walls and in case of hairy walls, for several values of the imposed flow.

By changing the power dependence for the weight function in the DPD dissipative and stochastic DPD forces to $\omega^S(r_{ij}) = (1 - r_{ij}/r_c)^{1/4}$, we obtain $\eta_{in} = 1.53$. Thus, the viscosity contrast is fixed to $\lambda = 1.7$. The shear capillary number is $Ca_{shear} = 0.077 \div 0.27$, corresponding to the range $A = 0.1 \div 0.6$ of imposed acceleration. Coupling between the fluid flow and the RBC dynamics is achieved through DPD viscous friction and stochastic force between membrane vertices and the surrounding solvent particles. No DPD conservative force acts between the membrane and the solvents.

5.1 RBC in bare channel

A RBC in a pore of diameter comparable with the cell size undergoes relevant deformations. Here, we aim to simulate a capillary of 10 μm in diameter. The consequent parameter values are discussed in Sect.2.4.4. With those physical values, we produce solvent velocities in the order of millimeters per seconds. The time step is $\Delta t = 0.002$.

According to literature [62], common shapes are the *parachute*, the *croissant* and the non-axisymmetric *slipper* one. Our numerical simulations are able to reproduce all those kind of deformations. In Fig.5.2 we report examples of those shapes with comparisons to the experimental

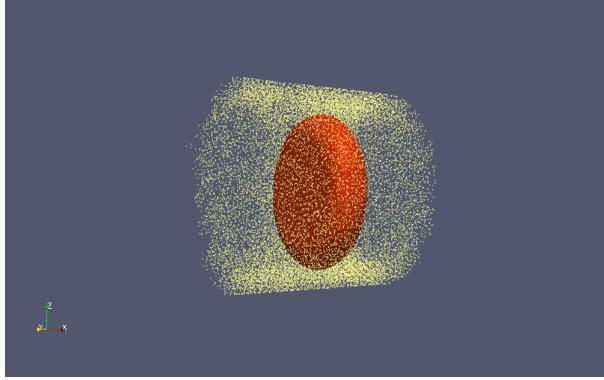


Figure 5.1: A picture of the new set-up system: a RBC is included in a brush coated cylindrical pore.

high-speed camera observations in capillaries of 10 μm in diameter.

The speed \vec{V}_{RBC} of the RBC is calculated as the average over time of its center of mass (com) velocity

$$\vec{V}_{RBC} = \left\langle \sum_i^{N_v} \frac{\vec{v}_i}{N_v} \right\rangle \quad (5.1)$$

where $\langle \dots \rangle$ indicates the time average and the index i , $i = 1, \dots, N_v$ runs over each membrane point. We recall that the mass is the same for all membrane vertices. Given the confinement in the radial direction, we report only on the component along the flow direction x . Results are plotted in Fig.5.3. We find a perfect agreement with theoretical model [157, 158] and experimental measures [159] in bare channels. Indeed, according to the cited literature, $V_{x,RBC} = 1.5\bar{v}$, where \bar{v} is the average flow velocity related to v_{max} by the relation $\bar{v} = v_{max}/2$ in Poiseuille flow.

In order to characterize the cell deformation we calculate the eigenvalues of the gyration tensor. The gyration tensor $G_{\alpha\beta}$ is defined as

$$G_{\alpha\beta} = \sum_i^N (\vec{r}_i^\alpha - \vec{r}_{com}^\alpha)(\vec{r}_i^\beta - \vec{r}_{com}^\beta) \quad (5.2)$$

with $i = 1, \dots, N_v$ and $\alpha, \beta = x, y, z$. It measures the geometrical distribution of particles. Its eigenvalues are ordered as $\lambda_1 \leq \lambda_2 \leq \lambda_3$. Combinations of them give the shape descriptors R_g^2 , δ , S and c . The squared radius of gyration R_g^2 corresponds to the trace of the gyration

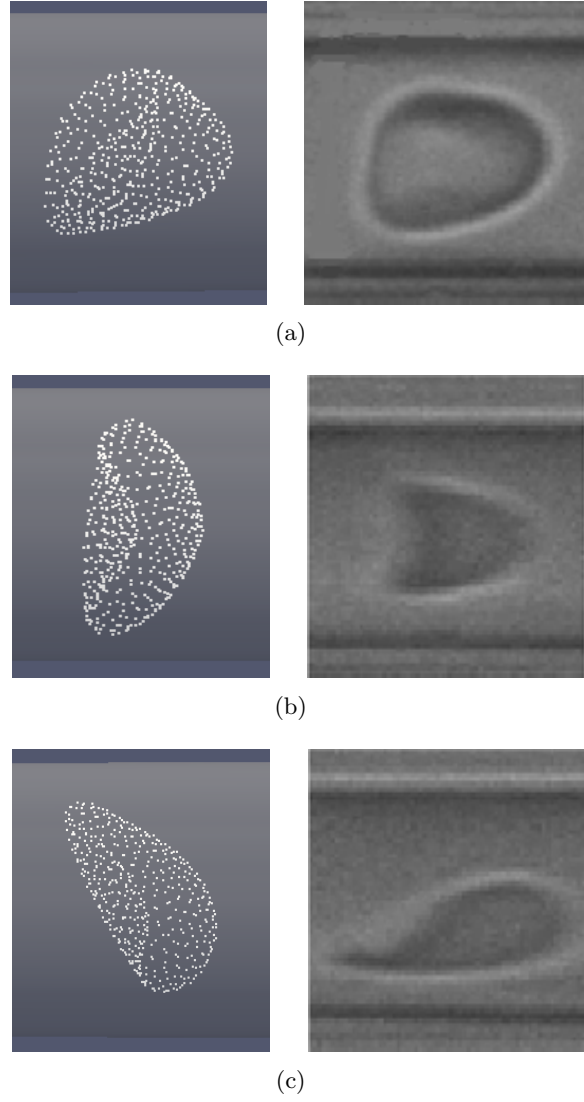


Figure 5.2: RBC shapes obtained by numerical simulations in comparison with experimental ones found in capillaries of 10 μm : (a) parachute, (b) croissant and (c) slipper.

tensor: $R_g^2 = \lambda_1 + \lambda_2 + \lambda_3$. The other three parameters are defined as follows:

$$\delta = \frac{(\lambda_1 - \lambda_2)^2 + (\lambda_2 - \lambda_3)^2 + (\lambda_3 - \lambda_1)^2}{2(\lambda_1 + \lambda_2 + \lambda_3)^2} \quad (5.3a)$$

$$S = \frac{(3\lambda_1 - R_g^2)(3\lambda_2 - R_g^2)(3\lambda_3 - R_g^2)}{R_g^6}, \quad (5.3b)$$

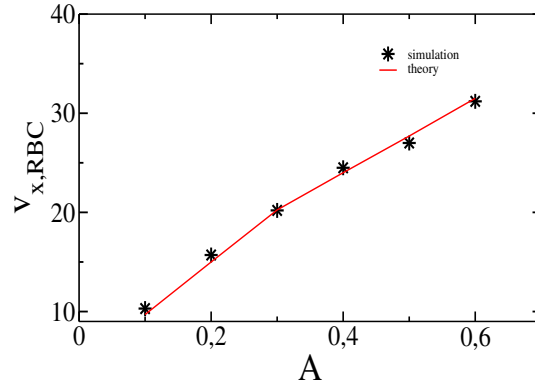


Figure 5.3: The x -component of the velocity of the RBC center of mass at different imposed flows. Numerical results are in perfect agreement with the theoretical prediction by Secomb et al. [157].

$$c = \lambda_3 - \lambda_2. \quad (5.3c)$$

The *anisotropy*, δ is positive definite and ranges from 0 (in case of spherical distribution) to 1 (in case points are aligned). The parameter S is called *prolateness*: it indicates prolate shapes if $0 \leq S \leq 2$ or oblate shape if $-0.25 \leq S \leq 0$. It biases the definition of the last parameter, namely the *acylindricity* c : since we deal with oblate shapes, the definition in Eq.(5.3c) assures that the condition $c = 0$ holds in case of perfectly cylindrical conformations. On the contrary, for prolate shapes, the same condition is verified by the definition $c = \lambda_2 - \lambda_1$.

We first report the time-averages of such shape descriptors, in Fig.5.4, for different imposed flow, together with their equilibrium values. At equilibrium, the RBC has its characteristic discoidal biconcave shape and its radius of gyration amounts to $R_g^2 = 87.9$. With the switching on of solvent flow all the shape parameters change and their trends indicate that the cell undergoes larger and larger deformations on increasing the pressure drop. The deformed cell tends to more compact shapes (Fig.5.4(b) and Fig.5.4(a)), while maintaining its oblateness (Fig.5.4(c)). At the same time, it assumes a more cylindrical conformation (Fig.5.4(d)). In summary, hydrodynamics molds the cell such that, with its increased deformation, it opposes a lower flow resistance.

In a range of few millimeters per second for the flow velocities, a RBC experiences shear and bending forces able to deform it, but not enough high to expand its membrane area, thus the cell is known to conserve both volume and surface area. As discussed in Chap. 2, this corresponds

to a constant reduced volume ν . With the parameter listed in Sect.2.4.4, the model generates the value $\nu = 0.64$ at equilibrium (good match of $\nu = 0.65$, found by experimental estimations). However, as far as the imposed flow gets higher, a drift in the reduced volume is registered: looking at Fig.5.5, the decrease is of order 10^{-3} , outside the statistical error ($O(10^{-4})$). Anyway, it is so small that dynamics is not affected.

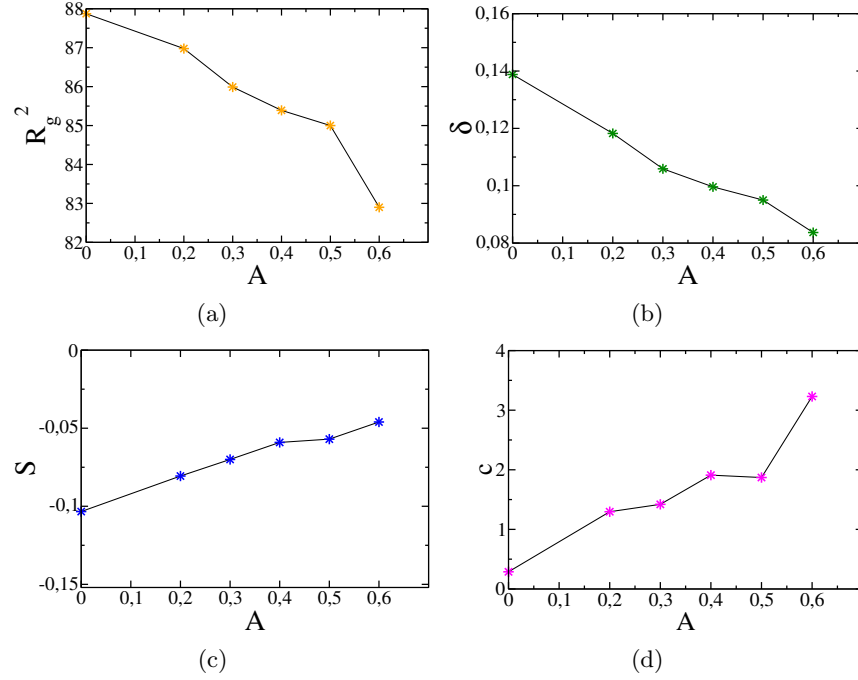


Figure 5.4: Time averages of the shape descriptors, obtained by combinations of the gyration tensor eigenvalues (see the main text for definitions) as function of the imposed flow: (a) the squared radius of gyration R_g^2 , (b) the anisotropy δ , (c) the prolateness S and (d) the acylindricity c . All the trends show an increasing deviation from the equilibrium values as far as the imposed flow get stronger, thus confirming that, at higher velocities, the RBC enhances its deformation rate.

Additional considerations are extracted from tracking the shape descriptors over time. Those trends contain similar amount of information, therefore, for the sake of conciseness we only show the ones relative to R_g^2 , in Fig.5.6(a), and to δ , in Fig.5.6(b). It is revealed how the increase of the pressure drop makes more difficult the settlement of stable shapes and orientations: frequent tumbling events, flips and large deformations are observed.

5.2 Polymer brush as a rigid compartment for a RBC

For the sake of computational time, we lower the grafting density to $\sigma_{graft} = 0.5$. A further decrease of the time step is necessary to avoid chain extension beyond the FENE limit, thus $\Delta t = 2 \cdot 10^{-4}$. A conservative force between the membrane and the polymers is activated, with the reasonable choice of $a_{MP} \equiv a_{PP} = 25$. Because of lengthscales and geometry, chains are constrained to the following molecular weights: $2 < n < 10$. In Fig.5.7 we plot, as example, the density profile for $n = 6$: given the low grafting density, the profile at the brush periphery decays smoothly. We maintain the definition $h_b = 2\langle z \rangle$, as it gives a reasonable estimation: $h_b = 2.7$.

In coated channels ($n = 6$ and $h_b = 2.7$) the RBC velocity is lower with respect to the bare one (Fig.5.8(a)) but the cell deformation is comparable (Figs.5.8(b)). Therefore, our simulations highlight the joined contribution of flow strength and confinement in inducing the cell shape, since such equivalent deformation at lower speed must be ascribed to the brush presence. The decrease of $V_{x,RBC}$ is matched by $V_{x,RBC} \approx 1.6\bar{v}$, where \bar{v} is the average Poiseuille velocity in the coated pore. In summary, the polymer brush constitutes a compartment enhancing the cell confinement.

Asymmetric shape are still observed and are more stable in comparison to the ones observed in bare channels, as revealed by the plots of the

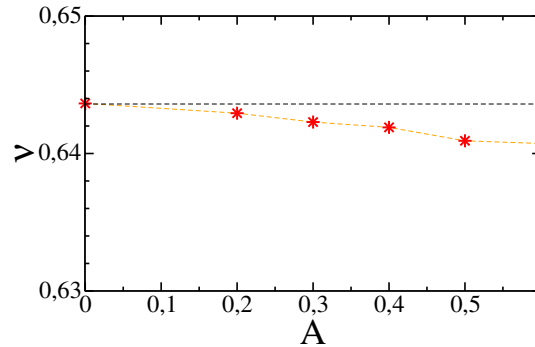
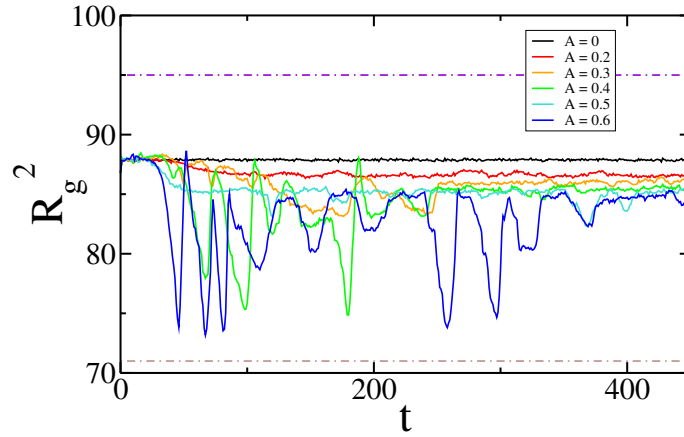
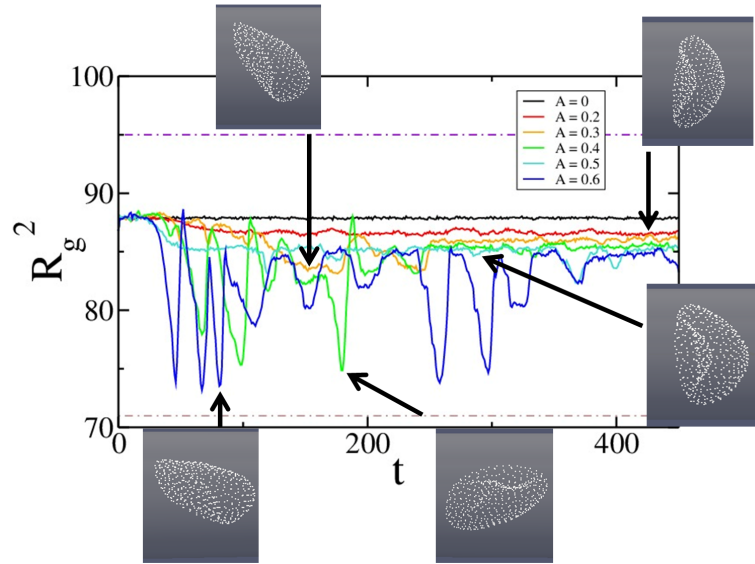


Figure 5.5: Drift of the reduced volume ν : it slightly decreases ($O(10^{-3})$) as function of the imposed flow. Such trend can be ascribed to the difficulty, at high cell velocities, in maintaining a constant local and global area by mean of the model constraints discussed in the Subsect.2.4.2.



(a)



(b)

Figure 5.6: Shape descriptors over time at different imposed flows: (a) the gyration radius and (b) the anisotropy. In (a) the two dotted-dashed lines correspond to the gyration radius of a sphere having volume V_{RBC} (in brown) and to the gyration radius of a sphere with surface area A_{RBC} (in violet). At high velocities, the transient time leading to a stable deformation rate gets longer and frequent tumbling events and shape changes are observed. In (b) some of the cell shapes are indicated.

shape descriptors over time in Fig.5.8(c) (again, we report only R_g^2 for conciseness). The transient time leading to the stationary shape is also

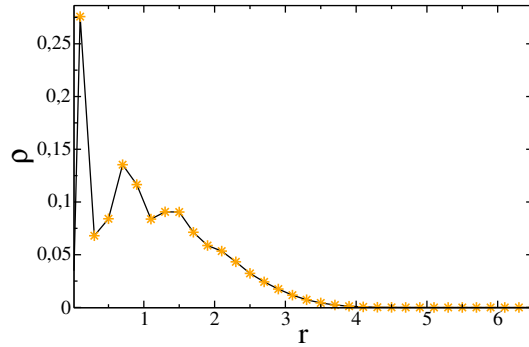


Figure 5.7: Brush density profile in cylindrical geometry. With $n = 6$ and $\sigma_{graft} = 0.5$, the profile is closer to a parabolic monomer distribution.

shorter.

Finally, at constant imposed flow ($A = 0.2$) $V_{x,RBC}$ decreases on increasing the brush thickness, as plotted in Fig.5.9(a), while the cell deformation is slightly more pronounced, as indicated by the average anisotropy in Fig.5.9(b). On such points, a recent paper should be mentioned regarding experiments that produce different results. According to such experimental study, the microcapillary coating has an on-off effect on the red blood cell velocity: below a certain threshold for the brush thickness ($h_b \approx 120\text{nm}$), the RBC does not detect the brush presence and its speed is the same as in a bare channel; beyond such threshold, instead, $V_{x,RBC}$ settles on a lower value that keeps constant independently of the specific value of h_b . The inverse proportionality with respect to the brush thickness that they found for the velocity of the pure fluid (see Ref. [42]) does not hold for the RBC velocity. The cell response to the increase of h_b is rather expressed in an increase of the cell deformation rate [156]. From our findings, on the contrary, we conclude that inverse proportionality is valid also between the RBC velocity and the coating thickness. One possible explanation of such discrepancy can be pointed out in the different range of brush thicknesses that has been explored: from 50 nm to 350 nm in Ref. [156], from 600 nm to more than 1 μm in our simulations, considering the length unit reported in Eq.2.38 and values from $h_b = 1.85$ ($n = 3$) to $h_b = 3.98$ ($n = 8$). Indeed, it is reasonable to expect that also the cell velocity, and not only the cell shape, becomes sensitive to brush thickness, if the latter is a more prominent layer.

We conclude with a last considerations on the effects of polydispersity

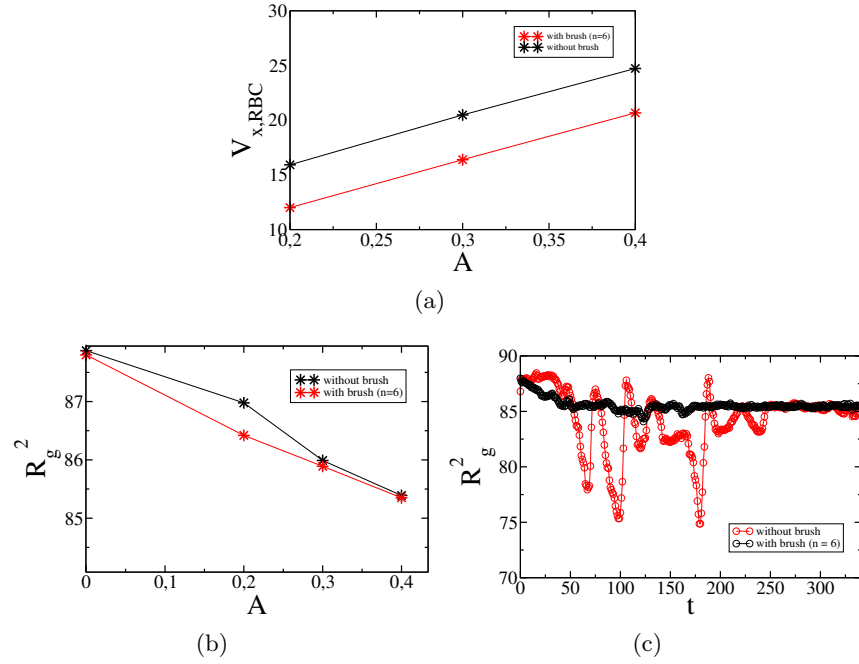
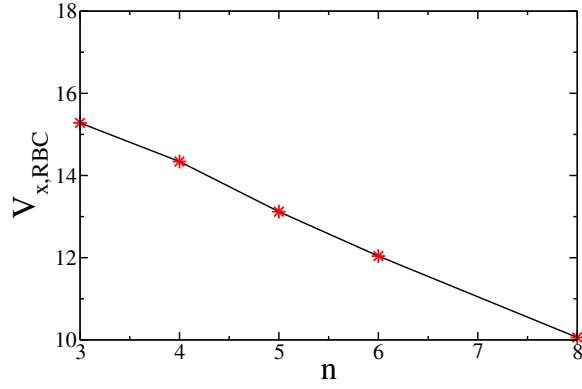


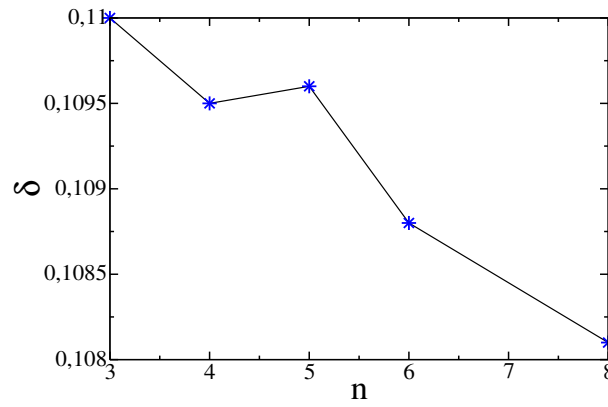
Figure 5.8: Comparisons of RBC flow in bare and hairy channels for different imposed flows. In (a) it is highlighted the cell slowdown in presence of a polymer brush coating with $n = 6$. In (b) the focus is on the radius of gyration, as representative measure of the deformation rate: it is only slightly lower than the value found in the bare channel. Moreover, as shown in (c) for $A = 0.4$, its trend over time reveals that cell shapes are more stable than in bare pores.

on the cell dynamics. We compare observations for the homodisperse brush $n = 6$ to observations for two bidisperse brushes with $\langle n \rangle = 6$, one with $PI = 1.03$ ($n_- = 5$, $n_+ = 7$, mixing ratio (1:1)) and the other with $PI = 1.44$ ($n_- = 2$, $n_+ = 10$, mixing ratio (1:1)). This last case corresponds to the highest polydispersity index we can reproduce in this geometry. We find no appreciable difference in the RBC speed when it flows over a homodisperse brush or a bidisperse brush with low PI , while a decrease of the cell speed is observed in the channel coated by the brush with $PI = 1.44$, as reported in Figs.5.10(a). Differently, looking at the gyration radius, no change in the cell deformation rate can be detected as function of PI , as evident from Fig.5.10(b). Irregularities of the brush surface are maybe too detailed to be appreciated on the cell scale.

This Chapter has been offered as a preliminary analysis. Considerations on future works are deferred to the Conclusion.

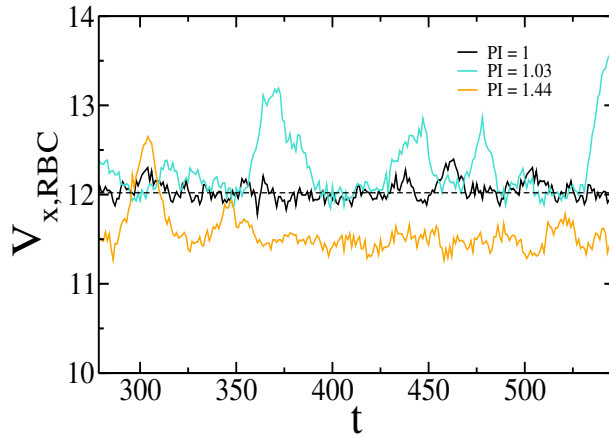


(a)

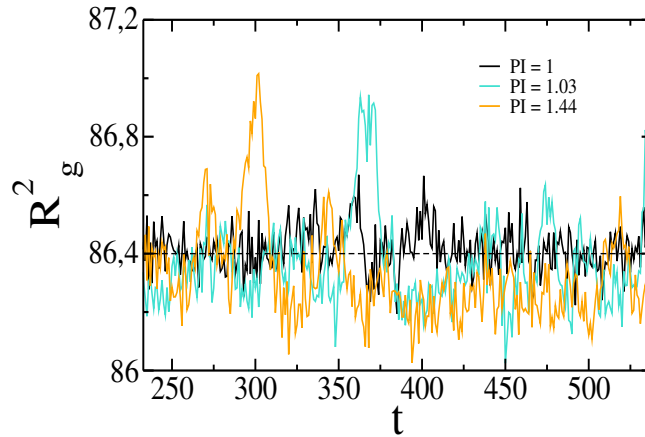


(b)

Figure 5.9: Dynamics of the RBC in a coated channel as function of polymer brush thickness, indicated by n : (a) as the number of monomers per chain increases, the cell is slowed down; (b) the anisotropy δ marks a slight decrease. The grafting density is $\sigma_{graft} = 0.5$ and the imposed acceleration is $A = 0.2$.



(a)



(b)

Figure 5.10: The RBC flowing over bidisperse polymer brushes with $\langle n \rangle$ compared to the homodisperse brush with $n = 6$: in (a) it is reported the cell speed and in (b) its radius of gyration. The cell speed, even if sensitive to the presence and thickness of a channel coating, it is not affected by a low polymer brush polydispersity ($PI = 1.03$), while it is slowed down if the brush polydispersity is higher ($PI = 1.44$). The cell radius of gyration displays no appreciable difference as function of PI . The dashed line in the two graphs indicates the average RBC speed and radius of gyration in case of homodisperse brush.

Résumé (french version)

Dans les capillaires les plus petits, la couche d'écoulement sans cellules est significativement réduite et la présence d'un revêtement de polymères à la paroi peut devenir relevante pour la dynamique, même pour celle des cellules. Ainsi, afin de compléter la vue d'ensemble présentée au Chapitre 1, on explore l'interaction d'un objet déformable avec une brosse de polymères. Une caractérisation de la seule dynamique des globules rouges dans les micro-capillaires avec des diagrammes de phase détaillés peut être trouvée dans la Réf. [155]. Ici, nous voulons plutôt concentrer l'attention sur l'interaction entre le globule et le revêtement de polymères. À notre connaissance, c'est la première fois que les deux structures, polymères et globule rouge, sont manipulés par le même code numérique.

Même si la large gamme d'échelles de longueurs physiques (centaines de nanomètres pour la hauteur de la brosse, dix micromètres pour le globule) ne permet pas de réaliser parfaitement dans les simulations les conditions physiologiques, nous croyons que aborder le problème avec la technique à l'échelle mésoscopique et auto-cohérente de la DPD peut ajouter des nouveaux détails. En d'autres termes, ces simulations pourraient éclairer la question plus générale relative au comment les matrices de macromolécules interagissent avec des objets déformables sous écoulement pour éventuellement perturber leur dynamique.

Un globule rouge dans un canal de diamètre comparable à sa taille subit des déformations. Ici, on essaye à simuler un capillaire de 10 μm de diamètre. Selon la littérature, les formes que le globule peut assumer sont à "parachute", à "croissant" et à "pantoufle", qui n'est pas axisymétrique. Nos simulations numériques sont capables de reproduire toutes ces déformations.

La vitesse V_{RBC} du globule est calculée comme la moyenne dans le temps de la vitesse de son centre de masse. Afin de caractériser la déformation cellulaire, on utilise le tenseur gyrationnel. Les combinaisons de ses valeurs propres donnent les descripteurs de forme R_g^2 , δ , S et c .

Nous rapportons d'abord les moyennes temporelles de ces descripteurs de forme pour différents écoulements imposés, ainsi que leurs valeurs à l'équilibre. À l'équilibre, le globule a sa forme biconcave discodale caractéristique. Sous écoulement, tous les paramètres de forme changent et leurs tendances indiquent que la cellule subit des déformations de plus en plus grandes en augmentant le débit de pression. En résumant, l'hydrodynamique moule le globule de sorte que, avec des déformations plus importantes, il oppose une résistance plus faible à l'écoulement.

Des considérations supplémentaires sont extraites en suivant la dépendance du temps des descripteurs de forme. On révèle comment l'augmentation de la chute de pression rend plus difficile la réalisation de formes et d'orientations stables: événements fréquents de *tumbling*, retournements et grandes déformations sont observés.

Dans les canaux revêtus, par souci de temps de calcul, on abaisse la densité de greffage et une nouvelle diminution du pas de temps Δt est nécessaire pour éviter que les chaînes puissent s'allonger au-delà de la limite posée par le potentiel FENE. La vitesse du globule dans les canaux revêtus est plus faible par rapport à la vitesse dans les canaux nus, mais la déformation de la cellule est comparable. Par conséquence, nos simulations mettent en évidence la contribution conjointe de la résistance à l'écoulement et du confinement pour induire la forme de la cellule. Des formes asymétriques sont encore observées et sont plus stables que celles observées dans les canaux nus. Le temps transitoire conduisant à la forme stationnaire est également plus court.

Enfin, à débit constant, la vitesse du globule diminue en augmentant l'épaisseur de la brosse. Ce résultat n'est pas en accord avec les expériences présentées dans un papier récent [156], qui montre au contraire une vitesse du globule qui n'est pas dépendent de l'épaisseur de la couche polymérique. Une explication possible d'une telle divergence peut être dans la gamme différente d'épaisseurs de brosses qui a été explorée: à partir de 50 nm à 350 nm dans la Réf. [156], de 600 nm à plus de 1 μm dans nos simulations. Il est raisonnable que la vitesse de la cellule, et non seulement la forme de la cellule, devient sensible à l'épaisseur de la brosse, si celle-ci est une couche plus proéminente.

Ce Chapitre a été présenté à titre d'analyse préliminaire. Des considérations sur les travaux futurs sont reportés dans la Conclusion.

Chapter 6

Final discussion

Before summarizing our results and reviewing our conclusion, we devote the present, short, Chapter to few points that we prefer to discuss at this final stage of the reported thesis.

6.1 Technical issues: one more success for DPD

The use of DPD to simulate polymer dynamics has been often criticized because of the repulsive potential: too soft to prevent crossing between polymers. We calculate the crossing probability p_{cross} as $p_{cross} = \exp(-\Delta E(\bar{r})/k_B T)$ where $\Delta E(\bar{r}) = V^C(0) - V^C(\bar{r})$ and \bar{r} is the average distance between interacting monomers of different chains. Our simulations yield $\bar{r} \approx 0.4$. Thus, with the values reported in Sect.2.3, we obtain

$$\Delta E = \frac{1}{2} a_{PP} \left(1 - \left(1 - \frac{\bar{r}}{r_c} \right)^2 \right) \sim a_{PP} \bar{r} \approx 10. \quad (6.1)$$

The crossing probability, finally, is $p_{cross} \approx 10^{-4}$. Such probability is not so high considering that the chain number is in the order of some hundreds, therefore crossing can happen. In general, a consequence of crossing is the change in polymer topology. Fortunately, this is not relevant for our analysis, since polymers are linear grafted chains and crossing will not induce any topology change. Anyway, new algorithms have been proposed in literature to correct this artifact [160]. Out-of-equilibrium DPD turns to be adequate even for the reproduction of the backflow phenomenon: this last one being the result of a collective effect, it is not sensitive to the single chain crossings. Moreover, the low Schmidt number does not hinder the propagation of efficient hydrodynamic interactions, provided that the DPD Wi number is enough high. This thesis

testifies that phenomenologies that were considered impossible to recover with DPD are actually feasible, thus confirming the leading role of DPD among the coarse-graining techniques.

6.2 Finite size effects on the surface wave phenomenon

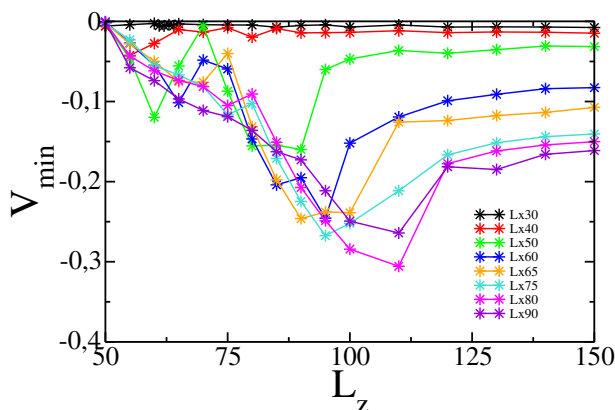
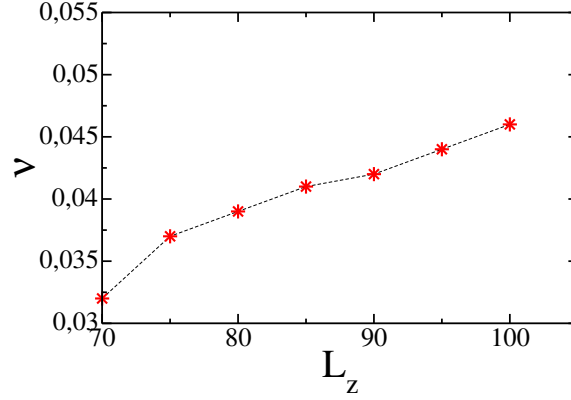


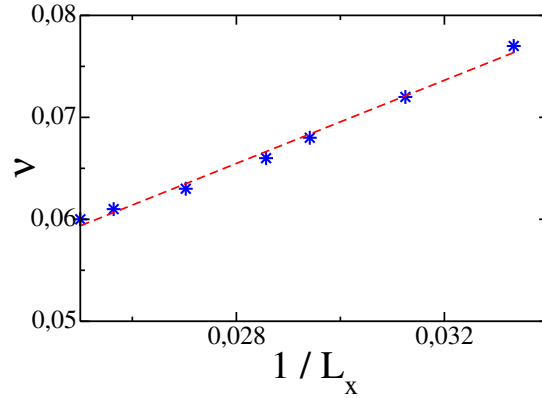
Figure 6.1: Investigation of finite size effects on the flow inversion phenomenon: the v_{min} at the brush interface is plotted as function of the channel width L_z for different channel lengths L_x . Sizes are increased up to three times both in L_x and in L_z . The flow strength is fixed ($A = 0.01$). All reported values are negative, meaning that the backflow is a robust phenomenon taking place also in significantly bigger systems. Precisely: on increasing the channel width, v_{min} settles in a plateau; on increasing the channel length, v_{min} slightly decreases.

The discussed surface wave phenomenon pertains simulations carried out in a box of size $L_x = 30$, $L_y = 5$ and $L_z = 50$. We remark that wave propagation is observed also in systems of considerably bigger size. Indeed, we have investigated the influence of finite size effects increasing the channel length L_x and the channel width L_z at fixed acceleration A : the wave persists. In Fig.6.1, we show the minimum of the solvent velocity profile at $z \sim h_b$ in channels up to the triple in L_x and to the triple in L_z . The acceleration is $A = 0.01$. On increasing L_z , v_{min} reaches a plateau and settles on a non-zero value. The wave amplitude b follows the same trend, in accordance with the Taylor's relation in Eq.(4.3). We recall that an increase of the channel width, even if at constant acceleration,

produces an increase of the bulk velocity and therefore an increase of Wi . Such Wi increase reflects on an increase of the wave frequency (see Fig.6.2(a)). Such finding is coherent with the plot ν vs. Wi of Fig.4.8.(b), where Wi has been changed by increasing A at fixed system sizes. Fixing the width, thus keeping a constant Wi number, the wave increases in wavelength ($\lambda = L_x$) and decreases in frequency, as shown in Fig. 6.2(b) for $30 < L_x < 40$, such that the propagation speed keeps constant.



(a)



(b)

Figure 6.2: Trends of the wave frequency ν on changing the system size: (a) the frequency increases as function of the channel width L_z and (b) decreases as function of the channel length L_x . In (a) the increment in L_z at constant acceleration $A = 0.01$ produces bigger bulk velocities, with consequent raise of the Weissenberg number. In (b) the acceleration is $A = 0.05$. The linear fit (in blue) indicates the the wave increases in wavelength ($\lambda = L_x$) and decreases in frequency such that the propagation speed keeps constant.



Figure 6.3: A snapshot for a larger studied systems ($L_x = 180$, $L_y = 5$ and $L_z = 150$) with a surface wave with multiple crests of wavelength $L_x/2 \approx 90$ ($Wi = 340$). Again, we show the central box (in red) and the two nearest replicas (in grey) to highlight the wave periodicity.

We find that in big channels multiple wave crests can be displayed (see Fig. 6.3). This suggests that the finite size of the simulation box exerts a cutting on the density of states, making it possible to observe only waves with wavenumbers which are integer multiples of $2\pi/L_x$. The wave amplitude b as function of L_x , reported in Fig.6.4(a), resembles the behavior of the unstable mode amplitudes of a Swift-Hohenberg equation, prototype of dynamical equations exhibiting instability and wavelength selection:

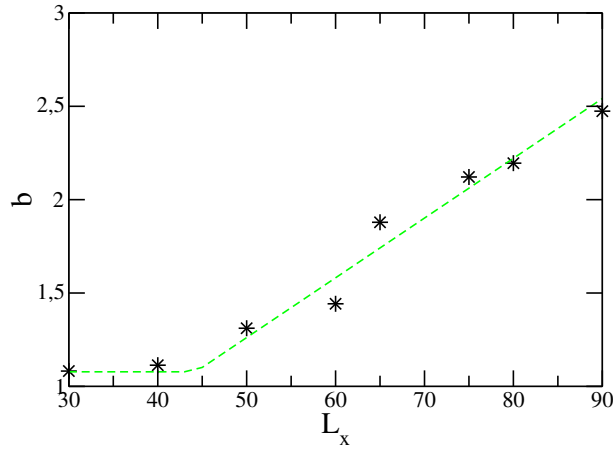
$$\partial_t u = \delta u - (1 + \partial_{xx})^2 u - u^3, \quad (6.2)$$

where u is the scalar order parameter (the local surface height, in the polymer brush case). However, in longer channels we found that several wavelengths are allowed: as shown in Fig.6.4(b), several harmonics have a non negligible amplitude. Thus, the characterization of the surface modulation as a simple monochromatic wave loses significance.

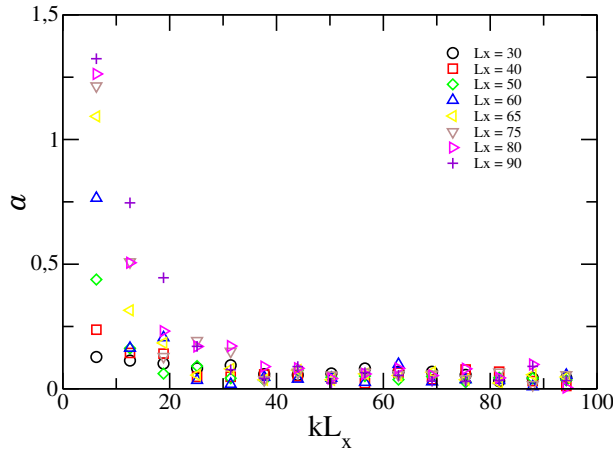
Finally, we observe a huge reduction of the bulk maximum velocity as function of the channel length, as shown in Fig.6.5. Different profiles correspond to different L_x while all the other parameters keep constant (especially, $L_z = 140$ and $A = 0.01$). Such decrease reaches a saturation value around the 60%. At the moment, we have no possibilities to produce an explanation. We remark that those simulations contain almost one million particles and that a further increase of the system size is frustrated by computational limits.

6.3 Speculations

As previously discussed, we ascribe the presence of disconnected Wi regions displaying backflow to nonlinear effects: as the imposed flow raises, the brush undergoes more pronounced deformations and, as a result, it stiffens. A linearly increasing shear stress, as produced by increasing A , is not strong enough to induce the instability again and the shear stress



(a)



(b)

Figure 6.4: Wave features as function of channel length L_x : (a) the wave amplitude increases linearly with wavelengths; (b) the Fourier spectrum in the wavenumber domain for $L_z = 150$ does not correspond to monochromatic signal and several harmonics have non negligible amplitudes.

at the surface has to jump to larger values before new waves settle. Such scenario is made even more complicated by the hydrodynamic coupling with polymer dynamics. Indeed, we report here of a peculiar effect related to the wave phenomenon. In Figs.6.6 the flow rate $Q = L_y \int_0^{z_{vmax}} \rho v(z) dz$ is plotted against the flow strength A . Because of the asymmetry of the simulated system (polymer are only at the bottom wall) the integral is defined between $z = 0$ and $z = z(v_{max})$, thus corresponding to half Q in

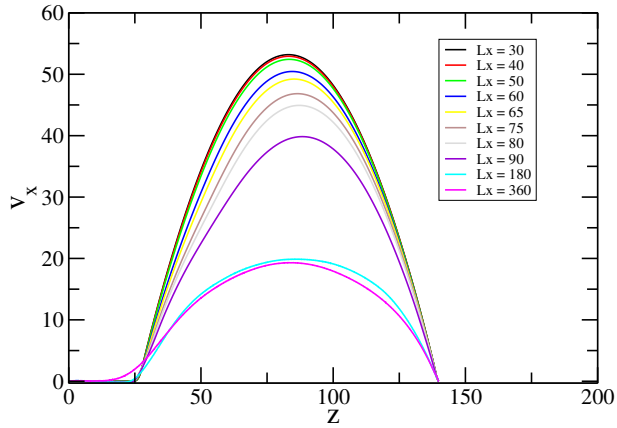
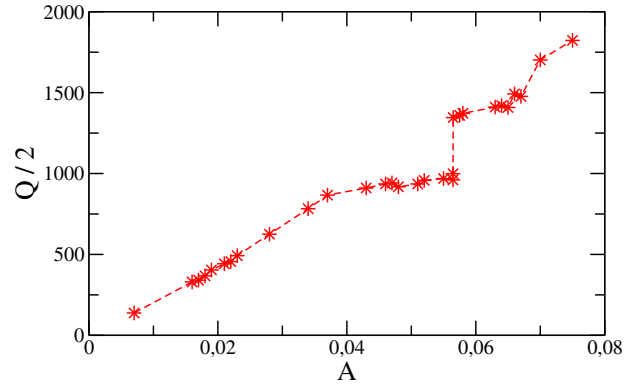
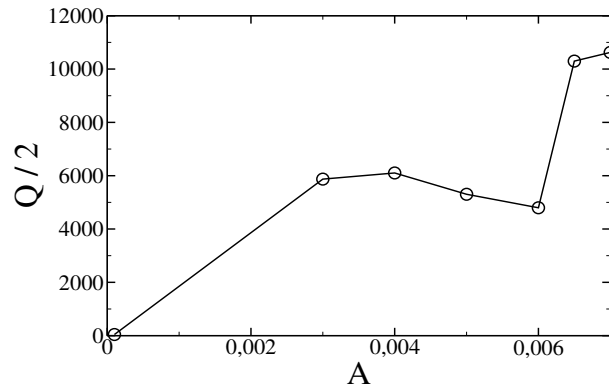


Figure 6.5: Significant reduction of the maximum velocity as function of the channel length in a channel of $L_z = 140$. The phenomenon is accompanied by flow reversal at the interface and therefore by the surface wave. The trend shows a saturation around a 60% decrease. The acceleration is $A = 0.01$.

a symmetric channel. The two images refer to two systems of different size. The first one regards the system $L_x = 30$, $L_y = 5$ and $L_z = 50$ that we have thoroughly discussed, while the second one pertains $L_x = 180$, $L_y = 5$ and $L_z = 150$. Focusing on the first image, it is evident how, instead of a linear trend, two plateau are displayed in correspondence of the second and third surface wave regions. The velocity profiles of those system points deviate slightly from the parabola expected in a reduced channel whose half-width is $H = z_{vmax} - h_b$. We speculate that a hydrodynamic coupling enter the dynamics and produces a sort of lock-in mechanism, similar to the one reported for the crop canopy system in Sect.4.5.1 and treated in Ref. [151] in full details. The flow is considered to locks-in onto a natural mode frequency of the brush and the supplied energy, instead of resulting in increasing the bulk fluid velocity, feeds the instability: the brush motion is enhanced, as revealed by the higher values of $|v_{min}|$, (see Fig.4.5.(c)). For the second plot, the decrease of the maximum velocity is even more pronounced and reaches 50%. A full clarification could derive from a model equation encompassing all those nonlinear dynamic sources and will be postponed to future work.



(a)



(b)

Figure 6.6: The volumetric flow rate $Q/2 = L_y \int_0^{z_{vmax}} \rho v(z) dz$ as function of the imposed acceleration A (the choice of the integral interval considers Q as the flow rate in a symmetric slit-pore, with polymers on both the walls). Panel (a) concerns the thoroughly discussed system with $L_x = 30$, $L_y = 5$ and $L_z = 50$, while panel (b) refers to a larger channel ($L_x = 180$, $L_y = 5$ and $L_z = 150$). In both cases significant plateau, deviating from the linear expected trend, appear.

Résumé (french version)

Avant de résumer nos résultats et de présenter nos conclusions, on dédie ce court chapitre à quelques points spécifiques que on préfère discuter à ce stade final de la thèse.

L'utilisation de la technique DPD pour simuler la dynamique des polymères a été souvent critiquée à cause du potentiel répulsif: trop souple pour empêcher le croisement entre les polymères. En général, une conséquence du croisement est le changement de la topologie du polymère. Heureusement, ce n'est pas relevant pour notre analyse, puisque les polymères sont des chaînes greffées linéaires et un éventuel croisement n'induirait aucun changement de topologie. La méthode de la DPD devient adéquat même pour la reproduction du phénomène de reflux: ce dernier étant le résultat d'un effet collectif, il n'est pas sensible aux croisements des chaînes simples. Cette thèse témoigne que des phénoménologies considérées impossibles à réaliser avec la DPD sont tout à fait réalisables, confirmant ainsi le rôle de premier plan de la DPD parmi les techniques de coarse-graining.

Le phénomène de l'onde de surface discuté concerne des simulations dans une boîte de taille donnée L_x , L_y et L_z . Nous remarquons que la propagation des ondes est également observée dans des systèmes de taille considérablement plus grande. En effet, nous avons étudié l'influence des effets de taille finie en augmentant la longueur L_x du canal et sa largeur L_z à accélération A fixée: l'onde persiste.

On constate que dans les grands canaux des crêtes d'onde multiples peuvent être affichés. Cela suggère que la taille finie de la boîte de simulation exerce une coupe sur la densité des états, permettant d'observer seulement des ondes avec des nombres d'ondes qui sont des multiples entiers de $2\pi/L_x$.

Enfin, on observe une énorme réduction de la vitesse maximale dans le canal. En fonction de la longueur du canal, on trouve des profils de vitesse différents alors que tous les autres paramètres restent constants (en particulier, $L_z = 140$ et $A = 0,01$). Cette diminution atteint une valeur de saturation autour du 60%. Pour le moment, nous n'avons pas d'explication. On remarque que ces simulations contiennent presque un million de particules et qu'une augmentation supplémentaire de la taille du système augmenterait considérablement les temps de calcul.

On attribue la présence de plusieurs régions de Wi montrant un reflux à des effets non linéaires: lorsque le débit imposé augmente, la brosse subit des déformations plus prononcées et, par conséquent, elle se raidit. Une

contrainte de cisaillement linéairement croissante, telle que celle produite par l'augmentation de A , n'est pas assez forte pour induire de nouveau l'instabilité et donc la contrainte de cisaillement à la surface doit sauter à des valeurs plus grandes avant que des nouvelles ondes s'installent. Tel scénario est rendu encore plus compliqué par le couplage hydrodynamique avec les polymères. Une clarification complète pourrait dériver seulement d'une équation modèle englobant toutes les sources dynamiques non linéaires et sera reporté à des travaux futurs.

Conclusion and perspectives

We have reported on a numerical investigation of the out-of-equilibrium dynamics of a dense polymer brush under flow, in which the brush is modeled as a collection of linear freely flexible chains grafted to a flat substrate. We have implemented a coarse-grained Dissipative Particle Dynamics (DPD) code with explicit solvent, where the coarse-grained DPD procedure have been applied both to solvent molecules and polymer monomers. Our approach classifies among the self-consistent model analysis, offering the possibility to (i) reproduce hydrodynamic interactions while retaining a detailed view of the brush dynamics on the scale of the coarse-grained monomers; (ii) access both the polymer dynamics, influenced by the imposed flow, and the flow field, perturbed by the presence and motion of the brush. Moreover, the election of such a mesoscopic model has allowed the inclusion in the system of a deformable object of cellular size. This case study has been guided by the aim to approach the endothelial glycocalyx layer and to reproduce external conditions resembling the microcirculatory system. The set-up of a macroscopic deformable object interacting with the polymer matrix, therefore, figures a red blood cell flowing in a microcapillary.

In the present thesis a big amount of data has been collected for the analysis of a dense polymer brush subdued to a simple liquid parabolic flow in a slit-pore geometry. Increasing the Weissenberg number (Wi) we have detected three ranges of imposed flow for which a velocity inversion appears at the interface between the brush and the rest of the channel. We have discovered a well-characterized surface traveling wave, which appears in all cases of backflow and it is not present in the other ones, providing a novel picture of the flow-inversion phenomenon, which is associated to a collective motion of the whole brush rather than to the single chain dynamics. We have also observed a striking and unexpected similarity in the relation between the wave velocity and the backflow velocity for the case of flow in passive polymer brushes and for the case

of active microswimmers. Indeed, both the Taylor swimmer propagation velocity and the backflow velocity can be viewed as the solution of a two dimensional Stokes flow with a propagating sinusoidal wave as boundary condition.

Aiming at quantifying the conditions under which the physical collective properties of the brush couple with the hydrodynamic properties of the solvent to produce flow inversion and thus the surface wave, we have characterized the brush as a continuous medium and provided an estimation of its elastic moduli. We have indicated a criterion for the onset of surface wave in the following condition:

$$\sigma_S \sim G \tag{4.7}$$

where σ_S is the shear stress exerted by the flow on the brush surface S and G is the brush shear modulus. Beyond such threshold, brush instabilities can take place and the wave forms. We stress the importance of G with respect to the brush Young modulus Y , since for polymer brushes the two moduli greatly differ ($Y/G \sim 10^2$), therefore instability is more easily induced by a resonance with shearing modes than with compressional modes. Interestingly, coming back to the physical reference system, the shear modulus of the endothelial glycocalyx layer has been measured to be $G = 6.7\text{Pa}$ and at physiological conditions shear stresses at the microcapillary walls are of the same order of magnitude (few pascals). Thus, the criterion condition of Eq.(4.7) can be fulfilled and the surface wave we have discovered might be displayed.

In our system, the aforementioned condition is fulfilled at the first Wi region of flow inversion, while the presence of different disconnected Wi windows in which the wave appears is maybe due to the strong nonlinearity that enters the dynamics at high Wi : the brush stiffens and its height decreases as function of the imposed flow.

We have also characterized bidisperse brushes and probed the backflow effect as function of the polydispersity index: $|v_{min}|$ decreases. Such result is reasonable, as in the vicinity of the brush interface (where the backflow is observed) an increase of the bidispersity goes in the same direction as a decrease of the grafting density. Since the backflow effect is definitely a collective phenomenon, it is expected to vanish if the distance between chains increases and the excluded volume interactions, which are determinant for the polymer recursive motion, become the more and more negligible.

Including a RBC in the channel and switching to cylindrical geome-

try, we have found that the cell velocity decreases on increasing the brush thickness. Also bidispersity can reduce the cell speed, while the cell shape keep constant as effect of a balance between the lower velocity and the stronger confinement induced by longer chains. Those findings indicate that the cell detects the polymer brush as basically a rigid thickening of the channel wall. The apparent contrast with respect to the on-off effect of the brush thickness on the cell velocity (reported from recent experiments [156] and discussed in Sect.5.2) could be ascribed to the limited range of polymerization degree n we have explored in the cylindrical geometry: the thickness of our brush corresponds, in physical units, to a much thicker layer ($\gtrsim 600$ nm) than the ones explored in Ref. [156]. In the next paragraph we will propose few alternative ways to overcome this problem.

It would be interesting, in addition, to investigate the effect of the surface wave on the red blood cell dynamics. We speculate that, if the brush surface modulation has effect on the cell surface, it might help in breaking red blood cell clusters, likely to create and stabilize at high but physiologically possible fibrinogen concentrations and known to reduce oxygen delivery [81]. Moreover, if the lock-in mechanism presented in Sect.6.3 does take place at the microcirculation level, it could serve as a control in establishing a blood velocity limit and avoiding too strong shear stresses.

In order to follow up on the hydrodynamic-driven interaction between polymer brush and RBCs and verify the aforementioned hypotheses, we propose the following novel approaches. A first test could be conducted regardless of microcirculation and physiological scales: with modifications to the parameter list and coming back to slit-pore geometry with polymers only at one wall, the code should be able to answer if a generic deformable object is actually influenced by the brush surface wave. Another idea is supplied by more refined multiscale models that exploit the so-called Adaptive Resolution technique [161]. With the development of more and more powerful computers, it is earning an increasing role in case the problem to be addressed involves several different scales: with opportune adjustments, the Adaptive Resolution technique allows a coarse-graining of different level in different regions of the simulated system. It would be worthwhile an attempt in which the cut-off radius r_c

for polymer-polymer interaction is fixed to a smaller value than the one for membrane vertices and membrane-solvent interactions. This modification would allow the simulation of longer chains in co-presence with the cell. Finally, a completely different method (for example, the Boundary Integral method [162]) would envisage the numerical solution of Stokes equation with cell embedded in and in which a boundary is a traveling wave or an elastic medium with low shear modulus. It would therefore be a continuum description, but with unusual boundary conditions set accordingly to the present thesis findings.

Conclusion et perspectives (french version)

On a rapporté une étude numérique de la dynamique hors de l'équilibre d'une brosse dense de polymères dans laquelle la brosse est modélisée en tant que collection de chaînes linéaires complètement flexibles et greffées sur un substrat plat. On a exploité une technique de coarse-graining qui s'appelle Dissipative Particle Dynamics (DPD), permettant d'avoir un solvant explicite. La procédure de coarse-graining de la DPD a été appliquée à la fois aux molécules de solvant et aux monomères. Notre approche classe parmi les modèles d'analyse auto-cohérents, offrant la possibilité (i) de reproduire les interactions hydrodynamiques en conservant une vue détaillée de la dynamique de la brosse à l'échelle des monomères coarse-grained; (ii) accéder à la fois à la dynamique du polymère, influencée par le débit imposé, et au champ de vitesse d'écoulement, perturbé par la présence et le mouvement de la brosse. De plus, l'élection d'un tel modèle mésoscopique a permis d'inclure dans le système un objet déformable de taille cellulaire. Cette étude a eu pour objectif d'approcher la physique de la couche de glycocalyx endothélial et de reproduire des conditions ressemblantes à celles du système micro-circulatoire. Elle se termine par la mise en place d'un objet déformable macroscopique interagissant avec la matrice de polymères et qui représente, donc, un globule rouge circulant dans un micro-capillaire.

Dans la présente thèse, une grande quantité de données a été recueillie pour l'analyse d'une brosse dense de polymères sous écoulement parabolique d'un liquide simple dans une géométrie *slit-pore*. En augmentant le nombre de Weissenberg (Wi), on a détecté trois régions de débit imposé pour lesquelles une inversion de vitesse apparaît à l'interface entre la brosse et le reste du canal. On a découvert une onde de surface qui peut être bien caractérisée et qui apparaît dans tous les cas d'inversion de flux et il n'est pas présent dans les autres. On a donc fourni une nouvelle image du phénomène d'inversion de flux, qui est associée à un mouvement collectif de la brosse entière plutôt qu'à la dynamique de la chaîne simple. On a également observé une similitude frappante et inattendue entre la brosse de polymères sous écoulement (au cas où l'inversion de flux est remarqué) et les micro-nageurs de Taylor. En effet, la vitesse de propagation du nageur de Taylor et la vitesse du flux inverse peuvent être considérées comme la solution d'un flux Stokes bidimensionnel avec une onde sinusoïdale se propageant comme condition aux limites.

Pour quantifier les conditions selon lesquelles la dynamique collective de la brosse se couple avec l'hydrodynamique du solvant pour produire

l'inversion de flux et donc l'onde de surface, on a caractérisé la brosse comme un milieu continu et on a fourni une estimation de ses modules élastiques. On a donc indiqué un critère pour l'apparition de l'onde de surface qui est le suivant:

$$\sigma_S \sim G \quad (6.3)$$

où σ_S est la contrainte de cisaillement exercée par l'écoulement sur la surface S de la brosse et G est le module de cisaillement de la brosse. Au-delà de ce seuil, des instabilités peuvent avoir lieu et les ondes se forment. Nous soulignons l'importance pour une brosse de G par rapport à son module de Young Y , puisque pour les brosses de polymères les deux modules diffèrent grandement ($Y/G \sim 10^2$), donc l'instabilité est plus facilement induite par une résonance avec les modes de cisaillement qu'avec les modes de compression. En plus, en rappelant le système physique de référence, le module de cisaillement de la couche de glycocalyx endothélial a été mesurée de $G = 6.7$ pascal et, aux conditions physiologiques, les contraintes de cisaillement aux parois des micro-capillaires sont du même ordre de grandeur (quelques pascals). Ainsi, la condition indiquée par l'équation susmentionnée peut être vérifiée et l'onde de surface qu'on a découverte pourrait être affichée.

Dans notre système, la condition susmentionnée est vérifiée à la première région de Wi qui montre l'inversion de flux, tandis que la présence de différentes fenêtres Wi déconnectées dans lesquelles l'onde apparaît est peut-être due à la forte non-linéarité qui joue un rôle dans la dynamique à haut Wi : la brosse se raidit et sa hauteur diminue en fonction du débit imposé.

On a également caractérisé des brosses bidispersées et sondé l'effet de flux inverse en fonction de l'indice de polydispersité: $|v_{min}|$ diminue. Ce résultat est raisonnable, puisque autour de l'interface de la brosse (où le flux s'inverse) une augmentation de la bidispersité va dans le même sens qu'une diminution de la densité de greffage. Puisque l'effet d'inversion du flux est définitivement un phénomène collectif, on s'attend à ce qu'il disparaisse si la distance entre les chaînes augmente et les interactions de volume exclus, qui sont déterminantes pour le mouvement récursif des polymères, deviennent de plus en plus négligeables.

Une fois inclus un globule rouge dans le canal et opérée la commutation à géométrie cylindrique, on a trouvé que la vitesse de la cellule diminue lorsqu'on augmente l'épaisseur de la brosse. La bidispersité peut également réduire la vitesse de la cellule, tandis que la forme de la cellule se maintient constante sous l'effet d'un bilan entre la vitesse plus basse

et le confinement plus fort induit par les chaînes les plus longues. Ces résultats indiquent que la cellule détecte la brosse de polymères fondamentalement comme un épaissement rigide de la paroi du canal. Le contraste apparent par rapport à des résultats récents [156] pourrait être attribuée à la gamme limitée de degré de polymérisation n qu'on a explorée dans la géométrie cylindrique: l'épaisseur de la brosse simulée correspond, en unités physiques, à une couche beaucoup plus épaisse (> 600 nm) que celles explorées dans la Référence citée. Dans le paragraphe suivant, nous proposons quelques alternatives pour surmonter ce problème.

Il serait intéressant, en plus, d'étudier l'effet de l'onde de surface sur la dynamique des globules rouges. Nous supposons que si la modulation de la surface de la brosse a un effet sur la forme et la vitesse de la cellule, elle pourrait contribuer à briser les grappes de globules rouges, susceptibles de se créer et de se stabiliser à des concentrations de fibrinogène élevées mais physiologiquement possibles et connu pour réduire l'apport d'oxygène [81]. De plus, si le mécanisme de *lock-in* présenté dans la section 6.3 se produit au niveau de la micro-circulation, il pourrait servir de contrôle pour établir une limite supérieure à la vitesse sanguine et éviter des contraintes de cisaillement trop fortes.

Afin de clarifier l'interaction hydrodynamique entre la brosse de polymères et les globules rouges et vérifier les hypothèses susmentionnées, nous proposons les nouvelles approches suivantes. Un premier test pourrait être effectué indépendamment des conditions et des échelles physiologiques de la micro-circulation: avec des modifications à la liste des paramètres et en revenant à la géométrie *slit-pore* avec des polymères greffés seulement à une paroi, on peut comprendre si un objet déformable générique est réellement influencé par l'onde de surface de la brosse. Une autre idée est fournie par des modèles multi-échelles qui exploitent la technique dite de *résolution adaptative* [161]. Avec le développement d'ordinateurs de plus en plus puissants, cette technique gagne un rôle croissant dans le cas où le problème à traiter implique plusieurs échelles différentes: avec des ajustements opportuns, la méthode de résolution adaptative permet un coarse-graining de niveaux différents dans différentes régions du système simulé. Il serait intéressant de déterminer la dynamique au cas où le rayon de *cut-off* r_c de l'interaction DPD polymère-polymère est fixé à une valeur inférieure que celle entre sommets de

membrane et entre membrane et solvant. Cette modification permettrait la simulation de chaînes plus longues en présence de la cellule. Enfin, une méthode complètement différente (par exemple, la Boundary Integral Method [162]) envisageait la solution numérique de l'équation de Stokes avec une cellule et pour laquelle une limite est une onde progressive ou un milieu élastique à faible module de cisaillement. Ce serait donc une description continue, mais avec des conditions aux limites conformes aux conclusions de la présente thèse.

Appendix A

The conservative force parameter

The conservative interaction parameter a_{SS} is related to density fluctuations of the system and it is calculated from the dimensionless isothermal compressibility κ_T^{-1} of the modeled liquid. The definition of isothermal compressibility is:

$$\kappa_T = -\frac{1}{V} \left. \frac{\partial V}{\partial P} \right|_T = \frac{1}{\rho} \left. \frac{\partial \rho}{\partial P} \right|_T \quad (\text{A.1})$$

with $\rho = N/V$ the number density. Its dimensionless form reads

$$\kappa_T^{-1} = \frac{1}{\rho k_B T} \frac{1}{\kappa_T} = \frac{1}{k_B T} \left. \frac{\partial P}{\partial \rho} \right|_T \quad (\text{A.2})$$

The equation of state to calculate the pressure P of the NVT system is, from the virial theorem:

$$\begin{aligned} P &= \rho k_B T + \frac{1}{3V} \left\langle \sum_{j>i} (\vec{r}_i - \vec{r}_j) \cdot \vec{F}_i \right\rangle = \\ &= \rho k_B T + \frac{1}{3V} \left\langle \sum_{j>i} (\vec{r}_i - \vec{r}_j) \cdot \vec{F}_i^C \right\rangle = \\ &= \rho k_B T + \frac{2\pi}{3} \rho^2 \int_0^{r_c} r F(r) g(r) r^2 dr \end{aligned} \quad (\text{A.3})$$

where we have used the equivalence $\sum_{j>i} = 1/2 \sum_{i,j \neq i}$ and the definition $\sum_{i,j \neq i} \delta(\mathbf{r} - \mathbf{r}_{ij})/V^2 = \rho^2 g(r)$ with $g(r)$ the radial distribution function for an isotropic system. The first term in the righthand side is the ideal gas contribution to the pressure. Previous simulation studies [109] have

brought to such heuristic expression:

$$P = \rho k_B T + \alpha a_{SS} \rho^2 r_c^4 \quad (\text{A.4})$$

with $\alpha = 0.101 \pm 0.001$. Such relations holds for high enough densities $\rho > 2$.

Therefore

$$\kappa_T^{-1} = \frac{1}{k_B T} (k_B T + 2\alpha a_{SS} r_c^4 \rho) = 1 + 0.2 \frac{a_{SS} r_c^4 \rho}{k_B T} \quad (\text{A.5})$$

Since at $T = 300K$ the compressibility of water is $\kappa_T^{-1} \approx 16$, the final relation $a_{SS} = 75 \frac{k_B T}{\rho r_c^4}$ is found.

Appendix B

Expressions for the RBC membrane forces

Membrane forces are calculated as $\vec{f}_i = -\partial V(\vec{r}_i)/\partial \vec{r}_i$. Instead of listing forces as acting on the generic point \vec{r}_i , it is more convenient to collect them separately as 2-, 3- and 4-point ones. For computational purposes, indeed, different loop cycles should be implemented, respectively running over links L_{ij} , triangles T_{ijk} and dihedrals D_{ijkl} .

2-point forces 2-point forces comprise the elastic interaction and the viscous interaction. For each L_{ij} we update forces on point i and j :

$$\begin{aligned} \vec{f}_i^{L_{ij}} &= -\frac{k_s}{1 - (r_{ij}/\ell_m)^2} \vec{r}_{ij} + \frac{k_p}{r_{ij}^2} \hat{r}_{ij} - \gamma^T \vec{v}_{ij} - \gamma^C (\vec{v}_{ij} \cdot \hat{r}_{ij}) \hat{r}_{ij} \\ &+ \sqrt{2k_B T} \left(\sqrt{2\gamma^T} \frac{d\bar{W}_{ij}^S}{dt} + \sqrt{3\gamma^C - \gamma^T} \frac{tr[dW_{ij}]}{3dt} \right) \hat{r}_{ij} \quad (\text{B.1}) \end{aligned}$$

Then, simply, $\vec{f}_i^{L_{ij}} = -\vec{f}_j^{L_{ij}}$.

3-point forces 3-point forces are derived from the global and local conserving area constraints and volume constraint. For each T_{ijk} we update the following point forces:

$$\vec{f}_i^{T_{ijk}} = -\alpha_t (\vec{\xi} \wedge \vec{a}_{kj}) - \beta_t (\vec{\xi} \wedge \vec{a}_{kj}) - \gamma_t \left(\frac{\vec{\xi}}{3} + \vec{t}_c \wedge \vec{a}_{kj} \right) \quad (\text{B.2a})$$

$$\vec{f}_j^{T_{ijk}} = -\alpha_t (\vec{\xi} \wedge \vec{a}_{ik}) - \beta_t (\vec{\xi} \wedge \vec{a}_{ik}) - \gamma_t \left(\frac{\vec{\xi}}{3} + \vec{t}_c \wedge \vec{a}_{ik} \right) \quad (\text{B.2b})$$

$$\vec{f}_k^{\mathcal{T}ijk} = -\alpha_t(\vec{\xi} \wedge \vec{a}_{ji}) - \beta_t(\vec{\xi} \wedge \vec{a}_{ji}) - \gamma_t \left(\frac{\vec{\xi}}{3} + \vec{t}_c \wedge \vec{a}_{ji} \right) \quad (\text{B.2c})$$

with the prefactors $\alpha_t = k_a(A - A_0^{tot})/(4A_t A_0^{tot})$, $\beta_t = k_d(A_t - A_0)/(4A_t A_0)$ and $\gamma_t = k_v(V - V_0^{tot})/(6V_0^{tot})$.

It is important to underline that, for forces calculation, triangle normal vectors must be all inwards or all outwards.

4-point forces The 4-point force is due to the bending energy. For each D_{ijkl} we update forces on points i , j , k and l . Let's consider a dihedral for which the common edge between triangles is \vec{a}_{jk} . The original work by Fedosov and coworkers yields [104, 116–118]:

$$\vec{f}_i^{\mathcal{D}ijkl} = b_{11}(\vec{\xi} \wedge \vec{a}_{kj}) + b_{12}(\vec{\zeta} \wedge \vec{a}_{kj}) \quad (\text{B.3a})$$

$$\vec{f}_j^{\mathcal{D}ijkl} = b_{11}(\vec{\xi} \wedge \vec{a}_{ik}) + b_{12}(\vec{\xi} \wedge \vec{a}_{kl} + \vec{\zeta} \wedge \vec{a}_{ik}) + b_{22}(\vec{\zeta} \wedge \vec{a}_{kl}) \quad (\text{B.3b})$$

$$\vec{f}_k^{\mathcal{D}ijkl} = b_{11}(\vec{\xi} \wedge \vec{a}_{ji}) + b_{12}(\vec{\xi} \wedge \vec{a}_{lj} + \vec{\zeta} \wedge \vec{a}_{ji}) + b_{22}(\vec{\zeta} \wedge \vec{a}_{lj}) \quad (\text{B.3c})$$

$$\vec{f}_l^{\mathcal{D}ijkl} = b_{12}(\vec{\xi} \wedge \vec{a}_{jk}) + b_{22}(\vec{\zeta} \wedge \vec{a}_{jk}) \quad (\text{B.3d})$$

with the definitions $b_{11} = -\beta_b \cos(\theta)/|\vec{\xi}|^2$, $b_{12} = \beta_b/(|\vec{\xi}||\vec{\zeta}|)$ and $b_{22} = -\beta_b \cos(\theta)/|\vec{\zeta}|^2$ with $\beta_b = k_b(\sin(\theta) \cos(\theta_0) - \cos(\theta) \sin(\theta_0))/\sqrt{1 - \cos^2(\theta)}$.

Differently, we derive those forces following [163], yielding simpler expressions. Indeed, according to the aforementioned method, calculation of the bending forces is done via the usual derivation employing the following chain rule:

$$\vec{F}_i = -\nabla_i V = -\frac{dV}{d\phi} \frac{d\phi}{d \cos(\phi)} \frac{\partial \cos(\phi)}{\partial \vec{r}_i} \quad (\text{B.4})$$

Such rule generates the terms $d\phi/d \cos(\phi) = -\sin^{-1}(\phi)$ that is a singularity in $\phi = 0, \pi$ and in neighborhood of these values produces big numerical errors. To avoid such numerical inefficiency we will use another chain rule:

$$\vec{F}_i = -\nabla_i V = -\frac{dV}{d\phi} \frac{\partial \phi}{\partial \vec{r}_i} \quad (\text{B.5})$$

Then, for each dihedral identified by vertices i, j, k, l with j, k in common between two triangles, we define

$$\vec{m} := \vec{r}_{ij} \wedge \vec{r}_{kj} \quad \text{and} \quad \vec{n} := \vec{r}_{kj} \wedge \vec{r}_{kl} \quad (\text{B.6})$$

such that

$$\cos(\theta) = \frac{\vec{m} \cdot \vec{n}}{|\vec{m}||\vec{n}|} \quad (\text{B.7})$$

Its sign is equivalent to that of $\mathbf{r}_{ij} \cdot \mathbf{n}$. The four forces are

$$\vec{f}_i = -\frac{dV(\theta)}{d\theta} r_{kj} \frac{\vec{m}}{|\vec{m}|^2} \quad (\text{B.8a})$$

$$\vec{f}_l = \frac{dV(\theta)}{d\theta} r_{kj} \frac{\vec{n}}{|\vec{n}|^2} \quad (\text{B.8b})$$

$$\vec{f}_j = -\vec{f}_i + \vec{S} \quad (\text{B.8c})$$

$$\vec{f}_k = -\vec{f}_l - \vec{S} \quad (\text{B.8d})$$

where $\vec{S} = 1/r_{jk}^2 [f_i(\vec{r}_{ij} \cdot \vec{r}_{kj}) - f_l(\vec{r}_{kl} \cdot \vec{r}_{kj})]$. The two last one exploiting the translational invariance of the potential Eq.(2.23), i. e. $\vec{f}_i + \vec{f}_j + \vec{f}_k + \vec{f}_l = 0$. In our case, Eq.(2.23), $dV(\theta)/d\theta = k_t \sin(\theta - \theta_0)$.

Appendix C

Membrane boundary conditions

A solvent particle can cross the membrane through any of the triangles constituting the tessellation. Let's indicate the solvent particle position with $\vec{p}(t)$ and the triangle vertex positions with $\vec{s}_i(t)$, $i = 1, 2, 3$. We define the quantity $b(t) = \vec{\xi}(t) \cdot (\vec{p}(t) - \vec{s}_1(t))$, where $\vec{\xi}$ is the triangle normal vector defined in Sect. (2.4.2), and check for the product $b(0)b(\Delta t)$. If $b(0)b(\Delta t) \leq 0$ it means that, during the time step, the particle has crossed the plane of normal $\vec{\xi}$ and containing the membrane point \vec{s}_1 . The collision time t' is found by solving the equation $\vec{\xi}(t) \cdot (\vec{p}(t) - \vec{s}_1(t)) = 0$. Since it is a cubic expression in t , the Newton-Raphson method is used. To be sure that the collision with the plane is actually a collision with the limited part of the plane constituting the triangle, a further condition has to be verified. Indicating with prime quantities calculated at the collision time t' , we define a vector $\vec{g}' = \vec{p}' - \vec{s}_1'$ and write it as linear combination of the \vec{a}'_{ij} : $\vec{g}' = \alpha \vec{a}'_{21} + \beta \vec{a}'_{31}$. Thus, $\alpha = [(\vec{g}' \cdot \vec{a}'_{21})|\vec{a}'_{31}|^2 - (\vec{g}' \cdot \vec{a}'_{31})(\vec{a}'_{21} \cdot \vec{a}'_{31})]/[|\vec{a}'_{21}|^2|\vec{a}'_{31}|^2 - (\vec{a}'_{21} \cdot \vec{a}'_{31})^2]$ and, analogously, $\beta = [(\vec{g}' \cdot \vec{a}'_{31})|\vec{a}'_{21}|^2 - (\vec{g}' \cdot \vec{a}'_{21})(\vec{a}'_{21} \cdot \vec{a}'_{31})]/[|\vec{a}'_{21}|^2|\vec{a}'_{31}|^2 - (\vec{a}'_{21} \cdot \vec{a}'_{31})^2]$. Therefore, collision with the membrane triangle occurs if also the following conditions are verified: $\alpha \geq 0$, $\beta \geq 0$ and $\alpha + \beta \leq 1$. In this case, new position and velocity for the particle are calculated:

$$\begin{cases} \vec{v}_p^{new} = 2\vec{v}' - \vec{v}_p & \text{where } \vec{v}' = (1 - \alpha - \beta)\vec{v}_1 + \alpha\vec{v}_2 + \beta\vec{v}_3 \\ \vec{p}^{new} = \vec{p}' + (\Delta t - t')\vec{v}_p^{new} & \text{where } \vec{p}' = \vec{p}_0 + \vec{v}_p t' \end{cases}$$

The mechanism does not conserve momentum.

Such algorithm should be repeated to have control also on possible

multiple collisions. At the same time, it is useful to create a neighboring list to avoid time-consuming collision-checking loops on *all* the solvent particles with *all* the membrane triangles.

Bibliography

- [1] P. Pincus, “Colloid stabilization with grafted polyelectrolytes,” *Macromolecules*, vol. 24, no. 10, pp. 2912–2919, 1991.
- [2] F. Lo Verso, S. A. Egorov, A. Milchev, and K. Binder, “Spherical polymer brushes under good solvent conditions: Molecular dynamics results compared to density functional theory,” *The Journal of Chemical Physics*, vol. 133, no. 18, p. 184901, 2010.
- [3] B. Jaquet, D. Wei, B. Reck, F. Reinhold, X. Zhang, H. Wu, and M. Morbidelli, “Stabilization of polymer colloid dispersions with pH-sensitive poly-acrylic acid brushes,” *Colloid and Polymer Science*, vol. 291, no. 7, pp. 1659–1667, 2013.
- [4] M. Kobayashi, H. Tanaka, M. Minn, J. Sugimura, and A. Takahara, “Interferometry study of aqueous lubrication on the surface of polyelectrolyte brush,” *ACS Appl. Mater. Interfaces*, vol. 6, no. 22, pp. 20365–20371, 2014.
- [5] J. Klein, E. Kumacheva, D. Mahalu, D. Perahia, and L. Fetters, “Reduction of frictional forces between solid surfaces bearing polymer brushes,” *Nature*, vol. 370, pp. 634–636, 1994.
- [6] M. Chen, W. Briscoe, S. Armes, and J. Klein, “Lubrication by biomimetic surface layers at physiological pressures,” *Science*, vol. 323, pp. 1698–1701, 2009.
- [7] S. N. Ramakrishna, R. M. Espinosa-Marzal, V. V. Naik, P. C. Nalam, and N. D. Spencer, “Adhesion and friction properties of polymer brushes on rough surfaces: A gradient approach,” *Langmuir*, vol. 29, no. 49, pp. 15251–15259, 2013.
- [8] L. Landherr, C. Cohen, P. Agarwal, and L. Archer, “Interfacial friction and adhesion of polymer brushes,” *Langmuir*, vol. 27, no. 15, pp. 9387–9395, 2011.

- [9] E. P. Schmidt, Y. Yang, W. J. Janssen, A. Gandjeva, M. J. Perez, L. Barthel, R. L. Zemans, J. C. Bowman, D. E. Koyanagi, Z. X. Yunt, L. P. Smith, S. S. Cheng, K. H. Overdier, K. R. Thompson, M. W. Geraci, I. S. Douglas, D. B. Pearse, and R. M. Tudor, “The pulmonary endothelial glycocalyx regulates neutrophil adhesion and lung injury during experimental sepsis,” *Nat Med*, vol. 18, no. 8, pp. 1217–1223, 2012.
- [10] C. Murphy and V. Turner, “Glycocalyx carbohydrates of uterine epithelial cells increase during early pregnancy in the rat,” *Journal of Anatomy*, vol. 17, pp. 109–115, 1991.
- [11] B. Button, L.-H. Cai, C. Ehre, M. Kesimer, D. B. Hill, J. K. Sheehan, R. C. Boucher, and M. Rubinstein, “A periciliary brush promotes the lung health by separating the mucus layer from airway epithelia,” *Science*, vol. 337, no. 6097, pp. 937–941, 2012.
- [12] J. H. Luft, “Fine structures of capillary and endocapillary layer as revealed by ruthenium red,” *Federation proceedings*, vol. 25, no. 6, pp. 1773–83, 1966.
- [13] L. N. Broekhuizen, H. L. Mooij, J. J. Kastelein, E. S. Stroes, H. Vink, and M. Nieuwdorp, “Endothelial glycocalyx as potential diagnostic and therapeutic target in cardiovascular disease,” *Current opinion in lipidology*, vol. 20, no. 1, pp. 57–62, 2009.
- [14] S. Weinbaum, J. M. Tarbell, and E. R. Damiano, “The structure and function of the endothelial glycocalyx layer,” *Annual Review of Biomedical Engineering*, vol. 9, pp. 121–167, 2007.
- [15] S. T. Milner, T. A. Witten, and M. E. Cates, “A parabolic density profile for grafted polymers,” *EPL (Europhysics Letters)*, vol. 5, p. 413, Mar. 1988.
- [16] S. T. Milner, “Polymer Brushes,” *Science*, vol. 251, pp. 905–914, 1991.
- [17] M. J. A. Hore, J. Ford, K. Ohno, R. J. Composto, and B. Hammouda, “Direct measurements of polymer brush conformation using small-angle neutron scattering (sans) from highly grafted iron oxide nanoparticles in homopolymer melts,” *Macromolecules*, vol. 46, no. 23, pp. 9341–9348, 2013.

- [18] E. Currie, M. Wagemaker, M. C. Stuart, and A. Van Well, "Structure of grafted polymers, investigated with neutron reflectometry," *Physica B: Condensed Matter*, vol. 283, no. 1, pp. 17–21, 2000.
- [19] D. I. Dimitrov, A. Milchev, and K. Binder, "Polymer brushes in solvents of variable quality: molecular dynamics simulations using explicit solvent," *The Journal of chemical physics*, vol. 127, no. 8, p. 084905, 2007.
- [20] K. Binder, *Monte Carlo and molecular dynamics simulations in polymer science*. Oxford University Press, 1995.
- [21] J. L. Barrat, "A possible mechanism for swelling of polymer brushes under shear," *Macromolecules*, vol. 25, no. 2, pp. 832–834, 1992.
- [22] P.-Y. Lai and C.-Y. Lai, "Polymer brush under strong shear," *Physical Review E*, vol. 54, no. 6, p. 6958, 1996.
- [23] Y. Rabin and S. Alexander, "Stretching of grafted polymer layers," *EPL (Europhysics Letters)*, vol. 13, no. 1, p. 49, 1990.
- [24] J. Klein, D. Perahia, and S. Warburg, "Forces between polymer-bearing surfaces undergoing shear," *Nature*, vol. 352, no. 6331, pp. 143–145, 1991.
- [25] J. F. Danielli, "Capillary permeability and oedema in the perfused frog," *The Journal of Physiology*, vol. 98, no. 1, pp. 109–129, 1940.
- [26] S. P. Drummond, "The vascularity of the brain of the hibernating frog and its relation to function," *The Journal of Comparative Neurology*, vol. 82, no. 1, pp. 1–18, 1945.
- [27] E. M. Landis, "Capillary permeability and the factors affecting the composition of capillary filtrate," *Annals of the New York Academy of Sciences*, vol. 46, no. 8, pp. 713–731, 1946.
- [28] R. Chambers and B. W. Zweifach, "Intercellular cement and capillary permeability," *Physiological Reviews*, vol. 27, no. 3, pp. 436–463, 1947.
- [29] B. Klitzman and B. R. Duling, "Microvascular hematocrit and red cell flow in resting and contracting striated muscle," *American Journal of Physiology - Heart and Circulatory Physiology*, vol. 237, no. 4, pp. H481–H490, 1979.

- [30] C. Desjardins and B. R. Duling, "Heparinase treatment suggests a role for the endothelial cell glycocalyx in regulation of capillary hematocrit," *American Journal of Physiology - Heart and Circulatory Physiology*, vol. 258, no. 3, pp. H647–H654, 1990.
- [31] A. R. Pries, T. W. Secomb, T. Gessner, M. B. Sperandio, J. F. Gross, and P. Gaehtgens, "Resistance to blood flow in microvessels in vivo," *Circulation Research*, vol. 75, pp. 904–915, 11 1994.
- [32] H. Vink and B. R. Duling, "Identification of distinct luminal domains for macromolecules, erythrocytes, and leukocytes within mammalian capillaries," *Circulation Research*, vol. 79, no. 3, pp. 581–589, 1996.
- [33] H. S. Bennett, "Morphological aspects of extracellular polysaccharides," *Journal of histochemistry & cytochemistry*, vol. 11, no. 1, pp. 14–23, 1963.
- [34] J. W. VanTeeffelen, J. Brands, E. S. Stroes, and H. Vink, "Endothelial glycocalyx: sweet shield of blood vessels," *Trends in cardiovascular medicine*, vol. 17, no. 3, pp. 101–105, 2007.
- [35] J. Rostgaard and K. Qvortrup, "Electron microscopic demonstrations of filamentous molecular sieve plugs in capillary fenestrae," *Microvascular Research*, vol. 53, no. 1, pp. 1 – 13, 1997.
- [36] B. M. van den Berg, H. Vink, and J. A. Spaan, "The endothelial glycocalyx protects against myocardial edema," *Circulation Research*, vol. 92, no. 6, pp. 592–594, 2003.
- [37] B. Fu and J. Tarbell, "Mechano-sensing and transduction by endothelial surface glycocalyx: composition, structure, and function," *Wiley Interdiscip Rev Syst Biol Med*, vol. 5, pp. 381–390, 2013.
- [38] M. Nieuwdorp, M. C. Meuwese, H. Vink, J. B. Hoekstra, J. J. Kastelein, and E. S. Stroes, "The endothelial glycocalyx: a potential barrier between health and vascular disease," *Current opinion in lipidology*, vol. 16, no. 5, pp. 507–511, 2005.
- [39] M. Nieuwdorp, H. L. Mooij, J. Kroon, B. Atasever, J. A. Spaan, C. Ince, F. Holleman, M. Diamant, R. J. Heine, J. B. Hoekstra, *et al.*, "Endothelial glycocalyx damage coincides with microalbuminuria in type 1 diabetes," *Diabetes*, vol. 55, no. 4, pp. 1127–1132, 2006.

- [40] C. Alphonsus and R. Rodseth, “The endothelial glycocalyx: a review of the vascular barrier,” *Anaesthesia*, vol. 69, no. 7, pp. 777–784, 2014.
- [41] K. P. Arkill, C. R. Neal, J. M. Mantell, C. C. Michel, K. Qvortrup, J. Rostgaard, D. O. Bates, C. Knupp, and J. M. Squire, “3d reconstruction of the glycocalyx structure in mammalian capillaries using electron tomography,” *Microcirculation*, vol. 19, no. 4, pp. 343–351, 2012.
- [42] L. Lanotte, S. Guido, C. Misbah, P. Peyla, and L. Bureau, “Flow reduction in microchannels coated with a polymer brush,” *Langmuir*, vol. 28, no. 38, pp. 13758–13764, 2012.
- [43] W. C. Aird, “Phenotypic heterogeneity of the endothelium i. structure, function, and mechanisms,” *Circulation research*, vol. 100, no. 2, pp. 158–173, 2007.
- [44] M. C. L. G. Gouverneur, *Fluid shear stress directly stimulates synthesis of the endothelial glycocalyx: perturbations by hyperglycemia*. PhD thesis, 2006.
- [45] S. Reitsma, D. Slaaf, H. Vink, M. van Zandvoort, and M. oude Egbrink, “The endothelial glycocalyx: composition, functions, and visualization,” *Pflugers Arch.*, vol. 454, 2007.
- [46] J. B. Williams, “Comparative physiology of the vertebrate kidney,” *BioScience*, vol. 39, no. 9, pp. 652–654, 1989.
- [47] P. F. Davies, “Flow-mediated endothelial mechanotransduction,” *Physiological reviews*, vol. 75, no. 3, pp. 519–560, 1995.
- [48] B. L. Langille and S. L. Adamson, “Relationship between blood flow direction and endothelial cell orientation at arterial branch sites in rabbits and mice,” *Circulation Research*, vol. 48, no. 4, pp. 481–488, 1981.
- [49] R. M. Nerem, M. J. Levesque, and J. Cornhill, “Vascular endothelial morphology as an indicator of the pattern of blood flow,” *Journal of biomechanical engineering*, vol. 103, no. 3, pp. 172–176, 1981.
- [50] G. M. Rubanyi, J. C. Romero, and P. M. Vanhoutte, “Flow-induced release of endothelium-derived relaxing factor,” *American Journal*

- of Physiology-Heart and Circulatory Physiology*, vol. 250, no. 6, pp. H1145–H1149, 1986.
- [51] M. Gouverneur, J. A. Spaan, H. Pannekoek, R. D. Fontijn, and H. Vink, “Fluid shear stress stimulates incorporation of hyaluronan into endothelial cell glycocalyx,” *American Journal of Physiology-Heart and Circulatory Physiology*, vol. 290, no. 1, pp. H458–H452, 2006.
- [52] A. I. Barakat and D. K. Lieu, “Differential responsiveness of vascular endothelial cells to different types of fluid mechanical shear stress,” *Cell biochemistry and biophysics*, vol. 38, no. 3, pp. 323–343, 2003.
- [53] B. Mazzag and A. I. Barakat, “The effect of noisy flow on endothelial cell mechanotransduction: A computational study,” *Annals of Biomedical Engineering*, vol. 39, no. 2, pp. 911–921, 2010.
- [54] Y. C. Fung, *Biomechanics: circulation*. Springer Science & Business Media, 2013.
- [55] A. I. Barakat, “Blood flow and arterial endothelial dysfunction: mechanisms and implications,” *Comptes Rendus Physique*, vol. 14, no. 6, pp. 479–496, 2013.
- [56] G. Stoll and M. Bendszus, “Inflammation and atherosclerosis: Novel insights into plaque formation and destabilization,” *Stroke*, vol. 37, no. 7, pp. 1923–1932, 2006.
- [57] H. Vink, A. A. Constantinescu, and J. A. Spaan, “Oxidized lipoproteins degrade the endothelial surface layer implications for platelet-endothelial cell adhesion,” *Circulation*, vol. 101, no. 13, pp. 1500–1502, 2000.
- [58] C. Michel, “Starling: the formulation of his hypothesis of microvascular fluid exchange and its significance after 100 years,” *Experimental Physiology*, vol. 82, no. 1, pp. 1–30, 1997.
- [59] S. Weinbaum, “1997 whitaker distinguished lecture: Models to solve mysteries in biomechanics at the cellular level; a new view of fiber matrix layers,” *Annals of Biomedical Engineering*, vol. 26, no. 4, pp. 627–643.

- [60] A. H. Salmon and S. C. Satchell, “Endothelial glycocalyx dysfunction in disease: albuminuria and increased microvascular permeability,” *The Journal of Pathology*, vol. 226, no. 4, pp. 562–574, 2012.
- [61] <http://www.easynotecards.com/>.
- [62] S. Guido and G. Tomaiuolo, “Microconfined flow behavior of red blood cells in vitro,” *Comptes Rendus Physique*, vol. 10, no. 8, pp. 751–763, 2009.
- [63] S. Chien, “Red cell deformability and its relevance to blood flow,” *Annual review of physiology*, vol. 49, no. 1, pp. 177–192, 1987.
- [64] E. Evans and R. Hochmuth, “Membrane viscoelasticity,” *Biophysical Journal*, vol. 16, no. 1, pp. 1–11, 1976.
- [65] R. Waugh and E. Evans, “Thermoelasticity of red blood cell membrane,” *Biophysical journal*, vol. 26, no. 1, p. 115, 1979.
- [66] E. A. Evans, “Bending elastic modulus of red blood cell membrane derived from buckling instability in micropipet aspiration tests,” *Biophysical Journal*, vol. 43, no. 1, p. 27, 1983.
- [67] J. Mills, L. Qie, M. Dao, C. Lim, and S. Suresh, “Nonlinear elastic and viscoelastic deformation of the human red blood cell with optical tweezers,” *MCB-TECH Science Press*, vol. 1, pp. 169–180, 2004.
- [68] E. W. Merrill, “Rheology of blood,” *Physiol. Rev*, vol. 49, no. 4, pp. 863–888, 1969.
- [69] R. Fåhræus and T. Lindqvist, “The viscosity of the blood in narrow capillary tubes,” *American Journal of Physiology–Legacy Content*, vol. 96, no. 3, pp. 562–568, 1931.
- [70] S. Chien, “Shear dependence of effective cell volume as a determinant of blood viscosity,” *Science*, vol. 168, no. 3934, pp. 977–979, 1970.
- [71] A. Pries, D. Neuhaus, and P. Gaehtgens, “Blood viscosity in tube flow: dependence on diameter and hematocrit,” *American Journal of Physiology–Heart and Circulatory Physiology*, vol. 263, no. 6, pp. H1770–H1778, 1992.

- [72] T. M. Fischer, M. Stohr-Lissen, and H. Schmid-Schonbein, “The red cell as a fluid droplet: tank tread-like motion of the human erythrocyte membrane in shear flow,” *Science*, vol. 202, no. 4370, pp. 894–896, 1978.
- [73] M. Abkarian and A. Viallat, “Vesicles and red blood cells in shear flow,” *Soft Matter*, vol. 4, no. 4, pp. 653–657, 2008.
- [74] C. Misbah, “Vacillating breathing and tumbling of vesicles under shear flow,” *Physical review letters*, vol. 96, no. 2, p. 028104, 2006.
- [75] Y. Sui, Y. Chew, P. Roy, Y. Cheng, and H. Low, “Dynamic motion of red blood cells in simple shear flow,” *Physics of Fluids (1994-present)*, vol. 20, no. 11, p. 112106, 2008.
- [76] V. Lebedev, K. Turitsyn, and S. Vergeles, “Nearly spherical vesicles in an external flow,” *New journal of Physics*, vol. 10, no. 4, p. 043044, 2008.
- [77] D. Cordasco and P. Bagchi, “Orbital drift of capsules and red blood cells in shear flow,” *Physics of Fluids (1994-present)*, vol. 25, no. 9, p. 091902, 2013.
- [78] A. Z. K. Yazdani and P. Bagchi, “Phase diagram and breathing dynamics of a single red blood cell and a biconcave capsule in dilute shear flow,” *Phys. Rev. E*, vol. 84, p. 026314, Aug 2011.
- [79] X. Grandchamp, G. Coupier, A. Srivastav, C. Minetti, and T. Podgorski, “Lift and down-gradient shear-induced diffusion in red blood cell suspensions,” *Physical review letters*, vol. 110, no. 10, p. 108101, 2013.
- [80] P. Steffen, C. Verdier, and C. Wagner, “Quantification of depletion-induced adhesion of red blood cells,” *Phys. Rev. Lett.*, vol. 110, p. 018102, Jan 2013.
- [81] M. Brust, O. Aouane, M. Thiébaud, D. Flormann, C. Verdier, L. Kaestner, M. Laschke, H. Selmi, A. Benyoussef, T. Podgorski, *et al.*, “The plasma protein fibrinogen stabilizes clusters of red blood cells in microcapillary flows,” *Scientific reports*, vol. 4, 2014.
- [82] E. Damiano, B. Duling, K. Ley, and T. Skalak, “Axisymmetric pressure-driven flow of rigid pellets through a cylindrical tube lined

- with a deformable porous wall layer,” *Journal of Fluid Mechanics*, vol. 314, pp. 163–189, 1996.
- [83] S. Weinbaum, X. Zhang, Y. Han, H. Vink, and S. C. Cowin, “Mechanotransduction and flow across the endothelial glycocalyx,” *Proceedings of the National Academy of Sciences*, vol. 100, no. 13, pp. 7988–7995, 2003.
- [84] Y. Han, S. Weinbaum, J. A. Spaan, and H. Vink, “Large-deformation analysis of the elastic recoil of fibre layers in a brinkman medium with application to the endothelial glycocalyx,” *Journal of Fluid Mechanics*, vol. 554, pp. 217–235, 2006.
- [85] A. Vink, G. Warnier, F. Brombacher, and J.-C. Renaud, “Interleukin 9-induced in vivo expansion of the b-1 lymphocyte population,” *The Journal of experimental medicine*, vol. 189, no. 9, pp. 1413–1423, 1999.
- [86] M. Deng, X. Li, H. Liang, B. Caswell, and G. E. Karniadakis, “Simulation and modelling of slip flow over surfaces grafted with polymer brushes and glycocalyx fibres,” *Journal of Fluid Mechanics*, vol. 711, pp. 192–211, Sept. 2012.
- [87] T. W. Secomb, R. Hsu, and A. Pries, “A model for red blood cell motion in glycocalyx-lined capillaries,” *American Journal of Physiology-Heart and Circulatory Physiology*, vol. 274, no. 3, pp. H1016–H1022, 1998.
- [88] E. R. Damiano and T. M. Stace, “A mechano-electrochemical model of radial deformation of the capillary glycocalyx,” *Biophysical journal*, vol. 82, no. 3, pp. 1153–1175, 2002.
- [89] M. L. Smith, D. S. Long, E. R. Damiano, and K. Ley, “Near-wall μ -piv reveals a hydrodynamically relevant endothelial surface layer in venules in vivo,” *Biophysical journal*, vol. 85, no. 1, pp. 637–645, 2003.
- [90] E. Damiano, D. Long, and M. Smith, “Estimation of viscosity profiles using velocimetry data from parallel flows of linearly viscous fluids: application to microvascular haemodynamics,” *Journal of Fluid Mechanics*, vol. 512, pp. 1–19, 2004.

- [91] M. Müller and C. Pastorino, “Cyclic motion and inversion of surface flow direction in a dense polymer brush under shear,” *EPL (Europhysics Letters)*, vol. 81, no. 2, p. 28002, 2008.
- [92] F. Léonforte, J. Servantie, C. Pastorino, and M. Müller, “Molecular transport and flow past hard and soft surfaces: computer simulation of model systems,” *Journal of Physics Condensed Matter*, vol. 23, p. 184105, May 2011.
- [93] De Gennes, P.G., “Scaling theory of polymer adsorption,” *J. Phys. France*, vol. 37, no. 12, pp. 1445–1452, 1976.
- [94] P. G. de Gennes, “Conformations of polymers attached to an interface,” *Macromolecules*, vol. 13, no. 5, pp. 1069–1075, 1980.
- [95] P. Español, “Hydrodynamics from dissipative particle dynamics,” *Phys. Rev. E*, vol. 52, pp. 1734–1742, Aug 1995.
- [96] W. Pan, I. Pivkin, and G. Karniadakis, “Single-particle hydrodynamics in dpd: A new formulation,” *EPL (Europhysics Letters)*, vol. 84, no. 1, p. 10012, 2008.
- [97] N. Spenley, “Scaling laws for polymers in dissipative particle dynamics,” *EPL (Europhysics Letters)*, vol. 49, no. 4, p. 534, 2000.
- [98] R. D. Groot and T. J. Madden, “Dynamic simulation of diblock copolymer microphase separation,” *The Journal of chemical physics*, vol. 108, no. 20, pp. 8713–8724, 1998.
- [99] R. D. Groot, “Mesoscopic simulation of polymer-surfactant aggregation,” *Langmuir*, vol. 16, no. 19, pp. 7493–7502, 2000.
- [100] S. Jury, P. Bladon, M. Cates, S. Krishna, M. Hagen, N. Ruddock, and P. Warren, “Simulation of amphiphilic mesophases using dissipative particle dynamics,” *Physical Chemistry Chemical Physics*, vol. 1, no. 9, pp. 2051–2056, 1999.
- [101] R. D. Groot, “Electrostatic interactions in dissipative particle dynamicssimulation of polyelectrolytes and anionic surfactants,” *The Journal of chemical physics*, vol. 118, no. 24, pp. 11265–11277, 2003.
- [102] J. B. Avalos and A. Mackie, “Dissipative particle dynamics with energy conservation,” *EPL (Europhysics Letters)*, vol. 40, no. 2, p. 141, 1997.

- [103] R. D. Groot and K. Rabone, “Mesoscopic simulation of cell membrane damage, morphology change and rupture by nonionic surfactants,” *Biophysical journal*, vol. 81, no. 2, pp. 725–736, 2001.
- [104] D. A. Fedosov, *Multiscale modeling of blood flow and soft matter*. PhD thesis, 2010.
- [105] D. Frenkel and B. Smit, *Understanding Molecular Simulation: From Algorithms to Applications*. Computational science series, Elsevier Science, 2001.
- [106] P. Hoogerbrugge and J. M. V. A. Koelman, “Simulating Microscopic Hydrodynamic Phenomena with Dissipative Particle Dynamics,” *Europhysics Letters*, vol. 19, p. 155, 1992.
- [107] B. M. Forrest and U. W. Suter, “Accelerated equilibration of polymer melts by time-coarse-graining,” *The Journal of Chemical Physics*, vol. 102, no. 18, p. 7256, 1995.
- [108] V. Simeonidis, G. E. Karniadakis, and B. Caswell, “Schmidt number effects in dissipative particle dynamics simulation of polymers,” *The Journal of chemical physics*, vol. 125, p. 184902, Nov. 2006.
- [109] R. D. Groot and P. B. Warren, “Dissipative particle dynamics: Bridging the gap between atomistic and mesoscopic simulation,” *The Journal of Chemical Physics*, vol. 107, no. 11, p. 4423, 1997.
- [110] P. Español and P. B. Warren, “Statistical Mechanics of Dissipative Particle Dynamics,” *Europhysics Letters*, vol. 30, p. 191, 1995.
- [111] G. S. Grest and K. Kremer, “Molecular dynamics simulation for polymers in the presence of a heat bath,” *Physical Review A*, vol. 33, pp. 3628–3631, May 1986.
- [112] A. G. Goicochea, E. Mayoral, J. Klapp, and C. Pastorino, “Nanotribology of biopolymer brushes in aqueous solution using dissipative particle dynamics simulations: an application to peg covered liposomes in a theta solvent,” *Soft Matter*, vol. 10, pp. 166–174, 2014.
- [113] I. V. Pivkin and G. E. Karniadakis, “A new method to impose no-slip boundary conditions in dissipative particle dynamics,” *Journal of Computational Physics*, vol. 207, pp. 114–128, July 2005.

- [114] M. Revenga, I. Zúñiga, and P. Español, “Boundary conditions in dissipative particle dynamics,” *Computer Physics Communications*, vol. 121-122, pp. 309–311, Sept. 1999.
- [115] M. Karttunen, I. Vattulainen, and A. Lukkarinen, *Novel methods in soft matter simulations*, vol. 640. Springer Science & Business Media, 2004.
- [116] I. V. Pivkin and G. E. Karniadakis, “Accurate coarse-grained modeling of red blood cells,” *Physical review letters*, vol. 101, no. 11, p. 118105, 2008.
- [117] D. A. Fedosov, B. Caswell, and G. E. Karniadakis, “Systematic coarse-graining of spectrin-level red blood cell models,” *Computer methods in applied mechanics and engineering*, vol. 199, no. 29, pp. 1937–1948, 2010.
- [118] D. A. Fedosov, B. Caswell, and G. E. Karniadakis, “A multiscale red blood cell model with accurate mechanics, rheology, and dynamics,” *Biophysical journal*, vol. 98, no. 10, pp. 2215–2225, 2010.
- [119] G. Li, R. Zhu, and Y. Yang, “Polymer solar cells,” *Nature Photonics*, vol. 6, no. 3, pp. 153–161, 2012.
- [120] C. W. Hsu, F. Sciortino, and F. W. Starr, “Theoretical description of a dna-linked nanoparticle self-assembly,” *Phys. Rev. Lett.*, vol. 105, p. 055502, Jul 2010.
- [121] L. Rovigatti, F. Smallenburg, F. Romano, and F. Sciortino, “Gels of dna nanostars never crystallize,” *ACS nano*, vol. 8, no. 4, pp. 3567–3574, 2014.
- [122] L. Rovigatti, F. Bomboi, and F. Sciortino, “Accurate phase diagram of tetravalent dna nanostars,” *The Journal of Chemical Physics*, vol. 140, no. 15, p. 154903, 2014.
- [123] P. E. Rouse Jr, “A theory of the linear viscoelastic properties of dilute solutions of coiling polymers,” *The Journal of Chemical Physics*, vol. 21, no. 7, pp. 1272–1280, 1953.
- [124] K. Binder, T. Kreer, and A. Milchev, “Polymer brushes under flow and in other out-of-equilibrium conditions,” *Soft Matter*, vol. 7, no. 16, p. 7159, 2011.

- [125] C. Pastorino, K. Binder, T. Kreer, and M. Müller, “Static and dynamic properties of the interface between a polymer brush and a melt of identical chains,” *The Journal of Chemical Physics*, vol. 124, no. 6, 2006.
- [126] S. Alexander, “Adsorption of chain molecules with a polar head a scaling description,” *Journal De Physique*, vol. 38, no. 8, pp. 983–987, 1977.
- [127] S. Brinkers, H. R. Dietrich, F. H. de Groote, I. T. Young, and B. Rieger, “The persistence length of double stranded dna determined using dark field tethered particle motion,” *The Journal of chemical physics*, vol. 130, no. 21, p. 215105, 2009.
- [128] S. T. Milner, T. A. Witten, and M. E. Cates, “Effects of polydispersity in the end-grafted polymer brush,” *Macromolecules*, vol. 22, no. 2, pp. 853–861, 1989.
- [129] W. M. de Vos and F. A. M. Leermakers, “Modeling the structure of a polydisperse polymer brush,” *Polymer*, vol. 50, no. 1, pp. 305–316, 2009.
- [130] S. M. Balko, T. Kreer, P. J. Costanzo, T. E. Patten, A. Johner, T. L. Kuhl, and C. M. Marques, “Polymer brushes under high load,” *PloS one*, vol. 8, no. 3, p. e58392, 2013.
- [131] T. W. Secomb, R. Hsu, and A. R. Pries, “Motion of red blood cells in a capillary with an endothelial surface layer: effect of flow velocity,” *American Journal of Physiology - Heart and Circulatory Physiology*, vol. 281, no. 2, pp. H629–H636, 2001.
- [132] G. Taylor, “Analysis of the swimming of microscopic organisms,” *Proceedings of the Royal Society of London. Series A. Mathematical and Physical Sciences*, vol. 209, no. 1099, pp. 447–461, 1951.
- [133] D. Das and S. Sabhapandit, “Accurate statistics of a flexible polymer chain in shear flow,” *Phys. Rev. Lett.*, vol. 101, p. 188301, Oct 2008.
- [134] S. N. Zhurkov and V. E. Korsukov, “Atomic mechanism of fracture of solid polymers,” *Journal of Polymer Science: Polymer Physics Edition*, vol. 12, no. 2, pp. 385–398, 1974.

- [135] T. T. Perkins, D. E. Smith, and S. Chu, “Single polymer dynamics in an elongational flow,” *Science*, vol. 276, no. 5321, pp. 2016–2021, 1997.
- [136] S. Gerashchenko and V. Steinberg, “Statistics of tumbling of a single polymer molecule in shear flow,” *Physical review letters*, vol. 96, no. 3, p. 038304, 2006.
- [137] C. Schroeder, R. Teixeira, E. Shaqfeh, and S. Chu, “Characteristic Periodic Motion of Polymers in Shear Flow,” *Physical Review Letters*, vol. 95, p. 018301, July 2005.
- [138] D. E. Smith, H. P. Babcock, and S. Chu, “Single-polymer dynamics in steady shear flow,” *Science*, vol. 283, no. 5408, pp. 1724–1727, 1999.
- [139] R. Delgado-Buscalioni, “Cyclic motion of a grafted polymer under shear flow,” *Physical review letters*, vol. 96, no. 8, p. 088303, 2006.
- [140] P. S. Doyle, B. Ladoux, and J.-L. Viovy, “Dynamics of a Tethered Polymer in Shear Flow,” *Physical Review Letters*, vol. 84, p. 4769, May 2000.
- [141] G. K. Batchelor, *An introduction to fluid dynamics*. Cambridge University Press, 2000.
- [142] M. Saphiannikova, I. Neelov, V. Pryamitsyn, A. a. Darinskii, and F. Sundholm, “Computer simulation of polymer brushes under shear,” *Rheologica Acta*, vol. 39, pp. 469–475, Oct. 2000.
- [143] G. H. Fredrickson, A. Ajdari, L. Leibler, and J. P. Carton, “Surface modes and deformation energy of a molten polymer brush,” *Macromolecules*, vol. 25, no. 11, pp. 2882–2889, 1992.
- [144] H.-W. Xi and S. T. Milner, “Surface waves on polymer brushes,” *Macromolecules*, vol. 29, no. 13, pp. 4772–4776, 1996.
- [145] L. D. Landau and E. M. Lifshitz, *Theory of Elasticity, 3rd*. Pergamon Press, Oxford, UK, 1986.
- [146] H. U. Sverdrup and W. H. Munk, “Wind, sea, and swell: theory of relations for forecasting,” 1947.

- [147] V. Kumaran and R. Muralikrishnan, “Spontaneous growth of fluctuations in the viscous flow of a fluid past a soft interface,” *Phys. Rev. Lett.*, vol. 84, pp. 3310–3313, Apr 2000.
- [148] S. Mandre and L. Mahadevan, “A generalized theory of viscous and inviscid flutter,” *Proceedings of the Royal Society of London A: Mathematical, Physical and Engineering Sciences*, 2009.
- [149] J. Elgeti and G. Gompper, “Emergence of metachronal waves in cilia arrays,” *Proceedings of the National Academy of Sciences*, vol. 110, no. 12, pp. 4470–4475, 2013.
- [150] J. R. Blake, “A model for the micro-structure in ciliated organisms,” *Journal of Fluid Mechanics*, vol. 55, pp. 1–23, 1972.
- [151] F. Gosselin and E. de Langre, “Destabilising effects of plant flexibility in air and aquatic vegetation canopy flows,” *European Journal of Mechanics-B/Fluids*, vol. 28, no. 2, pp. 271–282, 2009.
- [152] C. Py, E. De Langre, and B. Moulia, “A frequency lock-in mechanism in the interaction between wind and crop canopies,” *Journal of Fluid Mechanics*, vol. 568, pp. 425–449, 2006.
- [153] M. Dabagh, P. Jalali, P. J. Butler, and J. M. Tarbell, “Shear-induced force transmission in a multicomponent, multicell model of the endothelium,” *Journal of The Royal Society Interface*, vol. 11, no. 98, p. 20140431, 2014.
- [154] Y. Yao, *Three-dimensional flow-induced dynamics of the endothelial surface glycocalyx layer*. PhD thesis, Massachusetts Institute of Technology, 2007.
- [155] D. A. Fedosov, M. Peltomäki, and G. Gompper, “Deformation and dynamics of red blood cells in flow through cylindrical microchannels,” *Soft Matter*, vol. 10, no. 24, pp. 4258–4267, 2014.
- [156] L. Lanotte, G. Tomaiuolo, C. Misbah, L. Bureau, and S. Guido, “Red blood cell dynamics in polymer brush-coated microcapillaries: A model of endothelial glycocalyx in vitro,” *Biomicrofluidics*, vol. 8, no. 1, p. 014104, 2014.
- [157] T. W. Secomb, R. Skalak, N. Özkaya, and J. Gross, “Flow of axisymmetric red blood cells in narrow capillaries,” *Journal of Fluid Mechanics*, vol. 163, pp. 405–423, 1986.

- [158] T. W. Secomb, “Flow-dependent rheological properties of blood in capillaries,” *Microvascular research*, vol. 34, no. 1, pp. 46–58, 1987.
- [159] G. Tomaiuolo, M. Simeone, V. Martinelli, B. Rotoli, and S. Guido, “Red blood cell deformation in microconfined flow,” *Soft Matter*, vol. 5, no. 19, pp. 3736–3740, 2009.
- [160] T. W. Sirk, Y. R. Slizoberg, J. K. Brennan, M. Lisal, and J. W. Andzelm, “An enhanced entangled polymer model for dissipative particle dynamics,” *The Journal of chemical physics*, vol. 136, no. 13, p. 134903, 2012.
- [161] R. Potestio, S. Fritsch, P. Espanol, R. Delgado-Buscalioni, K. Kremer, R. Everaers, and D. Donadio, “Hamiltonian adaptive resolution simulation for molecular liquids,” *Physical review letters*, vol. 110, no. 10, p. 108301, 2013.
- [162] C. Pozrikidis, *Boundary integral and singularity methods for linearized viscous flow*. Cambridge University Press, 1992.
- [163] H. Bekker *et al.*, *Molecular dynamics simulation methods revised*. PhD thesis, 1996.

Polymer brushes are dense matrices of grafted macromolecules. In addition to brushes finely designed in laboratory, various examples are offered by Nature, as the endothelial glycocalyx, decorating the lumen of mammalian blood vessels. The interaction of such network with the flowing plasma and cells is still partially unknown. The present thesis, by mean of Dissipative Particle Dynamics simulations, proposes a coarse-grained model for the self-consistent analysis of a dense polymer brush under parabolic flow. Our mesoscale investigation highlights the relevance of collective effects, driven by hydrodynamics, and proposes novel interpretations regarding the rich phenomenology of the brush-flow system. Preliminary results are also provided for the interplay between a mesoscopic deformable flowing object (prototype of a red blood cell) and the grafted polymers.

Une brosse de polymère est une matrice dense de macromolécules greffées à une surface donnée. Au-delà des brosses synthétiques réalisées en laboratoire, on trouve des exemples très variés dans la nature: un exemple emblématique est le glycocalyx endothélial, décorant la surface interne des vaisseaux sanguins des mammifères. L'interaction de cette structure avec le plasma et les cellules sous écoulement n'est encore que très partiellement explorée. La présente thèse propose, grâce à des simulations de Dissipative Particle Dynamics, un modèle coarse-grained pour une analyse auto-cohérente d'une brosse polymérique dense sous écoulement parabolique. Cette étude mésoscopique met en évidence l'importance des effets collectifs entre molécules, entraînés par l'hydrodynamique, et propose des nouvelles interprétations à la phénoménologie du système brosse-écoulement. Des résultats préliminaires sont également produits pour l'interaction sous écoulement entre un objet mésoscopique déformable (prototype d'un globule rouge) et les polymères greffés.